

Global Energetics of Solar Flares: I. Magnetic Energies

Markus J. Aschwanden¹

¹) *Lockheed Martin, Solar and Astrophysics Laboratory, Org. A021S, Bldg. 252, 3251 Hanover St., Palo Alto, CA 94304, USA; e-mail: aschwanden@lmsal.com*

and

Yan Xu² and Ju Jing²

²) *Space Weather Research Laboratory, Center for Solar-Terrestrial Research, New Jersey Institute of Technology, 323 Martin Luther King Blvd., Newark, NJ 07102-1982, USA; e-mails: yan.xu@njit.edu, ju.jing@njit.edu*

ABSTRACT

We present the first part of a project on the global energetics of solar flares and coronal mass ejections (CMEs) that includes about 400 M- and X-class flares observed with AIA and HMI onboard SDO. We calculate the potential (E_p), the nonpotential (E_{np}) or free energies ($E_{free} = E_{np} - E_p$), and the flare-dissipated magnetic energies (E_{diss}). We calculate these magnetic parameters using two different NLFFF codes: The COR-NLFFF code uses the line-of-sight magnetic field component B_z from HMI to define the potential field, and the 2D coordinates of automatically detected coronal loops in 6 coronal wavelengths from AIA to measure the helical twist of coronal loops caused by vertical currents, while the PHOT-NLFFF code extrapolates the photospheric 3D vector fields. We find agreement between the two codes in the measurement of free energies and dissipated energies within a factor of $\lesssim 3$. The size distributions of magnetic parameters exhibit powerlaw slopes that are approximately consistent with the fractal-diffusive self-organized criticality model. The magnetic parameters exhibit scaling laws for the nonpotential energy, $E_{np} \propto E_p^{1.02}$, for the free energy, $E_{free} \propto E_p^{1.7}$ and $E_{free} \propto B_\varphi^{1.0} L^{1.5}$, for the dissipated energy, $E_{diss} \propto E_p^{1.6}$ and $E_{diss} \propto E_{free}^{0.9}$, and the energy dissipation volume, $V \propto E_{diss}^{1.2}$. The potential energies vary in the range of $E_p = 1 \times 10^{31} - 4 \times 10^{33}$ erg, while the free energy has a ratio of $E_{free}/E_p \approx 1\% - 25\%$. The Poynting flux amounts to $F_{flare} \approx 5 \times 10^8 - 10^{10}$ erg cm⁻² s⁻¹ during flares, which averages to $F_{AR} \approx 6 \times 10^6$ erg cm⁻² s⁻¹ during the entire observation period and is comparable with the coronal heating rate requirement in active regions.

Subject headings: Sun: Flares — Magnetic fields — Sun: UV radiation

1. INTRODUCTION

“The whole is greater than the sum of its parts”, mused Aristotle to his disciples, written down in his *Metaphysics* 350 B.C.E, when he wondered whether there are additional substances besides fire, earth, water, and air, that make up our universe. His disciples may be intrigued about the mathematical paradoxon. Exploring the global energetics of solar flares and associated eruptive phenomena, we also wonder whether we can measure all components of the energy output, partitioned by secondary processes, and whether the sum of their parts matches the whole of the energy input. In a nutshell, our concept or working hypothesis is that all primary energy input is provided by dissipation of magnetic energies, which supply the energy

output of secondary processes, such as the thermal energies of the heated flare plasma, the nonthermal energies of accelerated particles that produce hard X-rays, gamma-rays, or are detected as *solar energetic particles (SEP)*, and kinetic energies of coronal mass ejections (CMEs). Regardless whether this hypothesis is true or false, obtaining quantitative statistics of the different forms of energies will be extremely useful for a host of reasons: (i) Do the known forms of energy add up or do we miss important parts (similar to the dark matter problem of the universe); (ii) do we have sufficient magnetic energy to supply all secondary processes, or are our magnetic reconnection models insufficient; or (iii) what is the cause and consequence, the efficiency and upper limits of various energy conversion processes? Essentially, every theoretical solar flare or CME model can be tested, evaluated, and disproved by energetic considerations.

The global energetics of solar flares and their energy partition has been systematically addressed in some earlier studies, in two papers on the energy partition of two solar flare/CME events (Emslie et al. 2004, 2005), and in one on the global energetics of 38 large solar eruptive events (Emslie et al. 2012). Although these papers study various contents of energy, such as (i) the radiated energy in soft X-rays detected by GOES, (ii) the total energy radiated in soft X-rays, (iii) the peak energy in soft X-rays, (iv) the bolometric radiated energy, (v) the non-thermal energy in accelerated >20 keV electrons, (vi) in >1 MeV ions, (vii) the kinetic energies in CMEs, and (viii) in solar energetic particles (SEP) in interplanetary space, no measurement of the amount of available free magnetic energy that drives all these energy conversion processes was attempted. Instead, the simple (non-dissipative) magnetic potential field was calculated, and an ad hoc value of 30% was used to estimate the free magnetic energy. In the meantime, various *nonlinear force-free field (NLFFF)* codes have been developed that are able to calculate the free magnetic energy directly, either using information from vector magnetic field measurements (e.g., Metcalf et al. 1995, 2005; Bobra et al. 2008; Jiao et al. 1997; Guo et al. 2008; Schrijver et al. 2008; Thalmann et al. 2008, 2013), or employing tools that take advantage of the geometry of coronal loops, which supposedly trace out the “true” coronal magnetic field (Aschwanden 2013a,b,c; Aschwanden and Malanushenko 2013; Malanushenko et al. 2011, 2012, 2014). Thus, the new capabilities of calculating free magnetic energies as well as their decreases during flares with high-quality HMI/SDO data, represent one important justification to investigate the global energetics of solar flares now. Another important reason is the unprecedented EUV and soft X-ray imaging capabilities of AIA/SDO, which copiously display the twisted, sigmoid-like, and helical geometry of coronal loops that define the non-potential magnetic field. In addition, the EUV images provide spatial information (length scales, areas, and volumes of flares) which is a prerequisite to calculate the volume-integrated thermal energies in flares. Moreover, the EUV images from AIA/SDO and EUVI/STEREO yield also detailed information on EUV dimming during the launch of a CME (Aschwanden et al. 2009b), and thus allow us to determine masses, velocities, and kinetic energies of CMEs at any location on the solar disk, while the traditional measurements of CME masses using the polarized brightness of white-light images (e.g., Vourlidas et al. 2010) are only feasible near the solar limb.

This first paper of a series on the global energetics of solar flares is dealing with magnetic energies. Further studies will include thermal energies, non-thermal energies, kinetic energies of CMEs, a comparative synthesis of the global energetics, and the application of the fractal-diffusive self-organized criticality model. The organization of this first paper is as follows. Section 2 contains a brief description of the two used magnetic calculation methods, the PHOT-NLFFF and the COR-NLFFF codes, while more details about the COR-NLFFF code, especially the recent improvements, are described in the Appendices A (Automated tracing of coronal loops), B (Potential field parameterization), C (Rotational invariance of magnetic field), and D (Forward-fitting of non-potential fields). In Section 3 we present the observations and statistical results, based on the data analysis of a comprehensive dataset that includes all M- and X-class flares observed

with the SDO during the first 3.5 years of the mission. The results include measurements of the free energy and their uncertainties, their time evolution, their timing, comparisons between the two codes, scaling laws, geometric measurements, size distributions, and the Poynting flux. In the Discussion in Section 4 we address aspects of measuring the coronal magnetic field, the illumination effects that cause an apparent increase of free energies, a self-organized criticality model, previous measurements of flare-dissipated energies, scaling laws of magnetic energy dissipation, and aspects relevant to the coronal heating problem. We summarize the Conclusions in Section 5.

2. DATA ANALYSIS METHODS

In this study we deal with two fundamentally different methods to calculate magnetic energies of active regions during solar flare events, which differ in their (photospheric versus coronal) origin of the observables. Photospheric codes calculate nonlinear force-free fields (PHOT-NLFFF) based on an extrapolation of the photospheric 3D magnetic field vectors $\mathbf{B}(x, y) = [B_x(x, y), B_y(x, y), B_z(x, y)]$ (Section 2.1), while the alternative method (COR-NLFFF) calculates coronal nonlinear force-free fields by fitting a force-free field model to coronal loop geometries $[x(s), y(s)]$, which are obtained by an automated feature detection method applied to multi-wavelength EUV images, as well as using the line-of-sight component $B_z(x, y)$ from a simultaneously observed magnetogram (Section 2.2).

2.1. The Photospheric Magnetic Field Extrapolation Method (PHOT-NLFFF)

We use the photospheric vector magnetograms from the HMI onboard SDO (Scherrer et al. 2012; Hoeksema et al. 2014) as the boundary condition for the photospheric non-linear forcefree field extrapolation method (PHOT-NLFFF). Since the photosphere is not forcefree (Metcalf et al. 1995), while the corona is generally close to forcefree, a pre-processing technique is used to make the photospheric boundary near-forcefree before extrapolation with the 3D NLFFF code (Wiegelmann et al. 2006, 2008; Wheatland and Regnier 2009). For the pre-processing we use the weighted optimization method of Wiegelmann (2004), which is an implementation of the original work of Wheatland et al. (2000). The extrapolations were performed using non-uniformly rebinned magnetograms (approximately with a scale of 2 pixels $\times 0.5'' = 1.0''$) within a computational domain of $248 \times 248 \times 200$ (sometimes $248 \times 124 \times 200$) uniform grid points, corresponding to $\approx (180 \times 180 \times 145) \text{ Mm}^3$, or $(180 \times 90 \times 145) \text{ Mm}^3$, respectively. Since the Wiegelmann code requires a planar boundary perpendicular to the line-of-sight, the vector magnetograms are de-rotated to the disk center and remapped using the Lambert (cylindrical) equal-area projection (see also Sun et al. 2012 and references therein).

The NLFFF extrapolation yields a 3D field $\mathbf{B}(\mathbf{x}) = [B_x(x, y, z), B_y(x, y, z), B_z(x, y, z)]$ in each voxel of the 3D cube. The free magnetic energy E_{free} quantifies the energy deviation of the coronal magnetic non-linear forcefree field \mathbf{B}_{np} from its potential field state \mathbf{B}_p , which is defined as

$$E_{free} = E_{np} - E_p = \int \frac{(B_{np}^2 - B_p^2)}{8\pi} dV, \quad (1)$$

where V is the volume of the computational domain from the photosphere to the corona, and the subscripts np and p represent the NLFFF and the potential field, respectively. More details about the calculation of free magnetic energy with the NLFFF code used here are given in Jing et al. (2010).

For the present study we calculated PHOT-NLFFF solutions at a single time near the flare peak for 56 (out of the possible 172) flare events with >M1.0 GOES class, all at locations within $\leq 45^\circ$ heliographic longitude difference to the central meridian. For the subset of the 11 largest events (of >X1.0 GOES class) we calculated a time series of free energies with a cadence of 12 minutes. The calculation of a nonpotential field solution in a 3D computation box for a single time frame requires about 10 – 12 hours computation time.

2.2. The Coronal Loop Fitting Method (COR-NLFFF)

An alternative method is the so-called *Coronal Nonlinear Force-Free Field (COR-NLFFF)* code, which we are using for the computation of nonpotential fields by employing coronal constraints. This novel method uses a line-of-sight magnetogram to define a potential field solution, and applies forward-fitting of a parameterized NLFFF model (in terms of vertical currents) to the geometry of observed coronal loops, which supposedly trace out the true coronal magnetic field. The chief advantage of this alternative model is that the NLFFF solution is not affected by the non-forcefreeness of the photosphere and lower chromosphere (because it does not use the transverse photospheric magnetic field vectors in the extrapolation of a NLFFF solution, as the standard PHOT-NLFFF codes do), and that the obtained NLFFF solution matches closely the geometry of the observed coronal loops (while standard PHOT-NLFFF codes have no capability to fit the coronal loop geometry). Moreover, the COR-NLFFF code is orders of magnitude faster than traditional PHOT-NLFFF codes, because the COR-NLFFF model (in terms of vertical currents) represents an analytical NLFFF approximation (force-free to second order in the force-free α -parameter) that can be forward-fitted fast and efficiently. The forward-fitting of a COR-NLFFF solution for a single time frame is accomplished typically in $\approx 1 - 2$ min, which is about 2-3 orders of magnitude faster than with a PHOT-NLFFF code.

Previous studies using this COR-NLFFF code include the analytical derivation of a NLFFF solution in terms of vertical currents (Aschwanden 2013a), the numerical prototype code and tests with simulated data (Aschwanden and Malanushenko 2013), calculations of the free energy (Aschwanden 2013b), potential-field calculations of active regions (Aschwanden and Sandman 2010), nonpotential-field calculations of active regions using stereoscopic data (Aschwanden et al. 2012a), nonpotential forward-fitting with and without stereoscopic data (Aschwanden 2013c), and comparisons of PHOT-NLFFF and COR-NLFFF solutions for the 2011 February 12-17 flares (Aschwanden, Sun, and Liu 2014a). The COR-NLFFF code has been continuously developed over the last years, leading to substantial new improvements that are briefly described in the Appendices A, B, C, and D. The COR-NLFFF code consists of three principal parts: (i) the automated tracing of coronal loops in EUV images (Appendix A), the potential-field parameterization (Appendix B), which is shown to be invariant to the solar rotation (Appendix C), and the forward-fitting of nonpotential fields (Appendix D).

For the calculation of the free energy E_{free} we use the same definition as given for PHOT-NLFFF codes (Eq. 1), except that we correct for isotropic twist directions. Since the analytical nonpotential field approximation includes only magnetically twisted field lines wound around vertical twist axes, the obtained free energy E_{\perp}^{free} is a lower limit to the total free energy E^{free} . In order to obtain a first-order correction, we consider a current along a semi-circular loop or filament, which has a cosine-dependence along the loop and can be statistically included by introducing an *isotropic twist correction factor* $q_{iso} = (\pi/2)^2 \approx 2.5$ (Aschwanden, Sun, and Liu 2014a),

$$E_{\perp}^{free} = E^{free} \langle \cos(\theta)^{-2} \rangle = E^{free} \left(\frac{2}{\pi} \right)^2 = E^{free} / q_{iso} . \quad (2)$$

Thus we expect that the corrected free energy is about a factor of $q_{iso} = (\pi/2)^2 \approx 2.5$ higher than the best-fit values of the vertical-current free energies E_{\perp}^{free} .

3. OBSERVATIONS AND RESULTS

3.1. AIA and HMI Observations

The dataset we are analyzing for this project on the global energetics of flares includes all M- and X-class flares observed with the *Solar Dynamics Observatory (SDO)* (Pesnell et al. 2011) during the first 3.5 years of the mission (2010 June 1 to 2014 Jan 31), which amounts to 399 flare events. The catalog of these flare events is available online, see http://www.lmsal.com/~aschwand/RHESSI/flare_energetics.html. Magnetic energies are determined for events that have a heliographic longitude of $\lesssim 45^{\circ}$ (177 events), of which 5 events contained incomplete or corrupted AIA data, so that we are left with 172 events suitable for magnetic data analysis. Using the COR-NLFFF code we calculate the evolution of free (magnetic) energies for all of these 172 events, while a subset of 57 events is subjected to the (computationally more expensive) PHOT-NLFFF code also.

The analyzed SDO data set includes EUV images observed with the *Atmospheric Imaging Assembly (AIA)* (Lemen et al. 2012; Boerner et al. 2012), as well as magnetograms from the *Helioseismic and Magnetic Imager (HMI)* (Scherrer et al. 2012). The SDO started observations on 29 March 2010 and has produced essentially continuous data of the full Sun since then.

AIA provides EUV images from four 4096×4096 detectors with a pixel size of $0.6''$, corresponding to an effective spatial resolution of $\approx 1.6''$. AIA contains ten different wavelength channels, three in white light and UV, and seven EUV channels, whereof six wavelengths (94, 131, 171, 193, 211, 335 Å) are centered on strong iron lines (Fe VIII, IX, XII, XIV, XVI, XVIII), covering the coronal range from $T \approx 0.6$ MK to $\gtrsim 16$ MK. AIA records a full set of near-simultaneous images in each temperature filter with a fixed cadence of 12 seconds.

HMI provides full-disk magnetograms from measurements of the Doppler shift using the 6173 Å Fe I absorption line. The HMI magnetograms are recorded with a 4096×4096 pixel camera with a pixel size of $0.5''$, giving an overall cadence of 45 s for the Doppler velocity, intensity, and LOS magnetic field measurements, which have been processed from 135 s time intervals.

3.2. Example of a NLFFF Solution

An example of a forward-fitting solution for one instant of time during the evolution of a solar flare is given in Fig. 1, which shows AR 11158 at heliographic position S21N12 observed on 2011 February 15, 01:14 UT, shortly before the GOES-class X2.2 flare. The theoretical field lines of the best forward-fit nonpotential field model (red curves in Fig. 1) are overlaid on the tracings of observed loops (yellow curves in Fig. 1), calculated at the intersection at the midpoints of each observed loop segment. The observed magnetogram and the model with the decomposed magnetic charges are shown in Fig. 20. The control parameters of the COR-NLFFF code are listed on the right side of Fig. 1, where also a histogram of the misalignment angles of all loops is shown, with a median of $\mu_2 = 6.8^{\circ}$. From the 6 AIA wavelength images, a total of 508 loop structures were automatically detected, of which only 300 loops were used for forward-fitting, while a large number (188) of structures with a ripple ratio of $q_{ripple} \geq 0.50$ have been discarded (which

mostly contain “moss”-contaminated structures, see Appendix A). The key results of this run are the median misalignment angle of $\mu_2 = 6.8^\circ$ (which expresses the goodness-of-fit), the total potential energy of the active region, $E_p = 1.08 \times 10^{33}$ erg, the free energy, $E_{free} = E_{np} - E_p = 1.15 \times 10^{32}$ erg, which yields a ratio of $q_{np} = E_{np}/E_p = 1.106$, or a free energy that is 10.6% of the potential energy.

3.3. Uncertainties of Free Energy Measurements

In Fig. 2 we show the time evolution of the magnetic free energy $E_{free}(t)$, the soft X-ray GOES 1-8 Å flux profile $F_{GOES}(t)$, the misalignment angles $\mu_2(t)$, and the number of detected $n_{det}(t)$ and fitted loops $n_{loop}(t)$. For all cases in our analysis we compute a time series with a length that covers the flare duration plus a half hour margin before and after the flare, with a cadence of 0.1 hours (6 min), yielding about 12-40 time frames per flare. For event #12 shown in Figs. 1 and 2, we need 13 time intervals (with a step of $dt = 0.1$ hr) to cover the time series.

In order to quantify an error of the measurement of free energies we vary most of the control parameters and find that the final result of the free energy is somewhat sensitive to the loop selection criterion q_{ripple} (Appendix A). Therefore we perform the forward-fitting with 3 different sets of loop selection parameters: $q_{ripple} = 0.25$ (RUN1; Fig. 2 left), $q_{ripple} = 0.50$ (RUN2; Fig. 2 middle), and $q_{ripple} = 0.75$ (RUN3; Fig. 2 right). This “ripple criterion” (Eq. A2) discriminates between smooth loop flux profiles ($q_{ripple} \gtrsim 0$) and highly fluctuating loop flux profiles ($q_{ripple} \lesssim 1$) that are most likely containing “moss structures” rather than loops, or a combination of both (see Fig. 18 for examples of “moss-like” structures). A low value of the ripple criterion has the advantage of selecting only “good loop structures”, but has the disadvantage that the number of selected loops is low, which may not be sufficient in some cases to constrain the nonpotential energy near some magnetic sources (see low ratio of fitted to detected loops in Fig. 2 (bottom left panel). A high value, on the other side, contains more “false (moss) structures”, but provides more statistics that enables “good” forward-fitting solutions (see large ratio of fitted to detected loop structures in Fig. 2: bottom right panel). Therefore, the optimum is somewhere inbetween (say around $q_{ripple} \approx 0.5$). However, as the values shown in Fig. 2 demonstrate (see error bars in Fig. 2, top panel), the results of the free energy $E_{free}(t)$ are fairly robust for different loop selection parameters ($q_{ripple} = 0.25 - 0.75$), and thus we use the mean and standard deviation of these multiple (selection-dependent) solutions for error estimates of the free energy, $E_{free} \pm \sigma_{E,free}(t)$. We average the results from all the 3 trial runs (RUN1, RUN2, RUN3) and obtain a mean $E_{free}(t)$ and standard deviation $\sigma_{E,free}(t)$ of the free energy. The uncertainty or error $e_{E,free}(t)$ of the mean value of the free energy (for each time frame t) is according to standard statistics (Bevington and Robinson 1992)

$$e_{E,free}(t) = \frac{\sigma_{E,free}(t)}{\sqrt{N_{run}}}, \quad (3)$$

where $N_{run} = 3$ for our 3 trial runs with different loop selection criteria.

The evolutionary time profiles shown in Fig. 2 reveal a number of interesting features of the COR-NLFFF code. The most instructive property is that the free energy $E_{free}(t)$ systematically drops before the flare start time, for any chosen loop detection criterion (see error bars in Fig. 2, top, which are obtained from the scatter of the three runs), in contrast to the GOES flux that increases slowly in the preflare phase and then grows rapidly during the flare rise time (Fig. 2, second row). The drop in free energy is accompanied by a decrease of the nonlinear force-free parameter α_m for some of the strongest magnetic sources m , such as for the magnetic charges $m = 0, 1, 2$, and 3 (Fig. 2, third row). The misalignment angle varies in the range of $\mu_2(t) \approx 5^\circ - 10^\circ$ for the selection of smooth loops ($q_{ripple} \leq 0.25$), while the misalignment is larger

$\mu_2(t) \approx 8^\circ - 13^\circ$ for the selection of loops with a higher ripple ratio $q_{ripple} \leq 0.75$ (Fig. 2, fourth row), because of a higher contamination of “false loops” or moss features. The largest misalignment occurs around the flare peak time, when image saturation, pixel bleeding, and diffraction patterns occur and produce “false loop structures” that are difficult to completely remove (see details in Appendix A and Fig. 18).

3.4. Time Evolution of the Coronal Free Energy

Naively, we expect that the free energy $E_{free}(t)$ in a flaring active region has a near-constant value before a flare (because build-up or storage of nonpotential magnetic energy is slow compared with the rise time of a flare), which then decreases monotonically during the flare time interval, dropping to a lower level after the flare. We will see that this “single-step decrease” behavior is sometimes observed in the free energy when computed from photospheric field extrapolations (with PHOT-NLFFF codes), but the measurements of the free energy based on coronal loops (using COR-NLFFF codes) exhibit a more complex behavior that involves both apparent increases and decreases of the free energy before and during flare time intervals (Aschwanden, Sun, and Liu 2014a). The key aspect to understand this complex behavior is based on the fact that not all twisted and current-carrying loop structures are illuminated before the flare, and thus part of the free energy is invisible before the flare. Once the flare starts, chromospheric evaporation gradually fills up more and more helically twisted loops until all or most twisted loop structures are “illuminated” and the full amount of free energy becomes detectable. At the same time, some free magnetic energy becomes dissipated during the flare, which is manifested by decreases of the free energy. Thus, essentially we can interpret the increases of free energy after flare start as temporary “coronal illumination” effects, while decreases can be interpreted as episodes of “magnetic energy dissipation”. In simple flares we expect then to observe one single increase of the free energy at flare start, followed by a single decrease during the flare rise time. In more complex flares, multiple phases of illuminations and dissipations follow each other sequentially. The simplest method to measure the total amount of dissipated energy is then just to ignore the increases due to illumination effects and to sum up all energy decreases during the flare time interval. The principle of this method is illustrated in Fig. 3 for two subsequent illumination and dissipation phases. The total amount of dissipated free energy is $\Delta E_{free} = \Delta E_{3-2} + \Delta E_{5-4}$ in this example.

One might wonder whether the time intervals with decreases in the free energy could be interpreted as an inverse illumination effect, namely a disappearance of twisted flare loops by cooling, moving a detected loop eventually out of the observed wavelength passband and making it invisible again. This ambiguity, however, can entirely be ruled out during the risetime of soft X-ray or EUV light curves, because the rise time indicates a phase of increasing flux, emission measure, and electron density of the flaring structures, and thus would contradict an interpretation in terms of cooling-related flux decrease.

3.5. Measurement of Evolutionary Parameters

Based on the foregoing discussion we need to deconvolve the time evolution of energy dissipation (which manifests as a temporary decrease of free energy) from the illumination effects (which is indicated by a temporary increase of free energy). In order to achieve such a deconvolution we ignore the time steps with increasing energy and derive a time profile $E_{neg}(t)$ that includes only the negative energy decreases $dE_{free}(t)/dt < 0$, which is shown in Fig. 4 (second panel), as derived from the free energy time profile $E_{free}(t)$ of an observed flare (Fig. 4, top panel), observed with SDO on 2012-Mar-07, 00:02 UT (event #

147), being the largest flare of our analyzed dataset. This monotonously decreasing time profile $E_{neg}(t)$ mimics the free energy time profile that would be observed under ideal circumstances when all nonpotential loops would be illuminated in a coronal image (i.e., without illumination effects).

The time profile of the dissipated energy $E_{diss}(t)$ (Fig. 4, third panel) can then be defined as a positive energy by subtracting this monotonically decreasing energy time profile from its maximum value at the start time t_0 ,

$$E_{diss}(t) = E_{neg}(t_0) - E_{neg}(t) , \quad (4)$$

or alternatively we can derive it directly from the free energy profile $E_{free}(t)$ by adding the negative decreases as positive increments, ignoring the positive increases,

$$E_{diss}(t_i) = E_{diss}(t_{i-1}) + ([E_{free}(t_{i-1}) - E_{free}(t_i)] > 0) . \quad (5)$$

In addition we define the magnetic energy dissipation rate $F_{diss}(t)$, which is the time derivative of the dissipated energy $E_{diss}(t)$,

$$F_{diss}(t_i) = \frac{dE_{diss}(t_i)}{dt} = \frac{E_{diss}(t_{i+1}) - E_{diss}(t_{i-1})}{2 dt_i} , \quad (6)$$

where dt is the time step of the time profile, which is $dt = 0.1$ hr in our case. This energy dissipation rate is shown in Fig. 4 (fourth panel, red-hatched curve) and coincides closely with the time derivative of the GOES 1-8 Å time profile, dF_{GOES}/dt (Fig. 4, fifth panel, blue-hatched curve), which is a good proxy for the time profile of hard X-ray emission, particle acceleration, and the chromospheric thick-target heating rate in solar flares (Dennis and Zarro 1993; Brown 1972). Note that the two time profiles of energy dissipation are determined from absolutely independent parameters: the magnetic energy dissipation rate $F_{diss}(t) = dE_{diss}(t)/dt$ is entirely inferred from the geometry of untwisting coronal loops, while the GOES time derivative is derived from the soft X-ray brightness of flare loops.

The example shown in Fig. 4 contains also error bars for each evolutionary parameter at each time step, which we calculate based on the uncertainties of the free energies $F_{free}(t)$ obtained from multiple runs with different loop selections (Section 3.3), and using Monte-Carlo simulations that propagate the errors using the definitions of the evolutionary time profiles given in Eqs. 4-6).

3.6. The Timing of Magnetic Energy Dissipation

In the following we investigate the relative timing of the magnetic energy dissipation rate $F_{diss}(t) = dE_{diss}/dt$ with respect to the flare peak time of the GOES soft X-ray flux. A representative subset of 60 examples out of the 172 analyzed >M1.0 GOES-class flare events are shown in Figs. 5 to 8, in order of increasing complexity. For each case we show the temporal evolution of the (best-fit) magnetic free energy $F_{free}(t)$ and energy dissipation rate $F_{diss}(t)$, along with the GOES 1-8 Å light curve that defines the flare start and end time (by NOAA convention), as well as its time derivative $dF_{GOES}(t)/dt$, which is a good proxy of the hard X-ray flux, the nonthermal emission, rate of particle acceleration, and rate of chromospheric heating.

In a first group (Fig. 5) we show 12 examples with flare events where magnetic energy dissipation starts already before the GOES-defined flare start. In some cases we see flare precursors in the GOES time profile and its time derivative, which may indicate an early trigger of magnetic energy dissipation. Note, however,

that the free energy is generally not constant before the flare, but rather increases before flare start, probably thanks to an illumination effect of soft X-ray loops by gentle evaporation during the preflare phase.

In a second group (Fig. 6) we show classic examples where the magnetic energy dissipation coincides with the flare rise time of the soft X-ray (GOES) light curve. This timing corresponds to our physical intuition that the major energy release phase of a flare occurs during the rise time, when nonthermal particles are accelerated that heat the chromosphere at the flare loop footpoints and drive chromospheric evaporation according to the thick-target model (Brown 1972), which is manifested as a steady increase of the soft X-ray flux. This scenario predicts a correlation between the soft X-ray flux increase and the magnetic energy decrease, which is indeed clearly fulfilled in the observed cases shown in Fig. 6.

In a third group (Fig. 7) we show examples where the peak of the magnetic energy dissipation does occur slightly after the soft X-ray flare peak, with continuing but decreasing energy dissipation in the flare decay phase. This behavior could be explained by strongly driven chromospheric evaporation during the flare peak time, which drives the illumination of twisted and soft X-ray emitting flare loops with a higher emission increase rate than the magnetic dissipation rate. Since the two effects of illumination and dissipation are competing, it is no surprise that either one can be dominating during particular time phases.

In a fourth group (Fig. 8) we show cases with double flares (although classified as a single event by NOAA), which are clearly accompanied with two-step magnetic energy dissipation phases. In these cases we can resolve two flare loop illumination phases with two subsequent magnetic energy dissipation phases, exactly as sketched in the cartoon of Fig. 3.

In a fifth group (Fig. 9) we show cases of complex flares, which consequently have multi-step energy dissipation phases as a consequence. These cases correspond to long-duration flares, which typically last a few hours (say 1-4 hrs). These events were classified as single flares according to the NOAA definition, but both the soft X-ray time profile as well as the time derivative (i.e., the hard X-ray proxy) show multiple peaks that could possibly be considered as multiple flares. Nevertheless, because these events last significantly longer and have many different soft X-ray and hard X-ray emission peaks, it is natural that the free energy dissipation rate reveals multiple phases also, which often exhibit a one-to-one correspondence. Note that the evolution of the magnetic energy does not exhibit a monotonously dropping staircase as a function of time, but rather an alternating sequence of (illumination) increases and (dissipation) decreases.

3.7. Comparison of Photospheric versus Coronal NLFFF Results

For a subset of 57 flare events we calculated the potential, nonpotential, and free energy with the PHOT-NLFFF code for one single time frame. We compare these magnetic energies with the COR-NLFFF code in form of scatterplots as shown in Fig. 10. We find the following ratios: $q_{np} = E_{np}^{COR}/E_{np}^{PHOT} = 0.998$ with a scatter by a factor of 1.4 for the nonpotential energy; $q_p = E_p^{COR}/E_p^{PHOT} = 1.080$ with a scatter by the same factor of 1.4 for the potential energy, and $q_{free} = E_{free}^{COR}/E_{free}^{PHOT} = 0.343$ with a scatter by a factor of 2.2 for the free energy. Some differences can be explained by slightly different field-of-views, but it is unknown to what extent the pre-processing technique of the PHOT-NLFFF code, or the deprojection of the magnetogram in the PHOT-NLFFF code plays a role in the obtained absolute magnetic field strengths. On the other side, a factor of $q_{iso} \approx 2.5$ has been applied to the COR-NLFFF code to correct for isotropic twist directions, which indeed improves the agreement between the two codes, since the free energy would otherwise be a factor of $0.32/2.5=0.13$ too low compared with the photospheric code. We suspect that the slightly different spatial resolution (2-pixel rebinning for the PHOT-NLFFF code versus 3-pixel rebinning

for the COR-NLFFF code) or unresolved twisted magnetic structures could explain the slight underestimate of the free energy.

For the subset of all (11) X-class flares we calculated the time evolution of the free energy $E_{free}(t)$ with both the PHOT-NLFFF and the COR-NLFFF codes, which are juxtaposed in Figs. 11 and 12 and listed in Table 4. We find good agreement between the potential energies (within a factor $q_{E,pot} \lesssim 1.05 \pm 0.33$; Table 4). Differences in the potential energy may partially be caused in the COR-NLFFF code by closely-spaced mixed magnetic polarities in the decomposition of the strongest fields in sunspots.

The agreement in the mean free energy is within a factor of $q_{E,free} = 3.3 \pm 2.3$ (Table 4), which means that the PHOT-NLFFF code detects about 3 times more free energy than the COR-NLFFF code. Systematic underestimates of the free energy with the COR-NLFFF code may be caused by (i) unresolved twisted structures, (ii) by an insufficient number of detectable coronal loops in magnetic field regions with high non-potentiality, or (iii) by the vertical-current approximation of our analytical NLFFF solution, which cannot model structures with horizontal twist axes, such as horizontal parts of helically twisted filaments.

The most important parameter is the decrease of the free energy during the flares. The PHOT-NLFFF code does not detect a significant decrease in one event (#148). The COR-NLFFF code exhibits a highly significant decrease in all 11 cases (Figs. 11 and 12), while the PHOT-NLFFF codes detects a factor of $q_{E,diss} = E_{diss}^{PHOT}/E_{diss}^{COR} = 0.5 \pm 0.4$ less dissipated energy, and thus the COR-NLFFF code appears to be more sensitive, a pattern that was also found in previous work (see Fig. 12 in Aschwanden, Sun, and Liu 2014a). Careful inspection of the time evolution of the free energy detected with the PHOT-NLFFF code reveals sometimes increases shortly before the flare (see event #344 in Fig. 12, which may indicate new magnetic flux emergence. We take such counter effects to energy dissipation into account by using only the cumulative decreases of free energy (thick blue curves in Figs. 11 and 12), the same way we do for the COR-NLFFF code (thick red curves in Figs. 11 and 12).

3.8. Scaling Laws of Magnetic Energies

In this study we present for the first time extensive statistics of magnetic energies that are dissipated in M- and X-class flares. The easiest magnetic quantity to measure is the total potential energy of an active region, for which we find a range of $E_p = 1 \times 10^{32}$ to 4×10^{33} erg. The other forms of magnetic energy are more difficult to compute and hitherto could only be obtained with time-consuming runs of a PHOT-NLFFF code. In contrast, our COR-NLFFF code is much faster and can easily provide large statistics and useful scaling laws for the nonpotential magnetic parameters, which are listed in Table 3 and shown in Fig. 13.

The nonpotential energy of an active region is very closely correlated to the potential energy, being a factor of $E_{np}/E_p = 1.07 \pm 0.06$ or 7% larger in the average. There is a slight nonlinearity between the two parameters, which we determine with a linear regression fit (Fig. 13 top left),

$$\left(\frac{E_{np}}{10^{30}\text{erg}} \right) = 0.92 \left(\frac{E_p}{10^{30}\text{erg}} \right)^{1.02}. \quad (7)$$

This implies also that the free energy amounts to 7% in the statistical average, within a scatter by a factor of 2.3 (Fig. 13, top right). A linear regression fit reveals the following scaling law (fig. 13, top right panel),

$$\left(\frac{E_{free}}{10^{30}\text{erg}} \right) = 0.00034 \left(\frac{E_p}{10^{30}\text{erg}} \right)^{1.73}, \quad (8)$$

so there is a strong nonlinearity of almost quadratic dependence. This means that active regions with larger potential energy have an overproportional amount of free energy available for flaring. Note that a constant fraction of $E_{free}/E_p = 0.30$ was assumed in the study of Emslie et al. (2012), which matches our scaling law for the very largest X-class flares only, but overestimates the free energy of M-class flares by about an order of magnitude.

The actually dissipated magnetic energy during a flare has a very similar dependence on the potential energy, namely (Fig. 13, bottom left),

$$\left(\frac{E_{diss}}{10^{30}\text{erg}}\right) = 0.017 \left(\frac{E_p}{10^{30}\text{erg}}\right)^{1.56}, \quad (9)$$

which implies that the magnetic energy E_{diss} dissipated in a flare is almost identical to the available free energy E_{free} , within a scatter by a factor of 2.4 (Fig. 13, bottom right),

$$\left(\frac{E_{diss}}{10^{30}\text{erg}}\right) = 2.6 \left(\frac{E_{free}}{10^{30}\text{erg}}\right)^{0.89}, \quad (10)$$

Note that the dissipated energy can exceed the free energy in our COR-NLFFF code, because not all free energy is visible at the beginning of the flare. In such cases, the dissipated free energy may still be accurate, but the mean free energy averaged during the flare time interval is underestimated. The ratio of free energies determined with the COR-NLFFF and PHOT-NLFFF code differ indeed a factor of $E_{free}^{COR}/E_{free}^{PHOT} \approx 0.34$ (Fig. 10, bottom left panel).

The scaling law of the free energy E_{free} (Eq. 8) allows us to express the mean twist angle φ as a function of the potential field energy E_p of an active region. The twist angle φ is defined by the ratio of the twisted azimuthal field component B_φ to the radial potential field component B_p by the relationship $\tan(\varphi) = B_\varphi/B_p$ (Aschwanden 2013a), and using the definition of the magnetic energies, i.e., $E_p = B_p^2/(8\pi)$ and $E_{free} = B_\varphi^2/(8\pi)$ (Aschwanden 2013b) we obtain with Eq. (8),

$$\tan(\varphi) = \left(\frac{B_\varphi}{B_p}\right) = \left(\frac{E_{free}}{E_p}\right)^{1/2} = 0.02 \left(\frac{E_p}{10^{30}\text{erg}}\right)^{0.37} \approx 1.2^\circ \left(\frac{E_p}{10^{30}\text{erg}}\right)^{0.37}. \quad (11)$$

According to this scaling law we expect mean twist angles of $\varphi = 1.2^\circ, 2.8^\circ, 6.6^\circ, 15^\circ, 36^\circ$, and 84° for active regions with total potential energies of $E_p = 10^{30}, 10^{31}, 10^{32}, 10^{33}, 10^{34}$, and 10^{35} erg, respectively. The latter value corresponds to about the maximum possible twist and predicts a maximum potential energy of $E_{p,max} \lesssim 10^{35}$ erg, which indeed represents a firm upper limit of all measured potential energies here, as well as for the events studied in Emslie et al. (2012).

3.9. Magnetic Energy Dissipation Areas

From the forward-fitting of the free energy $E_{free}(x, y, z)$ to the geometry of coronal loops and their flare-related decreases $E_{diss}(x, y, z)$ we can obtain statistics on the spatial geometry of magnetic energy dissipation areas in flaring regions. An example of the spatial distribution of the free energy before and at the peak of the largest analyzed flare, observed on 2011-Feb-15, 01:40 UT, is shown in Fig. 14 (top panels), with the evolution shown in Fig. 4. We show contours of constant free energies at levels of $E_{free} = (E_n - E_p) = (B_\varphi^2/8\pi)$ corresponding to azimuthal magnetic field strengths of $B_\varphi = 5, 10, \dots, 100$ G. In this example we witness an increase of the energy dissipation rate by a factor of 13 with respect to half an hour before the flare.

In order to characterize a geometric size A_{diss} of the entire flare we determine a cumulative flare area a_{cum} that contains all pixels of the energy dissipation distribution $E_{diss}(x, y, t)$ that exceeded a threshold value E_{thresh} at least ones during the entire flare time interval. This procedure is identical to spatio-temporal area definition of avalanche sizes in self-organized criticality models applied in many other fields (e.g., Uritsky et al. 2002 on magnetospheric auroras). The energy dissipation distribution $E_{diss}(x, y, t)$ is defined by (negative) decreases of the free energy during each time step dt ,

$$E_{diss}(x, y, t_i) = (E_{free}(x, y, t_{i-1}) - E_{free}(x, y, t_i)) > 0 . \quad (12)$$

We define an energy dissipation area $a(t)$ above some threshold level $E_{thresh} = B_\varphi^2/(8\pi)$, with $B_\varphi = 100$ G, unless the maximum of the map $E_{free}(x, y, t)$ is below this threshold value, in which case we take the full width at half maximum (FWHM) as a minimum width of the flare area. After counting all pixels above this threshold value we obtain an instantaneous flare area map $a(t)$, from which we synthesize a cumulative flare area $a_{cum}(t)$ that contains all partial flare areas since flare start (with a margin of 0.5 hours earlier). The synthesized cumulative area at the end of the flare (with a margin of 0.5 hours later) represents then the total flare area,

$$A = \sum a(t) = a_{cum}(t = t_{end}) . \quad (13)$$

The cumulative flare area $a_{cum}(t)$ is a monotonously growing quantity, $a_{cum}(t_i) \geq a_{cum}(t_{i-1})$. An example of this cumulative flare area is shown for flare #147 in Fig. 4 (bottom panel). The uncertainties are calculated from the scatter between the three trial runs with different loop selection parameters ($q_{ripple} = 0.25, 0.5, 0.75$). We define also related geometric parameters by simple Euclidean relationships, such as the flare length scale L ,

$$L = A^{1/2} , \quad (14)$$

and the flaring volume V ,

$$V = A^{3/2} . \quad (15)$$

Since some active regions are located up to longitudes of $\leq 45^\circ$ away from disk center of the visible hemisphere, we have to correct the projected areas (in the photosphere) with the cosine of the radial angle between Sun center and the heliographic position at longitude (l) and latitude (b),

$$A \approx \frac{A_{proj}}{\cos \sqrt{(l^2 + b^2)}} . \quad (16)$$

In self-organized criticality models, the dissipated energy is often assumed to scale with the size of an avalanche. Consequently, we expect a correlation between the geometric flaring volume V and the total dissipated magnetic energy E_{diss} . We show a correlation plot between these two measured parameters in Fig. 14 (bottom right) and find almost proportionality. There is only a slight deviation from proportionality that can be characterized by the scaling law (as obtained from a linear regression fit between the logarithmic quantities),

$$V \propto E_{diss}^{1.16} . \quad (17)$$

For the scaling between the length scale L and the dissipated energies E_{diss} we expect a powerlaw index that is 3 times smaller, i.e., $1.16/3 = 0.39$, which is indeed confirmed by a linear regression fit (Fig. 14, bottom),

$$L \propto E_{diss}^{0.39} . \quad (18)$$

These scaling laws we quantified for magnetic dissipation area in solar flares here for the first time, provide important information for physical models of the energy release process (e.g., reconnection scaling law of Shibata and Yokoyama 1999).

3.10. Size Distributions of Magnetic Parameters

In Fig. 15 we plot the size distributions (or occurrence frequency distributions) of the various magnetic energy parameters measured here. Each size distribution follows a powerlaw at the upper end of the distribution (and a roll-over at the lower end due to undersampling), as it is typical for parameters of a nonlinear dissipative system that is governed by self-organized criticality (Bak, Tang, and Wiesenfeld 1987), such as for solar flares (Lu and Hamilton 1991), in many wavelength regimes (e.g., see recent review by Aschwanden et al. 2014b). Here we measure the size distribution of magnetic parameters in solar flares for the first time and find the following powerlaw fits (Fig. 15): The dissipated energies E ,

$$N(E)dE \propto E^{-2.0 \pm 0.2} dE , \quad (19)$$

the peak energy dissipation rate P ,

$$N(P)dP \propto P^{-2.3 \pm 0.2} dP , \quad (20)$$

the flare durations (measured from the GOES start and end times),

$$N(T)dT \propto T^{-2.4 \pm 0.2} dT , \quad (21)$$

the flare length scale L ,

$$N(L)dL \propto L^{-3.8 \pm 0.3} dL , \quad (22)$$

the flare dissipation area A ,

$$N(A)dA \propto A^{-2.1 \pm 0.2} dA , \quad (23)$$

and the flaring volume V ,

$$N(V)dV \propto V^{-1.7 \pm 0.1} dV . \quad (24)$$

The powerlaw slopes extend over 1-2 decades of the logarithmic values. Our statistics is limited to $N = 172$ events for which magnetic analysis was suitable. From the geometric parameters, only the flare dissipation area A is directly measured, while the length L and volume V is directly derived from the Euclidean relationships (Eqs. 14-15).

3.11. Poynting Flux

We provide also statistics on the azimuthal magnetic field component B_φ , which is found to vary in the range of $B_\varphi \approx 12 - 400$ G, and is strongly correlated with the dissipated flare energy E (Fig 16, top left panel). Note, that this azimuthal field component determines the free energy E_{free} per voxel dV of the computation grid,

$$\frac{dE_{free}}{dV} = \frac{B_\varphi^2}{8\pi} , \quad (25)$$

and is found to be nearly proportional to the total (volume-integrated) dissipated energy, $E_{free} = \int (B_\varphi^2/8\pi)dV$, as the scatterplot in Fig. 16 (top right panel) demonstrates. This implies that most of the magnetic energy is contained in a compact core (that is of similar size in different flares) around the location with the maximum azimuthal magnetic field strength B_φ , and does not scale with the overall flare volume.

Finally we calculate also the Poynting flux F ,

$$F = \frac{E}{AT} = \frac{E}{L^2T} , \quad (26)$$

which specifies the energy flux per unit area A and time T , where E represents the total dissipated energy per flare. The scatterplot in Fig. 16 (bottom left panel) shows that the Poynting flux F is somewhat correlated with the dissipated energy E and has a range of $F \approx 5 \times 10^8 - 10^{10}$ erg cm⁻² s⁻¹. A theoretical estimate of the Poynting flux into a reconnection region, i.e., $F = v_{inflow} B^2 / (4\pi)$, with $v_{inflow} \approx 0.1v_A$, $B \approx 100$ G, and $v_A \approx 1000$ km s⁻¹, yields a similar value, $F \approx 8 \times 10^9$ erg cm⁻² s⁻¹. Thus, the average Poynting flux during flaring time intervals exceeds that of the steady-state heating of the corona in active regions ($F \lesssim 10^7$ erg) by several orders of magnitude. The total duration of the 172 analyzed flares is $T_{flare} = \sum_{i=1}^{172} T_i = 75.3$ hrs = 2.6×10^5 s, which corresponds to an average flare duration of $\langle T_i \rangle = 0.43$ hr.

We can estimate the time-averaged Poynting flux in active regions by dividing the total sum E_{tot} of all flare-dissipated energies by the average active region area A_{AR} and the total time span T_{tot} of observations, for which we obtain

$$F_{AR} = \frac{E_{tot}}{A_{AR}T_{tot}} = 5.8 \times 10^6 \left(\frac{L_{AR}}{0.1R_{\odot}} \right)^{-2} \quad [\text{erg cm}^{-2}\text{s}^{-1}], \quad (27)$$

where the total energy $E_{tot} = \sum E_i = 3.1 \times 10^{34}$ erg is obtained from summing all dissipated energies of each of the 172 flares (Table 3), the total observing time is $T_{obs} = \sum T_i = 3.5$ years = 1.1×10^8 s, and the active region size $A_{AR} = L^2$ is normalized to the length scale of $L = 0.1R_{\odot} \approx 70,000$ km. Interestingly, this average Poynting flux in active regions is close to the average coronal heating requirement of $F_{heat} \lesssim 10^7$ erg cm⁻² s⁻¹ (Withbroe et al. 1977), which we will discuss in the context of the coronal heating problem in Section 4.6.

4. DISCUSSION

4.1. Measuring the Coronal Magnetic Field

It has often been stated that we have no direct method to measure the coronal magnetic field, except for some special methods that can infer the magnetic field at particular locations only, such as in some layers above sunspots by means of gyroresonance emission (Alissandrakis et al. 1980), in the core of active regions by means of polarized bremsstrahlung (Brosius and Holman 1988), both measured in radio wavelengths, by spectropolarimetry of forbidden coronal lines in infrared (Lin, Kuhn, and Coulter 2004; Judge et al. 2001), or by coronal seismology applied to oscillating loops (Roberts, Edwin, and Benz 1984). With the two NLFFF methods used in this study, however, we have new tools that are able to measure the 3D magnetic field $\mathbf{B}(\mathbf{x})$ in a space-filling coronal volume that encompasses entire active regions. We introduced two methods in Section 2, the PHOT-NLFFF method that uses the 3D magnetic field at the photospheric boundary as input, and the COR-NLFFF method that uses a LOS-magnetogram $B_z(x, y)$ and the projected 2D coordinates of coronal loops. With these two methods, the coronal magnetic field can be measured in principle in the entire corona. However, challenges for the PHOT-NLFFF codes are the non-forcefreeness of the photosphere (DeRosa et al. 2009) and the heavy computational demands (ca. 10-12 hrs per run), while the COR-NLFFF code does not have these problems, but may partially suffer from sparseness of suitable loop structures (uncontaminated by “moss”) in the immediat proximity of sunspots, where the highest field strengths and thus the largest amounts of free energies are measured. Nevertheless, we improved the COR-NLFFF code substantially in recent times and obtained reasonable results of the measured magnetic energies in all analyzed flares. The computational efficiency of the COR-NLFFF code makes it possible to obtain these results fast for a large number of flares and many time steps (in the order of minutes per time step and active region. While the present version of the COR-NLFFF code uses an approximative NLFFF solution in terms of vertical

currents, more accurate NLFFF solutions have been carried out elsewhere (Malanushenko et al. 2014) with similar results (though with manual rather than automated tracing of coronal loops, and with significantly longer computation times).

When we talk about magnetic energies in the solar corona, we have to be aware that there are at least three different quantities that can be measured, which are, in order of increasing difficulty: (i) the potential energy E_p , (ii) the free energy E_{free} , or the non-potential energy which is the sum of the potential and free energy, $E_{np} = E_p + E_{free}$, and (iii) the dissipated energy $E_{diss} = E_{free}(t_2) - E_{free}(t_1)$ during a certain time interval $\Delta t = t_2 - t_1$. All these energies are volume-integrated quantities, $E = \int (dE/dV) dV$, while the energy density (dE/dV) is directly related to the magnetic field by $(dE/dV) = B_\varphi^2/(8\pi)$. The potential energy density $(dE/dV)_p$ is related to the potential field $B_p(x, y, z)$, while the free energy density $(dE/dV)_{free}$ is related to an azimuthal magnetic field component $B_\varphi(x, y, z)$ that is perpendicular to the potential field component $B_p(x, y, z)$, because the definition of the nonpotential field, $E_{np} = E_p + E_{free} = B_p^2 + B_\varphi^2$ implies that B_p and B_φ are perpendicular, according to the Pythagoras' theorem (Aschwanden 2013b). Consequently, the non-potentiality of a magnetic field can easily be inferred from the misalignment angle $\mu = \arctan(B_\varphi/B_p)$ between the potential $B_p(x, y, z)$ and non-potential field $B_{np}(x, y, z)$. This misalignment angle is constant along a uniformly helically twisted field line, which corresponds to a constant α -value of a nonlinear force-free field, and thus constitutes a nonlinear force-free field (NLFFF) solution. Since the automated tracing of coronal loops yields a direct measurement of the projected misalignment angle μ_2 in a 2D image observed in soft X-rays or EUV, the COR-NLFFF method is particularly sensitive to deviations of the nonpotential field from the potential field. Previous assessments of the non-potentiality of active regions were mostly based on visual inspection of EUV images and overlaid potential field lines (e.g., Schrijver et al. 2005).

What is the accuracy of our modeling of the coronal magnetic field? While the potential field B_r (Eqs. B1 and D2) is a zero-order approximation of the coronal magnetic field, the azimuthal field B_φ (Eq. D3) due to helical twist is a first-order approximation, the associated free energy $E_{free} \propto B_\varphi^2$ is a second-order effect, and the decreases of free energy during a flare, which we call the dissipated energy, is a third-order effect. In Table 3 we provide uncertainties for all these measured magnetic quantities. For the potential field energy, we find a scatter of $\sigma_B/B_p = 0.05 \pm 0.12$ ($\approx 5\%$), which includes the variation of the potential energy during a flare time interval as well as the uncertainty in the forward-fitting of a NLFFF solution. Comparing the COR-NLFFF with the PHOT-NLFFF code (Table 4), we find a similar degree of accuracy, namely $E_p^{PHOT}/E_p^{COR} = 1.05 \pm 0.33$ ($\approx 5\%$). For the free energy, which is a second-order effect, we find an agreement of $E_{free}^{PHOT}/E_{free}^{COR} = 2.8 \pm 2.0$ (or a factor of $\lesssim 3$) (Table 4), which includes methodical differences between both codes, such as uncertainties of the transverse field component of the vector magnetograms and spatial averaging effects due to pre-processing in the PHOT-NLFFF method, as well as sparseness of suitable loops free of moss contamination in the proximity of sunspots and separation problems of closely-spaced mixed magnetic polarities in the COR-NLFFF method. Even more important, for the dissipated energy, which is a third-order effect, we find an agreement of $E_{diss}^{PHOT}/E_{diss}^{COR} = 0.5 \pm 0.4$ (or a factor of 2) between the two methods. We note that the COR-NLFFF code is more sensitive than the PHOT-NLFFF code, and detects a significant amount of dissipated energy in all of the 172 analyzed flares, with a significance ratio of $\sigma_{E,diss}/E_{diss} = 10 \pm 8$. As a caveat, we have to add that these results were derived under the assumption that all decreases in the free energy during a flare time interval are due to energy dissipation, and that all energy increases during a flare time interval are due to illumination effects (such as by chromospheric evaporation), an assumption that we will discuss further in the following section.

4.2. Coronal Illumination Effects of Magnetic Structures

As the 60 examples of measurements with the COR-NLFFF code shown in Figs. 5-9 demonstrate, we almost never observe the naively expected scenario of a constantly elevated level of free energy before a flare, followed by a single-step decrease during the impulsive flare phase, with a constant depleted value afterward. On the other side, the PHOT-NLFFF code shows in about half of the cases such a single-step decrease behavior (Figs. 11-12), but detects a significantly smaller decrease of free energy in the other half of the cases (Figs. 11-12), which raises some questions about the sensitivity of the PHOT-NLFFF code. It may be hampered due to the averaging effects of the pre-processing technique (which tries to suppress the non-forcefreeness of the photosphere). So, what can explain this different behaviour in the measurement of free energies of the COR-NLFFF method?

Let us discuss first the positive increases of free energy during flaring time intervals. There are essentially two possibilities: (i) incremental storage of free energy, either by continued twisting of the magnetic field, or by new flux emergence with vertical currents, or (ii) progressive illumination of nonpotential field structures, such as twisted loops, sigmoids, or twisted filaments, manifested as brightening EUV structures, as it can be produced by chromospheric evaporation in the thick-target scenario (e.g., Antonucci et al. 1982; Brown 1972). The first argument can be largely eliminated by the argument of time scales. A statistical study of the nonpotentiality of 95 active regions has lead to the conclusion that the electric currents associated with the nonpotentiality have a characteristic growth and decay time scale of 10-30 hrs. Here we analyze the preflare time interval of 172 flares over a much shorter time margin of 0.5 hrs, which is a factor of 20-60 times shorter than the characteristic growth and decay time of nonpotentiality, and thus it can readily be neglected. Hence, the only obvious alternative explanation of the observed increases of free energy is due to chromospheric evaporation, which can illuminate twisted loop structures in the preflare phase (Fig. 5), during the rise time of the impulsive flare phase (Fig. 6), as well as during the decay time of the impulsive flare phase (Fig. 7). Therefore, we ignore the time intervals with positive increases in the calculations of the dissipated energy (in terms of cumulative decreases of free energy). A sceptic may even raise the argument that positive increases of the free energy could be caused by uncertainties in the forward-fitted NLFFF model. In order to convince ourselves that this is not the case, we repeated each forward-fit with three substantially different sets of loops (see Fig. 2) and obtain error bars that reflect the uncertainty of the forward-fits due to loop selections, but we find that these error bars are in most cases significantly smaller than the cumulative positive energy increases during the flare time interval. This means that the energy increases are due to a systematic effect that is significantly above the random noise of the NLFFF solutions.

What about the measured energy decreases of free energy. Are they all due to energy dissipation, as we assume in our data analysis technique (Fig. 4)? In principle, additional contributions to negative energy steps could arise from (i) decay of nonpotentiality, (ii) cooling of the flare plasma that renders twisted structures (such as sigmoids, helical loops, or twisted filaments) invisible, or (iii) from random fluctuations in the forward-fitting method. Again, we can argue in terms of time scales. Statistical studies of transient magnetic features associated with significant currents in active regions decay on time scales of ≈ 27 hrs (Pevtsov et al. 1994), ≈ 20 hrs (Schrijver et al. 2005), or 1-2 days (Welsch et al. 2011), which is much shorter than the time interval of 0.5 hrs we analyze after flares in our study. The second option of plasma cooling, can also largely be ruled out by the argument of flare decay time scales observed in EUV and soft SXR. Although the theoretical time scales of radiative and conductive cooling for a single loop structure can be in the order of ≈ 0.2 hrs (Rosner et al. 1978; Antiochos 1980, Culhane et al. 1994), the overall cooling time that is observed in a postflare loop system amounts to $T = 0.4 \pm 0.5$ hrs (as averaged from the flare durations listed in Table 3), which is generally longer than the rapid decay times of $\Delta t_{free} \lesssim 0.1$ hr that are seen for

the decreases of free energy (Figs. 5-10). This time scale ratio can be inspected in the 60 time profiles that we show for the evolution of the free energy $E_{free}(t)$ and the GOES light curve $F_{GOES}(t)$ in Figs. 5-10. And the third argument can also be eliminated by the fact that the error bars in the free energy solutions (Figs. 5-10 and Table 3) are generally much lower than the negative energy jumps, which is found to have a significance of $\sigma_{E,diss}/E_{diss} = 10 \pm 8$ (as averaged from Table 3).

Based on these arguments we justify the assumption made in our data analysis that the impulsive increases of free energy are largely due to “coronal illumination effects”, and the rapid energy increases represent the energy dissipation of magnetic energies during flares (as depicted in Fig. 3), which are caused by untwisting and relaxing of field lines after a magnetic reconnection process, according to our model of free energy produced by vertical currents.

4.3. Previous Estimates of Dissipated Flare Energies

Estimates of the free magnetic energy that is partially dissipated in a solar flare have initially been made with the virial theorem, which yields an upper limit of twice the potential energy for a simple dipole field (Metcalf et al. 1995, 2005; Emslie et al. 2012). Other methods include flux-rope modeling (Bobra et al. 2008), which yielded a misalignment angle of $\mu_2 \approx 10^\circ$ between the helical flux rope and the potential field, which translates into a free energy ratio of $E_{free}/E_p = (B_\varphi/B_r)^2 \approx \tan^2(10^\circ) \approx 3\%$. Calculations with nonlinear force-free field (NLFFF) codes using photospheric vector magnetograph data have been carried out in a number of studies, yielding free energy ratios in active regions of $q_{free} = E_{free}/E_p \approx 30\%$ (Metcalf et al. 1995), $q_{free} = 10\%$ (Jiao et al. 1997), $q_{free} = 2\%$ (Guo et al. 2008), a scatter of $q_{free} \approx -12\%$ to $+32\%$ from a test comparison between 14 different NLFFF codes (Schrijver et al. 2008), $q_{free} = 0.6\% - 6.3\%$ (Thalmann et al. 2008), $q_{free} = 9\% - 36\%$ (Thalmann et al. 2013), $q_{free} = 4\% - 32\%$ (Malanushenko et al. 2014), $q_{free} = 14\%$ (Sun et al. 2012). In summary, we can say that the ratio of the free energy to the potential energy is found in a range of $q_{free} \approx 0.4\% - 25\%$. This fits well with our statistical result of 172 flares, where the ratio of free energy is found in a range of $q_{free} \approx 0.6\% - 36\%$ (Fig. 13, top right panel), for potential energies in the range of $E_p \approx 1 \times 10^{31} - 4 \times 10^{33}$ erg. Moreover, we find a scaling law of $E_{free} \propto E_p^{1.73}$ that implies a near-quadratic dependence between the two quantities.

Now, the next question is what fraction of the free energy is dissipated in solar flares, which requires to measure the evolution of the free energy $E_{free}(t)$ during an entire flare event. This is a computationally more challenging task and has been computed only for few cases. Schrijver et al. (2008) compared the free energies calculated by 14 different NLFFF codes before and after a flare, where only two codes yielded a negative decrease of the free energy during the flare, in the amount of $7\% - 13\%$. Guo et al. (2008) measure a decrease of $\approx 2\%$ during an X3.4 flare. Thalmann et al. (2008) measure an energy decrease that corresponds to $q_{free} = 2.3\%$ of the potential energy, which translates into $E_{diss}/E_{free} \approx 38\%$, so about a third of the free energy becomes dissipated during the flare. Malanushenko et al. (2012) obtains free energies in the range of $q_{free} \approx 4\% - 32\%$, but the reference potential field changes during the flare, so that it is not trivial to estimate the dissipated energy during the flare. Sun et al. (2012) provide a detailed study of the evolution of the free energy in active region 11158 over 5 days and find the free energy decreases from $q_{free} = 29\%$ before the flare to $q_{free} = 25\%$ after the flare, so a fraction of $E_{diss}/E_p = 4\% \pm 1\%$ is dissipated, which is about 14% of the available free energy. Thus, these previous studies find that the actually dissipated energy in flares amounts to $E_{diss}/E_{free} \approx 7\% - 38\%$. In a statistical study of 38 eruptive flare events, the dissipated energy in flares was assumed (ad hoc) to a fraction $E_{diss}/E_p \approx 30\%$ (Emslie et al. 2012). In a follow-on study (Aschwanden, Sun, and Liu 2014a) we applied both a PHOT-NLFFF and a COR-NLFFF code, and found

that the PHOT-NLFFF code underestimates the dissipated flare energy by a factor of $\approx 3 - 8$ from C-class to X-class flares, compared with the PHOT-NLFFF code, which is also consistent with the new findings of $E_{diss}^{PHOT}/E_{diss}^{COR} = 0.5 \pm 0.4$ (Table 4). In our statistical study of 172 M and X-class flares here we find that the amount of dissipated energy scales with the potential energy of the active region and follows a scaling of $E_{diss} \propto E_p^{1.56}$ (Eq. 9), which yields a ratio from $E_{diss}/E_{free} \approx 20\%$ at $E_p = 10^{32}$ erg to $E_{diss}/E_{free} \approx 80\%$ at $E_p = 10^{33}$ erg (see also Fig. 13, bottom left). Note that the dissipated energy can exceed 100% of the available free energy using our COR-NLFFF code, because parts of the free energy is hidden in invisible loops that become illuminated around the peak time of the flare only.

4.4. Self-Organized Criticality Models

In this study we obtained for the first time statistical data on the primary form of energy that is dissipated in solar flares. The dissipated magnetic energy is believed to constitute the primary source of energy that supplies both flares as well as coronal mass ejection (CME) phenomena, while the conversion into thermal energies, non-thermal energies, and CME motion represent secondary energy conversion processes, each one consuming a partial amount of the primary energy. Statistics of secondary energy processes in solar flares, such as hard X-ray emission, have been interpreted early on as a manifestation of nonlinear energy dissipation processes that are governed by self-organized criticality (SOC) (Lu and Hamilton 1991), a concept that was originally developed to explain the powerlaws of earthquake magnitude distributions, originally modeled with cellular automaton models and sandpile avalanches (Bak, Tang, and Wiesenfeld 1987). A recent review on the application of this SOC concept in solar and astrophysics summarizes the developments over the last 25 years (Aschwanden et al. 2014b).

We present the occurrence frequency distributions (also known as size distributions, which are generally plotted in $\log(N)$ - $\log(S)$ format) of dissipated magnetic energies (E), peak dissipation rates (P), durations (T), length scales (L), flare areas (A), and volumes (V) in Fig. 15 and present the retrieved powerlaw scalings in Section 3.10. Let us compare these results with the theoretical expectations. The *fractal-diffusive self-organized criticality model (FD-SOC)* (Aschwanden 2012) considers the spatial scale (L) as the most fundamental quantity of SOC systems, which has a scale-free probability distribution of $N(L) \propto L^{-3}$ in Euclidean space dimension $d = 3$, which is not too far from the observed value of $\alpha_L = 3.75 \pm 0.26$ (Fig. 15, top right panel), given the small-number statistics. The associated size distributions for areas are predicted to have values of $\alpha_A = 1 + (d - 1)/2 = 2.0$ and $\alpha_V = 1 + (d - 1)/d = 5/3$ (Aschwanden 2012), which are consistent with our measurements $\alpha_A = 2.08 \pm 0.17$ and $\alpha_V = 1.72 \pm 0.11$ (Fig. 15, right middle and bottom panel). For the dissipated energy E and peak dissipation rate P , the FD-SOC model predicts powerlaw slopes of $\alpha_E = 3/2$ and $\alpha_P = 5/3$, for Euclidean dimension $d = 3$ and classical diffusion ($\beta = 1$). Our observed values are $\alpha_E = 2.00 \pm 0.21$ and $\alpha_P = 2.30 \pm 0.15$, which is somewhat steeper. The simplest version of the FD-SOC model assumes a proportionality between the volume V and total dissipated energy E , which is not exactly true, because the scatterplot in Fig. 14 (bottom right panel) indicates a slight nonlinearity of $V \propto E^{1.16}$, or inversely, $E \propto V^{0.86}$, which can explain the differences to the values predicted by the simplest version of the FD-SOC model. This result constrains physical scaling laws of the energy release process, as we will discuss in the next section.

4.5. Scaling Law of Magnetic Energy Dissipation

Statistics of magnetic parameters can reveal physical scaling laws of the magnetic energy release process, such as a particular type of magnetic reconnection. An exhaustive list of magnetic scaling laws for different types of coronal heating models has been compiled in Mandrini et al. (2000), which includes stressing models with a heating rate produced by stochastic build-up, $E_H \propto B^2 L^{-2} V^2 \tau$ (Sturrock and Uchida 1981), or for stressing models with a critical angle, $E_H \propto B^2 L^{-1} V \tan(\varphi)$ (Parker 1988, Berger 1993), where B is the magnetic field, L the length of a magnetic field line, V the volume, τ the time scale, and φ the critical shearing angle. Our NLFFF model involves a helically twisted field line with vertical currents, for which the scaling law of the dissipated energy is defined as $E_{diss} \propto (B_\varphi)^2 V \propto B^2 \tan^2(\varphi) V$ (Aschwanden 2013b). However, we have to be aware that this represents a microscopic scaling law that applies to one single (helically twisted) magnetic field line, while a macroscopic scaling law represents the integral over the entire volume of an inhomogeneous active region. The microscopic parameters in an inhomogeneous medium average out in such a way that macroscopic parameters, such as the average (azimuthal) magnetic field strength $\langle B_\varphi \rangle$ or the average length scale $\langle L \rangle$ of loops produce a different scaling law. The best we can hope is that the volume integration still preserves some scaling law between the dissipated energy E_{diss} and the maximum field strength $B_{\varphi,max}$ and length scale L_{AR} of an active region. We test such a hypothetical scaling law by defining two a priori unknown exponents β and λ ,

$$E_{diss} = \int \left(\frac{B_\varphi}{8\pi} \right)^2 dV \propto B_{\varphi,max}^\beta L_{AR}^\lambda. \quad (28)$$

Since we measured the maximum field strength $B_{\varphi,max}$ and length scale L_{AR} of flare areas in active regions, we can perform a linear regression fit for this scaling law, which yields a slope γ for an arbitrary choice of β and λ , i.e., $E_{diss} \propto (B_{\varphi,max}^\beta L_{AR}^\lambda)^\gamma$. For the best fit of a hypothetical scaling law we demand a slope of $\gamma = 1$ and a minimum uncertainty σ_γ of the fitted slope, which we can express with the goodness-of-fit criterion χ that needs to be minimized,

$$\chi = (\gamma - 1) + \sigma_\gamma. \quad (29)$$

We calculate a goodness-of-fit map $\chi(\beta, \lambda)$ in the range of $-3 \leq \beta, \lambda \leq +3$ (Fig. 17, top), where we find a minimum value at $\beta = 1.0$ and $\lambda = 1.5$, for a slope of $\gamma = 1.00 \pm 0.16$, with $\chi_{min} = 0.16$. We show the corresponding best fit in Fig. 17 (bottom panel), which reveals a scaling law of

$$E_{diss} \propto B_{\varphi,max}^{1.0} L_{AR}^{1.5}. \quad (30)$$

This scaling law applies also approximately to the dissipated energy in a flare, since we found $E_{diss} \propto E_{free}^{0.9}$ (Eq. 10).

It is interesting to note that this macroscopic scaling law does not preserve the same exponents as the theoretical (microscopic) scaling law predicts for one single twisted field line, i.e., $E_B \propto B^2 L^3$, but only about the half value of the exponents, which is a consequence of the averaging effects over a highly inhomogeneous active region volume. In comparison, a scaling law of $F_H \propto BL^{-1}$ was found for the heating flux F_H from hydrostatic modeling of a multi-loop corona in Schrijver et al. (2004). The heating flux F_H (in units of $\text{erg cm}^{-2} \text{ s}^{-1}$) corresponds to a volumetric heating rate of $H \propto F_H/L \propto BL^{-2}$ (in units of $\text{erg cm}^{-3} \text{ s}^{-1}$), or to a volume-integrated heating energy flux of $E_{heat} = F_H V = F_H L^3 = BL$ (in units of erg s^{-1}). The time-integrated heating energy would then be $E_{heat} = F_{heat} T \propto BLT$ (in units of erg). We find that the flaring time scale T is not significantly correlated with any other parameter, and thus the empirical scaling law $E_{heat} \propto BL$ of Schrijver et al. (2004) is similar to our scaling law of magnetically dissipated energies, $E_{diss} \propto BL^{1.5}$.

4.6. The Coronal Heating Problem

We calculated the Poynting flux during the analyzed energy dissipation episodes (or flares) and found values of $F \approx 5 \times 10^8 - 10^{10}$ erg cm⁻² s⁻¹ that occur temporarily, averaged over the flare duration. If we average these Poynting fluxes over the entire time span of observations (3.5 years) and an average active region area with a length scale of $L_{AR} = 0.1R_{\odot}$, we find an average Poynting flux of $\langle F_{AR} \rangle \approx 5.8 \times 10^6$ erg cm⁻² s⁻¹. This average Poynting flux meets the average coronal heating requirement of active regions, which is commonly quoted as $\langle F_{heat} \rangle \lesssim 10^7$ erg cm⁻² s⁻¹, which is needed to balance the observed conductive and radiative losses from the corona (Withbroe et al. 1977).

We have to be aware that this value of the Poynting flux with a total dissipated magnetic energy of $\sum E_{diss} \approx 3 \times 10^{34}$ erg during 3.5 years represents the energy content of 172 flares with a magnitude of \geq M1.0 GOES class only. As the size distribution of dissipated energies in Fig. 15 (top left panel) shows, the dissipated energies exhibit a distribution with a powerlaw slope of $\alpha_E \approx 2.0 \pm 0.2$ in the range of 10^{32} and 10^{33} erg. If we extend this powerlaw distribution down to the range of nanoflares with energies of $E \gtrsim 10^{24}$ erg (Parker 1988), the total dissipated energy increases only by a factor of

$$\frac{\int_{E_{nano}}^{E_X} E N(E) dE}{\int_{E_M}^{E_X} E N(E) dE} = \frac{\ln(E_X/E_{nano})}{\ln(E_X/E_M)} = 9, \quad (31)$$

based on a size distribution of $N(E) \propto E^{-\alpha_E}$ with a powerlaw slope of $\alpha_E \approx 2$, with lower energy limits of $E_{nano} \approx 10^{24}$ erg for nanoflares, $E_M \approx 10^{32}$ erg for M-class flares, and an upper limit of $E_X \approx 10^{33}$ erg for X-class flares (see Fig. 15 top left panel). Thus, extrapolating the observed energy distribution in the energy range of $[E_M, E_X]$ to the microflare and nanoflare range $[E_{nano}, E_X]$, we estimate a total dissipated magnetic energy that is about a factor of 9 higher, i.e., corresponding to a Poynting flux of $\langle F_{AR} \rangle \approx 4 \times 10^7$ erg cm⁻² s⁻¹. It might be somewhat higher during more active solar cycles, since the observed period of 2010-2014 belongs to a relatively weak solar cycle. All previous estimates of the energy budget for coronal heating were based on thermal energies or non-thermal energies (e.g., Crosby et al. 1993; Shimizu 1995), which appear to be only a lower limit to the magnetic energy budget (Emslie et al. 2008). This explains that some of those global energy estimates were found to be slightly below the coronal heating requirement (see discussion in Section 9.8.3 of Aschwanden 2004).

In conclusion we find that the magnetic energy dissipated during solar flares is sufficient to explain the coronal heating problem in active regions. Since most parts of the Quiet Sun (essentially all parts of the closed-field corona) are magnetically connected with active regions, the heating of the Quiet Sun can equally be explained as a by-product of plasma heating in active regions. Only coronal hole regions, which are not magnetically connected with active regions, require a different mechanism to explain a (low) coronal temperature ($T_e \lesssim 0.8$ MK) in such open-field regions. We conclude that the dissipated magnetic energies in solar flares, which are measured here with unprecedented statistics, represent the most relevant constituent to identify the energy source of coronal heating. Our results support the view that the solar corona is largely heated by impulsive magnetic energy dissipation processes that reduce the helical twist of the stressed coronal magnetic field during solar flares, most likely facilitated by a magnetic reconnection process.

5. CONCLUSIONS

We started a project on the global energetics of solar flares, using the most recent data from the SDO mission, which contains about 400 GOES M and X-class flares during the first 3.5 years of the mission. In

this first study we measure the magnetic energy that is dissipated during solar flares, for 172 events that are located within a longitude of $\leq 45^\circ$ from disk center. The major results and conclusions can be summarized as follows.

1. We are using two complementary nonlinear forcefree field (NLFFF) codes to measure the dissipated energies during flares. The PHOT-NLFFF code uses the vector magnetic field (from HMI/SDO) measured at the photospheric boundary and extrapolates the forcefree field after pre-processing in order to improve the forcefreeness condition. The COR-NLFFF code uses the line-of-sight (LOS) magnetic field component B_z from magnetograms (from HMI/SDO) and the geometry of coronal loops as measured in EUV images (from AIA/SDO) in six coronal wavelengths. The numerical procedure of the COR-NLFFF code consists of 3 major steps: (i) the decomposition of the magnetogram into buried magnetic charges that define the potential field, (ii) automated tracing of coronal loops to obtain the projected 2D coordinates of coronal loops, and (iii) forward-fitting of an analytical NLFFF approximation, which is based on vertical currents that twist coronal loops, by varying the nonlinear forcefree α -parameters of the nonpotential field until the misalignment between the model field lines and the observed loop directions is minimized. The average misalignment angle of all forward-fits is $\mu_2 = 8.6^\circ \pm 2.1^\circ$.
2. We measure the evolution of the potential energy $E_p(t)$, the free energy $E_{free}(t)$, and the dissipated energy $E_{diss}(t)$ during 172 flare events. While the PHOT-NLFFF code mostly detects a step-wise decrease of the free energy during most flares, the COR-NLFFF code detects both increases and decreases of the free energy during flares. We interpret the episodes of increasing free energy as “coronal illumination effects” of twisted loop structures during the impulsive flare phase (such as by chromospheric evaporation), while the episodes with decreasing free energies indicate the dissipation of magnetic energies, which can occur before flare start, during the impulsive flare phase, and sometimes are even detected during the flare decay phase.
3. Comparing the COR-NLFFF with the PHOT-NLFFF code, which could be done only for 11 X-class flares due to computational time limitations, we find that the potential and nonpotential energies agree within a few percents for the average of all cases, but vary by a factor of $\lesssim 1.4$ for individual flares, which corresponds to a factor of $\lesssim 1.2$ in the magnetic field. The agreement of the free energies varies by a factor of $q_{free} = 3.3 \pm 2.3$, which could be due to model assumptions of the COR-NLFFF code (vertical currents with helical twist cannot reproduce horizontally twisted structures), or numerical procedures (pre-processing and heliographic deprojection) of the PHOT-NLFFF code. The dissipated energies, which is a third-order effect of the magnetic field model, agree within a factor of $q_{diss} = 0.5 \pm 0.4$ between the two codes, where the COR-NLFFF code is more sensitive and detects decreases of the free energy in all 172 analyzed flares.
4. From the statistics of 172 events analyzed with the COR-NLFFF code we find the following empirical scaling laws between the magnetic potential energies (E_p), nonpotential energies (E_{np}), the free energies (E_{free}), and the dissipated energies (E_{diss}): $E_{np} \propto E_p^{1.02}$, $E_{free} \propto E_p^{1.73}$, $E_{diss} \propto E_p^{1.56}$, and $E_{diss} \propto E_{free}^{0.89}$. The mean twist angle in a flaring active region is related to the potential energy of the active region by the relationship: $\tan(\varphi) \approx (E_{free}/E_p)^{1/2} \approx 1.2^\circ (E_p/10^{30} \text{ erg})^{0.37}$. This relationship allows us to predict the magnitude of the largest flare to occur in an active region based on the average twist angle (or misalignment angle to the potential field). Furthermore we found a semi-empirical scaling law between the dissipated energy E_{free} , the maximum (azimuthal) magnetic field strength $B_{\varphi,max}$, and the length scale L_{AR} of the active region: $E_{free} \propto B_{\varphi}^{1.0} L^{1.5}$, which is similar to a scaling law found by Schrijver et al. (2004) for coronal heating, i.e., $E_{heat} \propto BL$.

5. The size distributions, which we derive here for the first time for magnetic parameters, are found to have the following powerlaw slopes: $\alpha_E = 2.0 \pm 0.2$ for dissipated energies, $\alpha_P = 2.3 \pm 0.2$ for the peak energy dissipation rate, $\alpha_T = 2.4 \pm 0.2$ for the flare duration, $\alpha_L = 3.8 \pm 0.3$ for flare length scales, $\alpha_A = 2.1 \pm 0.2$ for flare areas, and $\alpha_V = 1.7 \pm 0.1$ for flare volumes. The flare volume $V = L^3$ and the dissipated flare energy E_{diss} are found to scale as $V \propto E_{diss}^{1.16}$. These results are approximately consistent with the predictions of the fractal-diffusive self-organized criticality (FD-SOC) model. Since SOC models describe the statistics of nonlinear energy dissipation processes, the measurement of primary energy parameters, such as the dissipated magnetic energy measured here, are more important than secondary energy parameters, such as thermal or nonthermal energies in solar flares that have been subjected to SOC models previously.
6. The Poynting fluxes of dissipated magnetic energies are found to have values in the range of $F \approx 5 \times 10^8 - 10^{10} \text{ erg cm}^{-2} \text{ s}^{-1}$ during flare time intervals. The sum of all magnetic energies dissipated in solar flares is $E_{tot} \approx 3 \times 10^{34} \text{ erg}$ during the 3.5 years of observations, yields a temporally and spatially averaged flux of $P \approx 6 \times 10^6 \text{ erg cm}^{-2} \text{ s}^{-1}$ for a mean active region size of $L = 0.1 R_\odot$, and of $P \approx 4 \times 10^7 \text{ erg cm}^{-2} \text{ s}^{-1}$ when extrapolated down to the nanoflares. This amount of dissipated magnetic energies is sufficient to explain coronal heating in active regions (and quiet-Sun regions). Previous estimates of the global energy budget of the solar corona were based on thermal and nonthermal energies, which represent lower limits to the dissipated magnetic energy only and thus underestimate coronal heating rate. Our results support the view that the solar corona is largely heated by impulsive magnetic energy dissipation processes that reduce the helical twist of the stressed coronal magnetic field during solar flares.

The comparison between two completely different NLFFF codes has demonstrated that both codes yield commensurable results (within a factor of ≈ 3), which gives us more confidence in either code. In future studies we will calculate other forms of energies obtained during flares, such as thermal energies of the heated flare plasma, non-thermal energies of accelerated hard X-ray producing particles, and kinetic energies of CMEs. We will investigate whether those secondary energy products add up to the total dissipated magnetic energies inferred here, and what the relative energy partition in the various flare processes is. The unprecedented statistics of flare energies may reveal the underlying physical scaling laws that govern flares and CME processes.

We thank the referee for insightful comments and we appreciate helpful discussions with Bart De Pontieu, Mark DeRosa, Brian Dennis, Gordon Emslie, Allen Gary, Anna Malanushenko, Aidan O’Flannagain, Karel Schrijver, Daniel Ryan, Manuela Temmer, Astrid Veronig, and Brian Welsch. Part of the work was supported by NASA contract NNG 04EA00C of the SDO/AIA instrument and the NASA STEREO mission under NRL contract N00173-02-C-2035. YX and JJ are supported by NSF AGS-1345513, 1153424, NASA NNX11AQ55G and NNX13AG13.

APPENDIX A: Automated Tracing of Coronal Loops

The key input of the COR-NLFFF code is the geometry of coronal loops, which can be measured in 2D images in form of cartesian coordinates $[x(s), y(s)]$ as a function of a loop length coordinate s from highpass-filtered EUV images, or in form of 3D coordinates $[x(s), y(s), z(s)]$ from stereoscopic reconstruction. In

principle, 3D coordinates would be preferable because they provide stronger and more unique constraints for any type of loop modeling (Aschwanden 2009, 2011; Aschwanden et al. 2008a, 2008b, 2009a, 2012a, 2012b), but the inferior spatial resolution of the EUVI/STEREO imagers (Wülser et al. 2004), compared with AIA/SDO (Lemen et al. 2012), and the restricted time range suitable for small-angle stereoscopy (Aschwanden et al. 2012) make it impractical.

There exists a (Grad-Rubin method) COR-NLFFF code that calculates a NLFFF solution by fitting the geometry of coronal loops (Malanushenko et al. 2009, 2011, 2012, 2014), but its application is restricted to manually traced loops and was applied to very few flares only. Therefore, automated loop tracing is a prerequisite for efficient and objective NLFFF forward-fitting codes. The pioneering phase of automated coronal loop tracing started with an initial comparison of the performance of five different methods (Aschwanden et al. 2008c). One of these codes, the *Oriented Coronal CURved Loop Tracing (OCCULT)* code, was further developed by specializing the automated pattern recognition of curvi-linear features to the geometric property of large curvature radii, which achieved a performance close to visual perception (Aschwanden 2010). The guiding criterion of the oriented-directivity method for curvi-linear tracing was then further refined by including second-order terms (OCCULT-2; Aschwanden, DePontieu, and Katrukha 2013). In a recent study with AIA/SDO data, the automated loop tracing was extended to all available 7 coronal wavelengths (94, 131, 171, 193, 211, 304, 335 Å; Lemen et al. 2012), and the effect of loop selection in different filters on the NLFFF solution was investigated (Aschwanden et al. 2014).

The basic steps of the OCCULT-2 automated loop tracing code are: (a) read EUV images in 6 coronal wavelengths and apply a highpass-filter (with a typical highpass boxcar of $nsm_1 = 3$ and lowpass boxcar of $nsm_2 = 5$); (b) evaluation of a flux threshold based on the flux mean and standard deviations in 10×10 macropixels; (c) automated tracing using the control parameters of: minimum curvature $r_{min} = 25$ pixels, minimum structure length $l_{min} = 25$ pixels; maximum gap along coherent structure $n_{gap} = 3$ pixels, and threshold of $q_{thresh,2} = 3$ times the median flux of the background; (d) coordinate transformation of pixel units into units of solar radii relative to Sun center; and (e) rejection of unwanted loop structures.

From previous experience we learned that the convergence of a forward-fit of a NLFFF solution can be substantially degraded if there is a significant amount of false loop structures. It is therefore imperative to remove as many false loop structures as possible, when using an automated pattern recognition code. In the present study we improved the loop selection criteria further by automated feature detection of 6 types of false loop structures that are visible in EUV images.

(1) Curvi-linear structures that have no footpoint directly connected to a magnetic source (sunspot or magnetic flux concentration in the magnetogram) are likely to be false loop structures, because most coronal loops are best visible at their footpoints, where usually the maximum of the electron density, emission measure, and EUV brightness occurs, due to the hydrostatic stratification. We detect such unwanted loop structures by the following magnetic proximity requirement,

$$[(x_{foot,i} - x_{mag,j})^2 + (y_{foot,i} - y_{mag,j})^2]^{1/2} \leq d_{foot} = 0.015 R_{\odot}, \quad (A1)$$

where $(x_{foot,i}, y_{foot,i})$ is the starting point ($i = 1$) or end point ($i = n_s$) of a curvi-linear structure, and $(x_{mag,j}, y_{mag,j}), j = 0, \dots, n_m$ is the image position of the next buried magnetic charge (decomposed from the line-of-sight magnetograms) of any of the n_m magnetic charges. About 3.7% of automatically detected curvi-linear structures do not meet the magnetic proximity condition (Table 1).

(2) Parts of some AIA/SDO images contain saturated pixels at the datanumber limit (i.e., $> 2^{14}$ DN/s in 2-byte encoded images), which can produce curvi-linear features along the boundaries of saturated

areas in the CCD images (often occurring during the peak time of flares), which is found in about 0.3% of automatically detected structures (see Fig. 18; red curves).

(3) Saturated images display also “bleeding pixels”, which are manifested in form of vertical streaks in the CCD readout, which we found to produce about 0.1% false loop structures (Table 1).

(4) EUV images of active regions display often “moss structure” (Berger et al. 1999), which is a reticulated spongy fine structure that indicates the footpoint transition regions of hot coronal loops. Often, cooler coronal loops overlay fields with moss structures, which produces a ripple of the EUV flux profile $F(s)$ along the loop. Moreover, chains of moss dots often form a curved structure by chance coincidence and lead to false loop detections. We eliminate such false moss structure by a ripple criterion,.

$$q_f = \frac{1}{(n_s - 1)} \sum_{i=0}^{n_s} \frac{|F(s_i) - F(s_{i+1})|}{\max[F_{s_i}, F_{s_{i+1}}]} \leq q_{ripple} , \quad (A2)$$

which essentially quantifies the average degree of fluctuations, modulation depth, or smoothness of a flux profile $F(s)$ along the loop coordinate $0 < s < L$. Flux profiles that are absolutely smooth have a ripple ratio of $q_f \approx 0$, while strongly fluctuating flux profiles have a maximum ripple ratio of $q_f \lesssim 1.0$. We perform three types of runs (RUN1, RUN2, RUN3) with different ripple ratio limits of $q_f < 0.25$, 0.50, or 0.75, respectively. The ripple ratio limit has the biggest influence on the number of selected loops, ranging from 22% for smooth loops with $q_f \leq 0.25$ (RUN1) to 80% for very inhomogeneous loops with $q_f \geq 0.75$ (RUN3) (Table 1). We apply the ripple criterion only to short structures ($L \leq 2l_{min} = 50$ pixels $\approx 0.03R_\odot$), because longer structures are much less likely to form a regularly curved loop structure by chance coincidence (Fig. 18; green curves).

(5) A particular instrumental effect is the diffraction pattern that occurs from the EUV entrance mesh filter at high brightness levels during flares, which is detected from a clustering of directivity angles either in parallel or perpendicular direction in a directivity histogram. This applies to about 1.9% of the automatically detected loops (Table 1).

(6) After calculating a potential field $\mathbf{B}_p(s)$, we can measure the 2D misalignment angles between the potential field (projected in the plane-of-sky) and the automatically traced loops. Structures that have a large 2D misalignment angle to the potential field, say $\mu_2 > 45^\circ$, are unlikely to fit a non-potential field, which we discard also in the forward-fitting of our NLFFF model. This is the case in about 1.4% of the automatically detected loops (Table 1).

Some examples of such automatically detected structures are shown in Fig. 18, including coronal loop structures (blue curves), rippled (moss) structures (green curves), and boundaries of saturated image areas (red curves).

APPENDIX B: Potential Field Parameterization

In contrast to standard potential field codes, which generally extrapolate a potential field using the eigenfunction (spherical harmonic) expansion (Green’s function) method, originally derived by Altschuler & Newkirk (1969) and Sakurai (1982), the COR-NLFFF code deconvolves a line-of-sight magnetogram into a finite number of buried unipolar magnetic charges (Aschwanden & Sandman 2010). The chief advantage of the magnetic charge decomposition method is that it automatically provides also a suitable parameterization for NLFFF solutions with vertical currents, which can be defined for each unipolar magnetic charge and can be forward-fitted efficiently.

The decomposition of a potential field into uni-polar magnetic charges is defined in terms of $m = 1, \dots, n_m$ sub-photospheric locations (x_m, y_m, z_m) and a vertical field strength B_m at the photospheric surface, vertically above the buried magnetic charge. The field strength $B(r)$ of each unipolar magnetic source decreases with the square of the radial distance r . A arbitrary large number n_m of magnetic charges can be superimposed, which yield the resulting potential field \mathbf{B}_p ,

$$\mathbf{B}_p(\mathbf{x}) = \sum_{m=1}^{N_m} \mathbf{B}_m(\mathbf{x}) = \sum_{m=1}^{N_m} B_m \left(\frac{d_m}{r_m} \right)^2 \frac{\mathbf{r}_m}{r_m}, \quad (B1)$$

where $r_m = [(x-x_m)^2 + (y-y_m)^2 + (z-z_m)^2]^{1/2}$ is the distance of an arbitrary coronal location $\mathbf{x} = (x, y, z)$ to the subphotospheric charge location (x_m, y_m, z_m) , while $d_m = 1 - [x_m^2 + y_m^2 + z_m^2]^{1/2}$ is the depth of the buried charge, and B_m is the magnetic field strength at the solar surface in vertical direction above the buried charge. The square-dependence of the radial field component $B(r) \propto r^{-2}$ warrants that each magnetic charge fulfills Maxwell's divergence-free condition,

$$\nabla \cdot \mathbf{B} = 0, \quad (B2)$$

which it is also true for the summed magnetic field according to Eq. (B1), because the linear superposition of divergence-free fields is divergence-free too, i.e., $\nabla \cdot \mathbf{B} = \nabla \cdot (\sum_m \mathbf{B}_m) = \sum_m (\nabla \cdot \mathbf{B}_m) = 0$.

The decomposition of a LOS magnetogram $B_z(x, y)$ into a finite number n_m of magnetic charges is carried out by iterative decomposition of local maxima of the magnetic field into individual magnetic charges, each one yielding four model parameters, $(B_m, x_m, y_m, z_m), m = 1, \dots, n_m$. The numerical procedure is demonstrated in Aschwanden and Sandman (2010), and an analytical treatment is derived in Appendix A of Aschwanden et al. (2012a).

We start with the absolute peak in the magnetogram, which is measured at the location (x_p, y_p) and has the value B_z for the LOS component of the magnetic field vector. We extract then a local magnetogram map around this peak that has an extension of $(w \times w)$, where w corresponds to the numerically determined full width at a level of 25% of the peak flux. From the observables (B_z, x_p, y_p) and the variable d_m for the depth of the buried magnetic charge we can calculate the projected disk center distance ρ_p , the LOS coordinate z_p at the photospheric height, the angle α between the LOS and solar surface vertical, the angle β_p between the solar surface vertical and the LOS field component B_z , which yield then the field strength B_m and the coordinates $(x_m, y_m, z_m, r_m, \rho_m)$ of the buried magnetic charge m (see Fig. 19 and Eqs. A1-A11 in Aschwanden et al. (2012a),

$$\begin{aligned} \rho_p &= \sqrt{(x_p^2 + y_p^2)} \\ z_p &= \sqrt{1 - \rho_p^2} \\ \alpha &\approx \arctan(\rho_p/z_p) \\ \gamma &= \arctan(y_p/x_p) \\ \beta &= \arctan \left[\left(\sqrt{9 + 8 \tan^2 \alpha} - 3 \right) / 4 \tan \alpha \right] \\ B_m &= B_z / [\cos^2 \beta \cos(\alpha - \beta)] \\ r_m &= (1 - d_m) \\ \rho_m &= \rho_p - d_m \sin(\alpha - \beta) / \cos \beta \\ z_m &= \sqrt{r_m^2 - \rho_m^2} \\ x_m &= \rho_m \cos \gamma \\ y_m &= \rho_m \sin \gamma \end{aligned} \quad (B3)$$

While the width w was obtained as a direct observable in Aschwanden et al. (2012a), we found a more robust procedure here by varying the depth parameter d_m until the spatially integrated unsigned magnetic flux of

the local peak map yields the best match between the model and the observed local map $B_z(x, y)$,

$$\Phi = \int |B_z^{obs}(x, y)| dx dy = \int |B_z^{model}(x, y; w)| dx dy . \quad (B4)$$

In this way we obtain an inversion of the observables (B_z, x_p, y_p) and by varying d_m to find the model parameters (B_m, x_m, y_m, z_m) . After the deconvolution of the global maximum in the magnetogram, which yields the first 4 parameters of the model map, we subtract the model distribution $B_z(x, y)$ of the first magnetic source and continue in the same way by iterating additional magnetic source components. Since the magnetogram has positive and negative magnetic field values, the iteration is performed at the unsigned magnetogram, while the correct sign of the magnetic polarity is applied to each deconvolved component. Typically, a number of $n_m \approx 100$ magnetic sources is sufficient to obtain a realistic potential field model of a solar active region. In the end we renormalize the total unsigned magnetic flux of the model magnetogram to that of the observed magnetogram, in order to compensate for numerical residuals, which is typically in the order of a few percents. An example of a unipolar magnetic charge decomposition is shown in Fig. 20, for the same observation as shown in Fig. 18 (first panel). Note the negligible difference (Fig. 20 top right) between the observed (Fig. 20, top left) and the model magnetogram (Fig. 20, bottom left), which is also visualized with a 1D-scan across the sunspot with maximum magnetic field strength (Fig. 20, bottom right).

APPENDIX C: Rotational Invariance of Magnetic Fields

Most of the existing PHOT-NLFFF codes require a cartesian coordinate system with a planar boundary at the bottom of the computation box, oriented in perpendicular direction to the line-of-sight of the observed magnetogram. Active regions with a heliographic position that are some distance away from Sun center are therefore de-rotated to the disk center and remapped using the Lambert (cylindrical) equal-area projection (see also Sun et al. 2012 and references therein). Since the accuracy of the LOS component B_z is much higher than that of the transverse components (B_x, B_y) , a de-rotation of the magnetogram implies also a variable weighting in the accuracy of the horizontal and vertical magnetic field components. In the extreme case of an active region near the solar limb, the horizontal field component B_x is measured with the highest accuracy, while the other horizontal component B_y and the vertical component B_z are measured much less accurately. The accuracy of measuring vertical currents thus varies considerably from center to limb. To our knowledge, no validation test has been done to demonstrate whether a NLFFF solution is invariant to the heliographic position, or whether there is a center-to-limb dependency.

In contrast, the COR-NLFFF code takes the full sphericity of the solar surface into account and no de-rotation of magnetograms is required. Since the COR-NLFFF code uses only the observed LOS component of the magnetogram to infer the potential field solution, which is measured with highest accuracy, and does not require the knowledge of the transverse components, which are measured with much less accuracy, the inferred potential field solution should be invariant to solar rotation to first order, as long as small-scale magnetic sources are neglected that suffer from degraded spatial resolution due to projection effects near the limb. We perform a validation test of this rotational invariance hypothesis in Fig. 21. A bipolar active region is simulated at various longitudes from 0° to 80° (Fig. 21 top panels) to mimic observed magnetograms. Then we decompose the simulated LOS magnetogram $B_z^{obs}(x, y)$ into two magnetic sources, and calculate a model map $B_z^{model}(x, y)$, from which we show the profiles $B_z(x)$ along the East-West direction x (Fig. 21, middle panels). Then we calculate the ratio of the magnetic energies from the observed and the model map,

$$q_E = \frac{\int B_{z,model}^2(x, y) dx dy}{\int B_{z,obs}^2(x, y) dx dy} = \frac{\int B_{model}^2(x, y) dx dy}{\int B_{obs}^2(x, y) dx dy} \quad (C1)$$

and find a mean ratio of $q_E = 1.000 \pm 0.024$ when averaged over the different longitudes (Fig. 21, bottom panel). This result proves that the magnetic potential field energy is conserved and invariant to the solar rotation or center-limb-distance, as computed with our COR-NLFFF code. The accuracy starts to degrade at longitudes $\gtrsim 80^\circ$, which corresponds to a projected distance of $\sin(80^\circ) \approx 0.98$ solar radii. Thus, our code is able to calculate potential field solutions for a fraction of $\approx 90\%$ of active regions that are observed on the solar disk.

APPENDIX D: Forward-Fitting of Non-Potential Fields

The COR-NLFFF code is designed to forward-fit an approximate NLFFF solution in terms of vertical currents to the geometry of coronal loops. We use the same parameterization of the potential field solution \mathbf{B}_p as described above (Eq. B1), i.e., (B_m, x_m, y_m, z_m) for $m = 1, \dots, n_m$, but add a nonpotential parameter, the so-called force-free α -parameter, so that we have 5 variables for each magnetic source, i.e., $(B_m, x_m, y_m, z_m, \alpha_m)$. This force-free α -parameter represents a helical twist of the non-potential field lines about a vertical axis, for each magnetic charge. Requiring a force-free solution that fulfills Maxwell's equation,

$$\mathbf{j}/c = \frac{1}{4\pi}(\nabla \times \mathbf{B}) = 0, \quad (D1)$$

we calculated an analytical approximation in spherical coordinates (r, φ, θ) (Aschwanden 2013a),

$$B_r(r, \theta) = B_0 \left(\frac{d^2}{r^2} \right) \frac{1}{(1 + b^2 r^2 \sin^2 \theta)}, \quad (D2)$$

$$B_\varphi(r, \theta) = B_0 \left(\frac{d^2}{r^2} \right) \frac{br \sin \theta}{(1 + b^2 r^2 \sin^2 \theta)}, \quad (D3)$$

$$B_\theta(r, \theta) \approx 0, \quad (D4)$$

$$\alpha(r, \theta) \approx \frac{2b \cos \theta}{(1 + b^2 r^2 \sin^2 \theta)}. \quad (D5)$$

$$b = \frac{2\pi N_{twist}}{L}, \quad (D6)$$

that is accurate to second-order in the parameter α or $r \sin(\theta)$. While these equations are expressed in a spherical coordinate system that is aligned along the axis r with the solar vertical, the sphericity of the Sun is taken into full account by transforming the coordinates from each magnetic charge system into a common cartesian coordinate system that has the z -axis aligned with the observer's line-of-sight. The resulting nonpotential field \mathbf{B}_{np} is then summed from all magnetic charges,

$$\mathbf{B}_{np}(\mathbf{x}) = \sum_{m=1}^{N_m} \mathbf{B}_m(\mathbf{x}), \quad (D7)$$

which is also accurate to second-order in the parameter α . In the limit of $\alpha_m = 0$, this solution degenerates to a potential field solution (Eq. B1),

The numerical fitting technique of the nonpotential field $\mathbf{B}_n(\mathbf{r})$ to observed loop coordinates (x_s, y_s) has been initially described in Aschwanden & Malanushenko (2013b) and was gradually improved over time. Essentially, the nonpotential model parameters $\alpha_m, m = 1, \dots, n_m$ have to be optimized until they match the observed loop geometries, while the potential model parameters $(B_m, x_m, y_m, z_m), m = 1, \dots, n_m$ are left

unchanged. The convergence criterion of the forward-fitting method is a minimum value of the median misalignment angle $\mu(\mathbf{x})$ between theoretical field lines and observed loop geometries (Sandman et al. 2009; Aschwanden and Sandman 2010; Sandman and Aschwanden 2011) at a number of locations \mathbf{x} ,

$$\mu(\mathbf{x}) = \cos^{-1} \left(\frac{\mathbf{B}^{theo}(\mathbf{x}) \cdot \mathbf{B}^{obs}(\mathbf{x})}{|\mathbf{B}^{theo}(\mathbf{x})| |\mathbf{B}^{obs}(\mathbf{x})|} \right). \quad (D8)$$

where \mathbf{x} refers to a number of loop positions, for which we choose $n_{seg} = 9$ loop segments. The misalignment angle can be defined in 2D (μ_2), or in 3D (μ_3), but we will use only the 2D values μ_2 here, since we are not using any observational information from the third (line-of-sight) coordinate.

The current version of the COR-NLFFF forward-fitting code, for which we list the settings of the standard control parameters in Table 2, contains the following major steps:

1. Initialization of force-free parameter α_m : The initial guess of the variables start with the potential-field value $\alpha_m = 0$, if no near-simultaneous NLFFF solution exists, while previous solutions of $\alpha_m \neq 0$ are used for time series with $n_t \geq 2$ time frames. This strategy warrants more continuity of the NLFFF solution for sequential calculations with small time steps (say with time steps of $\Delta t \approx 0.1$ hour). Most of the magnetic energy is contained in the strongest sources, typically the 10 strongest magnetic sources contain about 90% of the magnetic energy. Therefore we need to vary only a subset of values α_m that correspond to the strongest magnetic sources, say $n_{nlfff} \approx 10$ for $B_m \gtrsim 0.1 B_{max}$, which represent $E_B \gtrsim 0.01 E_{max}$, and thus about 99% of the magnetic energy. Moreover we apply also a minimum distance criterion (d_{foot}) between nonpotential magnetic charges, in order to avoid magnetic flux cancellation of spatially overlapping magnetic sources with opposite magnetic polarity. A typical separation distance requirement of $d_{foot} \geq 0.015 R_\odot$ reduces the maximum number of magnetic charges (n_m), used in the decomposition of the magnetogram, to $n_{nlfff} \approx 20 - 50$ values of α_m , which yields also a more unique solution and speeds up the convergence of the forward-fitting code.
2. Optimization of 3D loop geometry: Since the loop tracing method provides 2D coordinates $[x(s), y(s)]$ only, while 3D coordinates $[x(s), y(s), z(s)]$ are required to enable forward-fitting with a 3D NLFFF model, we have to estimate the third coordinate $z(s)$ for each loop position in every forward-fitting iteration cycle. We estimate the 3D geometry of loops by using a circular geometry for each fitted loop segment, parameterized by a loop curvature radius r_{loop} , a loop apex altitude h_{loop} , and two footpoint locations at either end of the traced loop segments (Fig. 22). We perform for each loop a global search of the minimum 2D misalignment angle μ_2 within a physically plausible range (e.g., $h_{loop} \leq h_{max} = 0.2 R_\odot$, $L \leq r_{loop} \leq h_{max}$, where L is the detected projected loop length and h_{max} is the altitude of the computation box). The reconstruction of the best-fit 3D loop geometry is updated with every optimization cycle of α -values. Alternative methods to parameterize the 3D coordinates of coronal loops include cubic Bézier curves (Gary et al. 2014a,b).
3. Optimization of force-free parameters α_m : Each value α_m of the n_{nlfff} (strongest and well-separated) magnetic source components is optimized by minimizing the 2D misalignment angle $\mu_2(\mathbf{x})$ between the nonpotential field $\mathbf{B}_{np}(\mathbf{x})$ and the automatically traced loop segments $B_{obs}[x(s), y(s)]$, where \mathbf{x} refers to different loop positions (typically $n_{seg} = 9$ segments) and different loops synthesized from all 6 coronal AIA filters (typically $n_{loop} \approx 200 - 500$ for one time frame). The median value of this misalignment angle $\langle \mu \rangle$ is minimized by at least $n_{iter,min} = 25$ iteration cycles of all α values and all selected loops (n_{loop}). The α_m minimization is accomplished with a *direction set (Powell's) method in multi-dimensions* (Press et al. 1986, p.294), which calculates in each iteration cycle all

gradients $(\partial\mu/\partial\alpha_m)$ produced by each magnetic source, and improves the next iteration value by $\alpha_m^{new} = \alpha_m^{old} - \Delta\alpha_0(\partial\mu/\partial\alpha_m)/max[(\partial\mu/\partial\alpha_m)]$, which optimizes the misalignment angles by $\mu^{new} = \mu^{old} + \Delta\alpha_0(\partial\mu/\partial\alpha_m)$.

The final result of a NLFFF solution is contained in a set of coefficients $(B_m, x_m, y_m, z_m, \alpha_m), m = 1, \dots, n_{nlfff}$, from which a volume-filling NLFFF solution $\mathbf{B}_{np} = [B_x(x, y, z), B_y(x, y, z), B_z(x, y, z)]$ can be computed in the entire computation box. Individual field lines can be calculated from any starting point (x, y, z) by sequential extrapolation of the local B-field vectors in both directions, until the field line hits a boundary of the computation box.

REFERENCES

- Alissandrakis, C.E., Kundu, M.R., and Lantos, P. 1980, *A&A* 82, 30.
- Altschuler, M.D. and Newkirk, G.Jr. 1969, *Solar Phys.* 9, 131.
- Antiochos, S.K. 1980, *ApJ* 241, 385.
- Antonucci, E., Gabriel, A.H., Acton, L.W., Culhane, J.L., Doyle, J.G., Leibacher, J.W., Machado, M.E., Orwig, L.E., Rapley, C.G. 1982, *Solar Phys.* 78, 107.
- Aschwanden, M.J. 2014, 2004, *Physics of the Solar Corona - An Introduction*, Praxis Publishing Ltd., Chichester UK, and Springer, New York, ISBN 3-540-22321-5, First Edition, hardbound issue, 842p.
- Aschwanden, M.J., Wuelser, J.P., Nitta, N., and Lemen, J. 2008a, *ApJ* 679, 827.
- Aschwanden, M.J., Nitta, N.V., Wuelser, J.P., and Lemen, J.R. 2008b, *ApJ* 680, 1477.
- Aschwanden, M.J., Lee, J.K., Gary, G.A., Smith, M., and Inhester, B. 2008c, *Solar Phys.* 248, 359.
- Aschwanden, M.J. 2009, *Space Sci. Rev.* 149, 31.
- Aschwanden, M.J., Wuelser, J.-P., Nitta, N.V., Lemen, J.R., and Sandman, A. 2009a, *ApJ* 695, 12.
- Aschwanden, M.J., Nitta, N.V., Wuelser, J.-P., Lemen, J.R., Sandman, A., Vourlidis, A., and Colaninno, R.C. 2009b, *ApJ* 706, 376.
- Aschwanden, M.J. 2010, *Solar Phys.* 262, 399.
- Aschwanden, M.J. and Sandman, A.W. 2010, *Astron.J.* 140, 723.
- Aschwanden, M.J. 2011, *Living Rev. Solar Phys.* 8, 5.
- Aschwanden, M.J., Wülser, J.P., Nitta, N.V., Schrijver, C.J., DeRosa, M., and Malanushenko, A. 2012a, *ApJ* 756, 124.
- Aschwanden, M.J., Wuelser, J.P., Nitta, N.V., and Lemen, J.R. 2012b, *Solar Phys.* 281, 101.
- Aschwanden, M.J. 2012c, *A&A* 539, A2 (15p).
- Aschwanden, M.J. 2013a, *Solar Phys.* 287, 323.
- Aschwanden, M.J. 2013b, *Solar Phys.* 287, 369.
- Aschwanden, M.J. 2013c, *ApJ* 763, 115.
- Aschwanden, M.J. and Malanushenko, A. 2013, *Solar Phys.* 287, 345.
- Aschwanden, M.J., De Pontieu, B., and Katrukha, E.A. 2013, *Entropy* 15, 3007.
- Aschwanden, M.J., Sun, X.D., and Liu, Y., 2014a, *ApJ* 785, 34.

- Aschwanden, M.J., Crosby, N., Dimitropoulou, M., Georgoulis, M.K., Hergarten, S., McAteer, J., Milovanov, A., Mineshige, S., Morales, L., Nishizuka, N., Pruessner, G., Sanchez, R., Sharma, S., Strugarek, A., and Uritsky, V. 2014b *Space Science Reviews* (online first) DOI 10.1007/s11214-014-0054-6.
- Bak, P., Tang, C., and Wiesenfeld, K. 1987, *PhRvL* 59/4, 381.
- Berger, M.A. 1993, *PhRvL* 70/6, 705.
- Berger, T.E., DePontieu, B., Fletcher, L., Schrijver, C.J., Tarbell, T.D., and Title, A.M. 1999, *Solar Phys.* 190, 409.
- Bevington, P.R. and Robinson, D.K. 1992, *Data reduction and error analysis for the physical sciences*. McGraw Hill: Boston.
- Bobra, M.G., VanBallegoijen, A.A., and DeLuca, E.E. 2008, *ApJ* 672, 1209.
- Boerner, P., Edwards, C., Lemen, J., Rausch, A., Schrijver, C., Shine, R., Shing, L., Stern, R., Tarbell, T., Title, A., Wolfson, C.J., Soufli, R., Spiller, E., Gullikson, E., McKenzie, D., Windt, D., Golub, L., Podgorski, W., Testa, P., and Weber, M. 2012, *Solar Phys.* 275, 41.
- Brosius, J.W. and Holman, G.D. 1988, *ApJ* 327, 417.
- Brown, J.C. 1972, *Solar Phys.* 26, 441.
- Culhane, J.L., Phillips, A.T., Inda-Koide, M., Kosugi, T., Fludra, A., Kurokawa, H., Makishima, K., Pike, C.D., Sakao, T., Sakurai, T., Doschek, G.A., and Bentley, R.D. 1994, *Solar Phys.* 153, 307.
- Dennis, B.R. and Zarro, D.M. 1993, *Solar Phys.* 146, 177.
- DeRosa, M.L., Schrijver, C.J., Barnes, G., Leka, K.D., Lites, B.W., Aschwanden, M.J., Amari, T., Canou, A., McTiernan, J.M., Regnier, S., Thalmann, J., Valori, G., Wheatland, M.S., Wiegelmann, T., Cheung, M.C.M., Conlon, P.A., Fuhrmann, M., Inhester, B., and Tadesse, T. 2009, *ApJ* 696, 1780.
- Emslie, A.G., Kucharek, H., Dennis, B. R., Gopalswamy, N., Holman, G.D., Share, G.H., Vourlidas, A., Forbes, T.G., Gallagher, P.T., Mason, G.M., Metcalf, T.R., Mewaldt, R.A., Murphy, R.J., Schwartz, R.A., and Zurbuchen, T.H. 2004, *JGR (Space Physics)*, 109, A10, A10104.
- Emslie, A.G., Dennis, B.R., Holman, G.D., and Hudson, H.S., 2005, *JGR (Space Physics)*, 110, 11103.
- Emslie, A.G., Dennis, B.R., Shih, A.Y., Chamberlin, P.C., Mewaldt, R.A., Moore, C.S., Share, G.H., Vourlidas, A., and Welsch, B.T. 2012, *ApJ* 759, 71.
- Gary, G.A., Hu, Q., Lee, J.K., and Aschwanden, M.J. 2014a, *Solar Phys.* 289, 3703.
- Gary, G.A., Hu, Q., and Lee, J.K. 2014b, *Solar Phys.* 289, 847.
- Guo, Y, Ding, M.D., Wiegelmann, T., and Li, H. 2008, *ApJ* 679, 1629.
- Hoeksema, J.T., Liu, Y., Hayashi, K., Sun, X., Schou, J., Couvidad, S., Norton, A., Bobra, M., Centeno, R., Leka, K.D., Barnes, G., and Turmon, M. 2014, *Solar Phys.* 289, 3483.
- Jiao, L., McClymont, A.N., and Mikic, Z. 1997, *Solar Phys.* 174, 311.
- Jing, J., Tan, C., Yan, Y., Wang, B., Wiegelmann, T., Xu, Y., and Wang, H. 2010, *ApJ* 713, 440.
- Judge, P.G., Casini, R., Tomczyk, S., Edwards, D.P., and Francis, E. 2001, *Coronal magnetometry: a feasibility study*, NCAR TN-466+STR (Technical memo).
- Lemen, J.R., Title, A.M., Akin, D.J., Boerner, P.F., Chou, C., Drake, J.F., Duncan, D.W., Edwards, C.G., et al. 2012, *Solar Phys.* 275, 17.
- Lin, H., Kuhn, J.R., and Coulter, R. 2004, *ApJ* 613, L177.

- Lu, E.T. and Hamilton, R.J. 1991, ApJ 380, L89.
- Malanushenko, A., Longcope, D. W., and McKenzie, D.E. 2009, ApJ 707, 1044.
- Malanushenko, A., Yusuf, M.H., and Longcope, D.W., 2011, ApJ 736, 97.
- Malanushenko, A., Schrijver, C.J., DeRosa, M.L., Wheatland, M.S., and Gilchrist, S.A. 2012, ApJ 756, 153.
- Malanushenko, A., Schrijver, C.J., DeRosa, M.L., and Wheatland, M.S. 2014, ApJ 783, 102.
- Mandrini, C.H., Demoulin, P. and Klimchuk, J.A. 2000, ApJ 530, 999.
- Metcalf, T.R., Jiao, L., Uitenbroek, H., McClymont, A.N., and Canfield, R.C. 1995, ApJ 439, 474.
- Metcalf, T.R., Leka, K.D., and Mickey, D.L. 2005, ApJ 623, L53.
- Parker, E.N. 1988, ApJ 330, 474.
- Pesnell, W.D., Thompson, B.J., and Chamberlin, P.C. 2011, Solar Phys. 275, 3.
- Pevtsov, A.A., Canfield, R.C., and Metcalf, T.R. 1994, ApJ 425, L117.
- Press, W.H., Flannery, B.P., Teukolsky, S.A., and Vetterling, W.T. 1986, *Numerical recipes, The Art of Scientific Computing*, Cambridge University Press: Cambridge.
- Roberts, B., Edwin, P.M., and Benz, A.O. 1984, ApJ 279, 857.
- Rosner, R., Tucker, W.H., and Vaiana, G.S. 1978, ApJ 220, 643.
- Sakurai, T. 1982, Solar Phys. 76, 301.
- Sandman, A., Aschwanden, M.J., DeRosa, M., Wuelser, J.P. and Alexander, D. 2009, Solar Phys. 259, 1.
- Sandman, A.W. and Aschwanden, M.J. 2011, Solar Phys. 270, 503.
- Scherrer, P.H., Schou, J., Bush, R.I., Kosovichev, A.G., Bogart, R.S., Hoeksema, J.T., Liu, Y., Duvall, T.L., Zhao, J., Title, A.M., Schrijver, C.J., Tarbell, T.D., and Tomczyk, S. 2012, Solar Phys. 275, 207.
- Schrijver, C.J., Sandman, A.W., Aschwanden, M.J., and DeRosa, M.L. 2004, ApJ 615, 512.
- Schrijver, C.J., DeRosa, M.L., Title, A.M., and Metcalf, T.R. 2005, ApJ 628, 501.
- Schrijver, C.J., DeRosa, M.L., Metcalf, T., Barnes, G., Lites, B., Tarbell, T., McTiernan, J., Valori, G., Wiegelmann, T., Wheatland, M.S., Amari, T., Aulanier, G., Demoulin, P., Fuhrmann, M., Kusano, K., Regnier, S., and Thalmann, J.K. 2008, ApJ 675, 1637.
- Shibata, K. and Yokoyama, T. 1999, ApJ 526, L49.
- Shimizu, T. 1995, PASJ 47, 251.
- Sturrock, P.A. and Uchida, Y. 1981, ApJ 246, 331.
- Sun, X., Hoeksema, J.T., Liu, Y., Wiegelmann, T., Hayashi, K., Chen, Q., and Thalmann, J. 2012, ApJ 748, 77.
- Thalmann, J.K., Wiegelmann, T., and Raouafi, N.E. 2008, A&A 488, L71.
- Thalmann, J.K., Tiwari, S.K., and Wiegelmann, T. 2013, ApJ 769, 59.
- Uritsky, V.M., Klimas, A.J., Vassiliadis, D., Chua, D., and Parks, G. 2002, JGR (Space Physics), 107/A12, 1426, doi:10.1029/2001JA000281.
- Vourlidas, A., Howard, R. A., Esfandiari, E., Patsourakos, S., Yashiro, S., and Michalek, G. 2010, ApJ 722, 1522.
- Welsch, B.T., Christe, S., and McTiernan, J.M. 2011, Solar Phys. 274, 131.

- Wiegelmann, T. 2004, *Solar Phys.* 219, 87.
- Wiegelmann, T., Inhester, B., and Sakurai, T. 2006, *Solar Phys.* 233, 215.
- Wiegelmann, T., Thalmann, J.K., Schrijver, C.J., DeRosa, M.L., and Metcalf, T.R. 2008, *Solar Phys.* 247, 249.
- Wheatland, M.S., Sturrock, P.A. and Roumeliotis, G. 2000, *ApJ*, 540, 1150.
- Wheatland, M.S. and Regnier, S. 2009, *ApJ* 700, L88.
- Withbroe, G.L. and Noyes, R.W. 1977, *ARAA* 15, 363.
- Wuelser, J.P., Lemen, J.R., Tarbell, T.D., Wolfson, C.J., Cannon, J.C., Carpenter, B.A., Duncan, D.W., Gradwohl, G.S., Meyer, S.B., et al. 2004, *SPIE* 5171, 111.

Table 1. Statistics of automated feature detection in analyzed data. Three different runs (RUN1, RUN2, RUN3) have been executed with different thresholds in the flux profile smoothness criterion ($q_{ripple} \leq 0.25$, 0.50, and 0.75).

Feature type	Number All	Percentage All	Percentage RUN1	Percentage RUN2	Percentage RUN3
Ripple criterion q_{ripple}			≤ 0.25	≤ 0.50	≤ 0.75
Number of runs	6				
Number of wavelengths	6				
Number of flares	172				
Number of time frames	2,584				
Number of detected loops	6,900,000	100.0%	100.0%	100.0%	100.0%
Number of fitted loops	1,500,000	22.4%	22.4%	46.2%	79.8%
Number of eliminated loops:					
- magnetic proximity	260,000	3.7%	3.7%	6.0%	10.2%
- saturated pixels	19,000	0.3%	0.3%	0.5%	0.7%
- pixel bleeding	10,000	0.1%	0.1%	0.3%	0.5%
- rippled flux profile (moss)	4,800,000	70.2%	70.2%	42.8%	1.0%
- diffraction pattern	130,000	1.9%	1.9%	1.9%	3.1%
- misalignment ($> 45^\circ$)	930,000	1.4%	1.4%	2.3%	4.7%

Table 2. Standard control parameters of COR-NLFFF code used in this study.

Symbol	Parameter
	<u>Instruments :</u>
HMI/SDO	Magnetograms
AIA/SDO	EUV images
$\Delta_{HMI} = 0.0005R_{\odot}$	Spatial resolution HMI magnetogram
$\Delta_{EUV} = 0.0015R_{\odot}$	Spatial resolution AIA image
$\lambda = 94, 131, 171, 193, 211, 335 \text{ \AA}$	Wavelengths of EUV images
FOV = $0.35 R_{\odot}$	Field-of-view
	<u>Automated Loop Tracing :</u>
$r_{min} = 25$ EUV pixels	Minimum loop curvature radius
$l_{min} = 25$ EUV pixels	Minimum loop segment length
$n_{gap} = 3$ EUV pixels	Maximum gap with zero flux along loop
$n_{thresh} = 3$	Significance level of noise threshold
$n_{sig} = 4$	Significance level of diffraction pattern
$n_{point} = 200$	Maximum number of points per loop
$n_{loop} = 200$	Maximum number of loops per wavelengths
$n_{high} = 3$	Highpass filter boxcar
$n_{low} = 5$	Lowpass filter boxcar
$\Delta s = 0.002R_{\odot}$	Spatial resolution of loop length coordinate
$q_{ripple} = 0.25, 0.50, 0.75$	Loop flux profile ripple criterion
$\mu = 45^{\circ}$	Maximum tolerated misalignment angle
	<u>Magnetogram Decomposition :</u>
$n_m = 100$	Maximum number of magnetic charges
$\Delta_m = 3\Delta_{HMI}$	Spatial resolution of decomposed magnetogram
$d_{foot} = 0.015R_{\odot}$	Footpoint separation of magnetic charges
$d_{prox} = 0.015R_{\odot}$	Magnetic proximity requirement of loop footpoints
	<u>Forward-Fitting Algorithm :</u>
$n_{iter,min} = 25$	Minimum number of iteration cycles
$n_{iter,max} = 100$	Maximum number of iteration cycles
$n_{seg} = 9$	Number of loop segments
$h_{min} = \Delta s/2$	Minimum altitude
$h_{max} = 0.2R_{\odot}$	Maximum altitude of computation box
$n_{dim} = 2$	Dimension of misalignment angle
$\Delta\alpha_0 = 1/R_{\odot}$	Increment of force-free parameter α
	<u>Time Series Forward-Fitting :</u>
$dt = 0.1$ hr	Time step of EUV multi-wavelength dataset
$t_{margin} = 0.5$ hr	Margin of preflare and postflare time window
$lon_{max} = 45^{\circ}$	Maximum longitude difference to central meridian

Table 3. Magnetic energy parameters calculated with the COR-NLFFF code for 172 M and X-class flares with a longitude difference of $< 45^\circ$ to the central meridian.

#	Flare start time	GOES class	Helio-position graphic	Mis-align angle (deg)	Potential energy E_p (10^{30} erg)	Free energy E_{free} (10^{30} erg)	Energy ratio E_{free}/E_p	Dissipated energy E_{diss} (10^{30} erg)	Peak dissipation rate P_{diss} (10^{30} erg /0.2 hr)	Length scale L (Mm)	Duration T (hrs)
3	2010-08-07 17:55	M1.0	N13E34	4.0°	311 ± 8	6 ± 3	0.050	15 ± 1	9 ± 1	31 ± 1	0.87
4	2010-10-16 19:07	M2.9	S18W26	4.0°	202 ± 6	9 ± 4	0.138	27 ± 6	15 ± 4	20 ± 1	0.13
10	2011-02-13 17:28	M6.6	S21E04	3.4°	842 ± 19	23 ± 8	0.101	85 ± 20	47 ± 15	25 ± 4	0.32
11	2011-02-14 17:20	M2.2	S20W07	3.5°	1154 ± 14	96 ± 12	0.069	79 ± 11	47 ± 11	30 ± 2	0.20
12	2011-02-15 01:44	X2.2	S21W12	4.4°	1065 ± 14	52 ± 20	0.113	120 ± 10	53 ± 11	49 ± 3	0.37
13	2011-02-16 01:32	M1.0	S22W27	4.2°	823 ± 18	128 ± 17	0.136	111 ± 7	45 ± 8	38 ± 4	0.23
14	2011-02-16 07:35	M1.1	S23W30	4.6°	930 ± 19	172 ± 26	0.230	213 ± 44	82 ± 19	65 ± 6	0.33
15	2011-02-16 14:19	M1.6	S23W33	4.4°	855 ± 22	140 ± 53	0.217	185 ± 11	93 ± 12	50 ± 4	0.17
16	2011-02-18 09:55	M6.6	N15E05	3.4°	875 ± 16	8 ± 3	0.016	13 ± 2	11 ± 3	33 ± 6	0.33
17	2011-02-18 10:23	M1.0	N17E07	3.3°	936 ± 19	12 ± 5	0.022	20 ± 3	14 ± 4	40 ± 2	0.23
19	2011-02-18 14:00	M1.0	N17E04	3.5°	1016 ± 39	16 ± 6	0.026	26 ± 3	24 ± 7	40 ± 2	0.25
20	2011-02-18 20:56	M1.3	N15E00	3.4°	956 ± 18	11 ± 4	0.016	15 ± 1	14 ± 4	37 ± 5	0.30
22	2011-02-28 12:38	M1.1	N22E35	5.5°	428 ± 17	15 ± 12	0.070	29 ± 7	29 ± 10	21 ± 2	0.42
27	2011-03-07 13:45	M1.9	N11E21	4.0°	1135 ± 24	11 ± 7	0.044	50 ± 8	27 ± 9	36 ± 6	1.18
37	2011-03-09 23:13	X1.5	N10W11	4.3°	1790 ± 23	149 ± 38	0.150	268 ± 26	142 ± 3	41 ± 2	0.27
38	2011-03-10 22:34	M1.1	N10W25	4.0°	1618 ± 26	151 ± 55	0.173	280 ± 12	138 ± 34	38 ± 4	0.25
39	2011-03-12 04:33	M1.3	N07W41	4.6°	1172 ± 20	34 ± 16	0.096	112 ± 20	52 ± 12	41 ± 2	0.25
44	2011-03-25 23:08	M1.0	S18E34	3.8°	1200 ± 48	130 ± 21	0.109	131 ± 7	52 ± 8	34 ± 3	0.37
45	2011-04-15 17:02	M1.3	N13W24	3.6°	1427 ± 23	31 ± 10	0.022	31 ± 7	17 ± 6	22 ± 1	0.43
46	2011-04-22 04:35	M1.8	S19E40	3.8°	713 ± 29	21 ± 7	0.064	45 ± 9	20 ± 7	19 ± 2	0.65
47	2011-04-22 15:47	M1.2	S19E34	4.6°	1005 ± 46	74 ± 41	0.229	229 ± 16	152 ± 43	53 ± 6	0.40
52	2011-07-27 15:48	M1.1	N20E41	4.0°	313 ± 9	7 ± 5	0.104	32 ± 4	17 ± 2	22 ± 2	0.57
53	2011-07-30 02:04	M9.3	N16E35	5.0°	575 ± 21	33 ± 12	0.163	93 ± 22	55 ± 20	32 ± 2	0.13
54	2011-08-02 05:19	M1.4	N16W11	5.8°	1018 ± 28	64 ± 36	0.112	114 ± 21	96 ± 13	29 ± 5	1.48
55	2011-08-03 03:08	M1.1	N15W23	5.7°	793 ± 15	25 ± 18	0.027	21 ± 1	12 ± 3	32 ± 1	0.72
56	2011-08-03 04:29	M1.7	N16E10	4.0°	1855 ± 17	290 ± 41	0.124	230 ± 26	106 ± 29	79 ± 9	0.10
57	2011-08-03 13:17	M6.0	N17W30	5.7°	741 ± 17	68 ± 28	0.113	84 ± 4	44 ± 13	33 ± 5	0.88
58	2011-08-04 03:41	M9.3	N18W36	4.8°	600 ± 16	54 ± 28	0.191	114 ± 12	56 ± 8	31 ± 3	0.38
65	2011-09-06 01:35	M5.3	N15W03	4.6°	1213 ± 33	33 ± 19	0.093	112 ± 14	64 ± 20	38 ± 3	0.50
66	2011-09-06 22:12	X2.1	N16W15	4.7°	922 ± 24	49 ± 34	0.203	187 ± 9	97 ± 21	30 ± 5	0.20
67	2011-09-07 22:32	X1.8	N16W30	4.7°	582 ± 17	89 ± 16	0.161	93 ± 7	50 ± 16	19 ± 4	0.20
68	2011-09-08 15:32	M6.7	N17W39	4.5°	508 ± 18	89 ± 28	0.265	134 ± 4	75 ± 7	31 ± 1	0.33
89	2011-09-25 08:46	M3.1	N14E43	4.8°	1477 ± 467	136 ± 98	0.379	560 ± 70	288 ± 49	63 ± 4	0.10
91	2011-09-25 15:26	M3.7	N15E39	4.7°	1620 ± 55	245 ± 68	0.283	458 ± 85	265 ± 67	47 ± 4	0.20
92	2011-09-25 16:51	M2.2	N16E38	4.2°	1788 ± 74	265 ± 95	0.113	202 ± 33	131 ± 21	44 ± 6	0.30
93	2011-09-26 05:06	M4.0	N15E35	4.5°	2207 ± 34	350 ± 85	0.322	710 ± 169	355 ± 102	74 ± 12	0.12
94	2011-09-26 14:37	M2.6	N16E25	4.7°	2164 ± 86	302 ± 98	0.110	237 ± 49	157 ± 50	47 ± 10	0.42
96	2011-09-30 18:55	M1.0	N11E08	4.2°	686 ± 21	9 ± 7	0.037	25 ± 5	17 ± 3	30 ± 1	0.33
97	2011-10-01 08:56	M1.2	N10W03	4.5°	660 ± 255	62 ± 34	0.110	72 ± 6	51 ± 19	31 ± 0	1.35
98	2011-10-02 00:37	M3.9	N10W13	5.4°	771 ± 14	78 ± 17	0.081	62 ± 6	30 ± 8	31 ± 3	0.37
111	2011-11-05 11:10	M1.1	N22E43	2.7°	2742 ± 100	207 ± 62	0.107	294 ± 47	133 ± 31	37 ± 4	0.53
112	2011-11-05 20:31	M1.8	N21E37	2.9°	3356 ± 91	83 ± 33	0.049	163 ± 19	80 ± 13	31 ± 3	0.38
113	2011-11-06 00:46	M1.2	N22E34	3.0°	3572 ± 80	125 ± 50	0.067	239 ± 36	177 ± 51	38 ± 3	0.63
114	2011-11-06 06:14	M1.4	N21E31	3.3°	3656 ± 77	102 ± 71	0.040	146 ± 41	126 ± 26	53 ± 8	0.45

Table 3—Continued

#	Flare start time	GOES class	Helio- position graphic	Mis- align angle (deg)	Potential energy E_p (10^{30} erg)	Free energy E_{free} (10^{30} erg)	Energy ratio E_{free} $/E_p$	Dissipated energy E_{diss} (10^{30} erg)	Peak dissipation rate P_{diss} (10^{30} erg /0.2 hr)	Length scale L (Mm)	Duration T (hrs)
115	2011-11-09 13:04	M1.1	N20E36	5.0°	989 ± 32	24 ± 11	0.014	14 ± 1	10 ± 1	36 ± 5	1.13
117	2011-11-15 12:30	M1.9	S19E36	4.1°	333 ± 8	7 ± 6	0.101	33 ± 4	23 ± 6	26 ± 1	0.33
119	2011-12-25 18:11	M4.0	S20W26	4.9°	235 ± 9	5 ± 2	0.048	11 ± 2	4 ± 1	13 ± 0	0.15
120	2011-12-26 02:13	M1.5	S18W34	4.5°	210 ± 11	3 ± 0	0.045	9 ± 0	3 ± 0	20 ± 1	0.38
121	2011-12-26 20:12	M2.3	S18W44	4.9°	320 ± 90	7 ± 8	0.079	25 ± 4	22 ± 8	23 ± 1	0.40
126	2011-12-31 16:16	M1.5	S22E42	3.9°	926 ± 31	59 ± 20	0.177	163 ± 29	102 ± 29	33 ± 2	0.30
130	2012-01-19 13:44	M3.2	N32E24	4.7°	1204 ± 42	251 ± 66	0.354	426 ± 30	179 ± 14	50 ± 2	4.10
131	2012-01-23 03:38	M8.7	N30W21	5.0°	828 ± 20	50 ± 31	0.059	48 ± 9	28 ± 4	24 ± 3	0.93
138	2012-03-05 19:27	M1.8	N16E45	5.9°	1358 ± 673	242 ± 281	0.691	938 ± 150	777 ± 111	28 ± 0	0.08
139	2012-03-05 22:26	M1.3	N16E43	6.1°	1473 ± 532	237 ± 197	0.882	1299 ± 70	785 ± 103	160 ± 16	0.27
140	2012-03-06 00:22	M1.3	N18E42	6.0°	1775 ± 541	159 ± 152	0.478	848 ± 11	555 ± 67	236 ± 6	0.15
141	2012-03-06 01:36	M1.2	N18E41	5.6°	1545 ± 38	59 ± 32	0.125	193 ± 33	119 ± 37	33 ± 3	0.23
142	2012-03-06 04:01	M1.0	N18E39	4.4°	1609 ± 48	92 ± 45	0.170	273 ± 32	210 ± 32	55 ± 11	0.12
143	2012-03-06 07:52	M1.0	N18E40	4.6°	1634 ± 37	95 ± 75	0.287	469 ± 74	256 ± 84	77 ± 6	0.13
144	2012-03-06 12:23	M2.1	N21E40	5.6°	1781 ± 556	304 ± 265	0.868	1546 ± 110	1021 ± 69	84 ± 13	0.52
145	2012-03-06 21:04	M1.3	N18E32	6.0°	1795 ± 20	253 ± 54	0.186	333 ± 24	140 ± 28	71 ± 4	0.17
146	2012-03-06 22:49	M1.0	N18E32	6.0°	1720 ± 39	212 ± 75	0.139	239 ± 70	148 ± 40	49 ± 9	0.37
147	2012-03-07 00:02	X5.4	N18E31	7.5°	1740 ± 32	198 ± 66	0.158	275 ± 46	164 ± 42	55 ± 4	0.63
148	2012-03-07 01:05	X1.3	N18E29	7.9°	1780 ± 34	168 ± 55	0.113	200 ± 9	146 ± 3	39 ± 1	0.30
149	2012-03-09 03:22	M6.3	N17W00	5.2°	1815 ± 55	211 ± 65	0.080	144 ± 29	73 ± 18	31 ± 3	0.93
150	2012-03-10 17:15	M8.4	N16W21	4.5°	1459 ± 30	110 ± 23	0.039	57 ± 13	63 ± 15	25 ± 2	1.25
152	2012-03-14 15:08	M2.8	N14E07	3.8°	355 ± 9	5 ± 2	0.039	13 ± 2	8 ± 2	22 ± 2	0.47
153	2012-03-15 07:23	M1.8	N16W04	1.8°	131 ± 156	2 ± 3	0.000	0 ± 0	0 ± 0	0 ± 0	0.75
154	2012-03-17 20:32	M1.3	S25W28	3.7°	319 ± 10	11 ± 4	0.089	28 ± 1	14 ± 2	20 ± 1	0.17
157	2012-04-27 08:15	M1.0	N13W26	3.8°	324 ± 7	2 ± 0	0.014	4 ± 1	2 ± 0	24 ± 2	0.23
164	2012-05-09 12:21	M4.7	N13E29	4.1°	2522 ± 35	77 ± 66	0.117	295 ± 54	169 ± 24	50 ± 4	0.25
165	2012-05-09 14:02	M1.8	N12E29	3.8°	2640 ± 41	97 ± 46	0.091	239 ± 38	129 ± 43	46 ± 5	0.20
166	2012-05-09 21:01	M4.1	N13E24	4.1°	3039 ± 51	114 ± 98	0.115	349 ± 22	216 ± 61	56 ± 3	0.13
167	2012-05-10 04:11	M5.7	N12E19	3.8°	3189 ± 65	42 ± 30	0.045	145 ± 27	121 ± 43	39 ± 7	0.20
168	2012-05-10 20:20	M1.7	N12E10	3.9°	3180 ± 44	34 ± 10	0.040	128 ± 16	45 ± 10	27 ± 1	0.17
170	2012-06-03 17:48	M3.3	N15E33	3.6°	731 ± 14	23 ± 11	0.062	45 ± 4	23 ± 6	38 ± 6	0.15
171	2012-06-06 19:54	M2.1	S18W04	4.1°	562 ± 16	46 ± 8	0.096	53 ± 6	26 ± 4	36 ± 5	0.32
175	2012-06-13 11:29	M1.2	S18E21	4.0°	1755 ± 73	407 ± 110	0.173	303 ± 41	141 ± 42	62 ± 2	3.03
176	2012-06-14 12:52	M1.9	S19E06	3.7°	2534 ± 85	634 ± 109	0.122	310 ± 77	221 ± 55	76 ± 4	3.07
178	2012-06-29 09:13	M2.2	N15E37	5.3°	337 ± 9	12 ± 22	0.289	97 ± 4	79 ± 4	35 ± 1	0.15
179	2012-06-30 12:48	M1.0	N15E21	5.5°	370 ± 14	9 ± 6	0.109	40 ± 5	23 ± 5	25 ± 4	0.10
180	2012-06-30 18:26	M1.6	N14E18	5.1°	422 ± 10	11 ± 5	0.095	40 ± 3	23 ± 3	25 ± 1	0.13
181	2012-07-01 19:11	M2.8	N15E04	5.2°	642 ± 20	25 ± 13	0.104	66 ± 9	45 ± 10	31 ± 4	0.17
182	2012-07-02 00:26	M1.1	N15E01	6.0°	668 ± 24	48 ± 30	0.098	65 ± 9	42 ± 4	33 ± 3	0.23
183	2012-07-02 10:43	M5.6	S17E06	3.9°	1641 ± 34	155 ± 56	0.039	63 ± 10	118 ± 25	35 ± 8	0.23
184	2012-07-02 19:59	M3.8	S17E00	4.8°	1713 ± 50	148 ± 56	0.072	123 ± 20	70 ± 21	29 ± 1	0.23
185	2012-07-02 23:49	M2.0	S16W09	4.4°	884 ± 15	75 ± 21	0.120	106 ± 8	51 ± 16	28 ± 3	0.23
186	2012-07-04 04:28	M2.3	S18W18	3.8°	1872 ± 29	221 ± 65	0.064	119 ± 30	93 ± 38	32 ± 3	0.28
187	2012-07-04 09:47	M5.3	S17W18	4.2°	1993 ± 24	186 ± 41	0.083	166 ± 46	117 ± 38	28 ± 6	0.17

Table 3—Continued

#	Flare start time	GOES class	Helio- position graphic	Mis- align angle (deg)	Potential energy E_p (10^{30} erg)	Free energy E_{free} (10^{30} erg)	Energy ratio E_{free} $/E_p$	Dissipated energy E_{diss} (10^{30} erg)	Peak dissipation rate P_{diss} (10^{30} erg /0.2 hr)	Length scale L (Mm)	Duration T (hrs)
188	2012-07-04 12:07	M2.3	S17W19	4.1°	2011 ± 39	164 ± 52	0.073	147 ± 33	82 ± 28	45 ± 5	0.42
189	2012-07-04 14:35	M1.3	S18W20	3.6°	2052 ± 50	143 ± 67	0.026	53 ± 6	46 ± 16	24 ± 3	0.12
190	2012-07-04 16:33	M1.8	N14W33	4.5°	498 ± 28	7 ± 3	0.057	28 ± 5	11 ± 2	27 ± 4	0.25
191	2012-07-04 22:03	M4.6	S16W28	4.0°	2095 ± 48	160 ± 38	0.058	121 ± 16	66 ± 18	29 ± 2	0.20
192	2012-07-04 23:47	M1.2	S19W28	4.0°	1935 ± 42	164 ± 63	0.035	68 ± 14	37 ± 14	22 ± 3	0.25
193	2012-07-05 01:05	M2.4	S19W29	4.2°	1887 ± 29	120 ± 58	0.033	62 ± 16	47 ± 23	26 ± 4	0.17
194	2012-07-05 02:35	M2.2	S18W26	3.9°	1892 ± 21	186 ± 75	0.071	133 ± 14	113 ± 10	44 ± 6	0.20
195	2012-07-05 03:25	M4.7	S18W29	4.4°	2007 ± 26	194 ± 76	0.083	166 ± 49	75 ± 34	25 ± 5	0.23
196	2012-07-05 06:49	M1.1	S17W29	4.5°	2029 ± 32	166 ± 67	0.063	127 ± 15	60 ± 13	25 ± 1	0.27
197	2012-07-05 07:40	M1.3	S18W30	4.2°	2029 ± 34	141 ± 50	0.048	96 ± 17	80 ± 19	27 ± 2	0.13
198	2012-07-05 10:44	M1.8	S18W30	3.9°	1917 ± 39	63 ± 44	0.030	56 ± 11	33 ± 13	42 ± 5	0.10
199	2012-07-05 11:39	M6.1	S18W32	4.1°	1946 ± 52	86 ± 43	0.067	129 ± 24	95 ± 23	33 ± 2	0.17
200	2012-07-05 13:05	M1.2	S18W36	4.1°	1866 ± 32	167 ± 81	0.063	118 ± 3	83 ± 19	37 ± 3	0.45
201	2012-07-05 20:09	M1.6	S18W39	3.8°	1755 ± 28	99 ± 43	0.068	118 ± 19	89 ± 28	33 ± 5	0.32
202	2012-07-05 21:37	M1.6	S18W41	4.0°	1707 ± 31	67 ± 34	0.101	172 ± 21	114 ± 24	39 ± 9	0.23
203	2012-07-06 01:37	M2.9	S18W43	3.8°	1502 ± 507	34 ± 23	0.048	72 ± 8	36 ± 8	48 ± 2	0.08
206	2012-07-06 10:24	M1.8	S17W44	3.2°	1555 ± 36	44 ± 29	0.026	40 ± 7	35 ± 8	39 ± 1	0.13
217	2012-07-09 23:03	M1.1	S17E38	6.1°	3278 ± 56	635 ± 167	0.258	847 ± 120	383 ± 89	93 ± 2	0.13
218	2012-07-10 04:58	M1.7	S16E35	6.0°	3166 ± 66	661 ± 214	0.153	484 ± 86	283 ± 85	96 ± 10	0.55
219	2012-07-10 06:05	M2.0	S16E30	5.5°	3523 ± 57	778 ± 115	0.238	839 ± 163	461 ± 109	96 ± 4	0.70
220	2012-07-12 15:37	X1.4	S15W03	4.8°	3915 ± 766	951 ± 324	0.357	1399 ± 89	721 ± 222	103 ± 3	1.88
221	2012-07-14 04:51	M1.0	S20W23	5.7°	3485 ± 106	863 ± 275	0.240	835 ± 141	324 ± 80	91 ± 4	0.23
227	2012-07-30 15:39	M1.1	S21E28	3.8°	1358 ± 42	87 ± 33	0.076	102 ± 5	52 ± 7	40 ± 2	0.23
228	2012-08-06 04:33	M1.6	N16W12	5.5°	396 ± 10	3 ± 1	0.033	12 ± 2	6 ± 1	27 ± 3	0.13
229	2012-08-11 11:55	M1.0	S25W41	3.7°	142 ± 4	7 ± 2	0.115	16 ± 0	10 ± 1	22 ± 0	1.03
239	2012-09-08 17:35	M1.4	S14W40	4.4°	1004 ± 28	66 ± 19	0.153	154 ± 38	56 ± 12	28 ± 2	0.75
253	2012-11-13 05:42	M2.5	S26E44	4.0°	275 ± 19	65 ± 23	0.397	109 ± 11	47 ± 4	27 ± 1	0.20
254	2012-11-13 20:50	M2.8	S23E31	4.1°	275 ± 88	25 ± 10	0.128	35 ± 3	17 ± 2	21 ± 2	0.12
255	2012-11-14 03:59	M1.1	S23E27	3.7°	308 ± 13	30 ± 6	0.137	42 ± 5	17 ± 3	23 ± 1	0.13
256	2012-11-20 12:36	M1.7	N10E22	4.2°	534 ± 13	6 ± 3	0.040	21 ± 3	11 ± 2	26 ± 2	0.17
257	2012-11-20 19:21	M1.6	N10E19	3.8°	680 ± 23	12 ± 5	0.047	31 ± 4	17 ± 4	24 ± 0	0.18
258	2012-11-21 06:45	M1.4	N10E12	3.9°	806 ± 233	34 ± 14	0.072	58 ± 4	37 ± 10	28 ± 1	0.38
259	2012-11-21 15:10	M3.5	N10E08	3.4°	1075 ± 23	48 ± 12	0.072	77 ± 7	50 ± 17	35 ± 2	0.47
261	2012-11-27 21:05	M1.0	S13W42	3.9°	788 ± 17	18 ± 11	0.054	42 ± 9	15 ± 3	27 ± 3	0.42
264	2013-01-11 08:43	M1.2	N05E42	3.7°	1804 ± 66	62 ± 23	0.114	206 ± 30	119 ± 27	37 ± 1	0.57
265	2013-01-11 14:51	M1.0	N06E42	3.0°	1970 ± 51	47 ± 24	0.037	73 ± 7	32 ± 5	32 ± 4	0.55
266	2013-01-13 00:45	M1.0	N18W15	4.6°	811 ± 16	25 ± 14	0.024	19 ± 2	15 ± 6	37 ± 6	0.12
267	2013-01-13 08:35	M1.7	N17W18	3.9°	834 ± 7	43 ± 18	0.059	49 ± 11	37 ± 10	29 ± 1	0.08
268	2013-02-17 15:45	M1.9	N12E23	4.2°	219 ± 4	3 ± 2	0.083	18 ± 2	7 ± 1	19 ± 1	0.12
273	2013-04-11 06:55	M6.5	N11E13	5.2°	805 ± 15	18 ± 15	0.062	50 ± 4	29 ± 6	34 ± 4	0.57
275	2013-04-22 10:22	M1.0	N13W27	3.5°	1197 ± 47	104 ± 45	0.223	267 ± 14	157 ± 7	36 ± 2	0.15
276	2013-05-02 04:58	M1.1	N10W19	5.4°	1115 ± 21	27 ± 21	0.056	62 ± 15	38 ± 21	36 ± 1	0.35
277	2013-05-03 16:39	M1.3	N11W38	4.7°	548 ± 16	21 ± 7	0.027	14 ± 4	15 ± 5	30 ± 3	0.72
289	2013-05-16 21:36	M1.3	N11E40	4.2°	391 ± 15	13 ± 6	0.056	22 ± 2	10 ± 2	27 ± 3	0.45

Table 3—Continued

#	Flare start time	GOES class	Helio- position graphic	Mis- align angle (deg)	Potential energy E_p (10^{30} erg)	Free energy E_{free} (10^{30} erg)	Energy ratio E_{free}/E_p	Dissipated energy E_{diss} (10^{30} erg)	Peak dissipation rate P_{diss} (10^{30} erg /0.2 hr)	Length scale L (Mm)	Duration T (hrs)
290	2013-05-17 08:43	M3.2	N11E36	4.6°	389 ± 9	12 ± 8	0.041	16 ± 2	17 ± 7	24 ± 3	0.60
293	2013-05-31 19:52	M1.0	N12E42	4.1°	85 ± 3	1 ± 0	0.018	1 ± 0	1 ± 0	15 ± 1	0.23
299	2013-08-12 10:21	M1.5	S21E17	5.1°	388 ± 9	15 ± 6	0.043	16 ± 0	13 ± 1	22 ± 3	0.43
300	2013-08-17 18:16	M3.3	S04W30	5.2°	595 ± 23	97 ± 52	0.120	71 ± 5	35 ± 5	33 ± 1	0.32
301	2013-08-17 18:49	M1.4	S04W30	4.6°	600 ± 28	124 ± 47	0.360	216 ± 35	124 ± 19	53 ± 3	1.08
304	2013-10-13 00:12	M1.7	S22E17	4.9°	501 ± 10	31 ± 11	0.162	81 ± 10	39 ± 10	23 ± 4	0.88
305	2013-10-15 08:26	M1.8	S21W14	4.7°	353 ± 8	10 ± 3	0.068	24 ± 1	15 ± 4	18 ± 3	0.37
306	2013-10-15 23:31	M1.3	S21W22	4.7°	294 ± 5	16 ± 4	0.134	39 ± 10	14 ± 6	22 ± 2	0.17
308	2013-10-22 00:14	M1.0	N08E20	3.4°	1226 ± 20	43 ± 24	0.121	148 ± 10	78 ± 7	34 ± 5	0.23
309	2013-10-22 14:49	M1.0	N08E11	3.5°	1959 ± 47	43 ± 17	0.059	115 ± 21	61 ± 16	28 ± 4	0.65
310	2013-10-22 21:15	M4.2	N07E03	3.5°	2090 ± 44	7 ± 4	0.013	26 ± 2	14 ± 3	37 ± 3	0.12
311	2013-10-23 20:41	M2.7	N08W06	3.5°	3015 ± 64	231 ± 57	0.055	166 ± 21	79 ± 15	43 ± 1	0.30
312	2013-10-23 23:33	M1.4	N09W08	4.2°	2392 ± 788	216 ± 105	0.147	350 ± 19	294 ± 27	71 ± 3	0.23
313	2013-10-23 23:58	M3.1	N09W09	3.8°	2923 ± 43	254 ± 87	0.051	149 ± 7	130 ± 37	45 ± 3	0.30
314	2013-10-24 00:21	M9.3	S09E12	4.2°	1468 ± 42	81 ± 40	0.163	239 ± 24	125 ± 26	86 ± 3	0.23
315	2013-10-24 09:59	M2.5	N09W14	3.6°	2812 ± 35	230 ± 55	0.077	217 ± 12	156 ± 34	46 ± 3	0.30
316	2013-10-24 10:30	M3.5	N09W14	3.7°	2848 ± 48	311 ± 77	0.053	150 ± 40	115 ± 47	49 ± 9	0.12
334	2013-10-28 14:46	M2.7	S08E27	4.8°	682 ± 24	16 ± 11	0.076	52 ± 11	42 ± 5	31 ± 3	0.30
335	2013-10-28 15:07	M4.4	S06E28	4.2°	697 ± 18	37 ± 19	0.144	100 ± 3	53 ± 10	34 ± 2	0.23
339	2013-11-01 19:46	M6.3	S12E01	3.7°	1523 ± 23	34 ± 12	0.054	82 ± 7	47 ± 10	29 ± 0	0.20
340	2013-11-02 22:13	M1.6	S12W12	4.6°	1060 ± 27	40 ± 21	0.082	87 ± 3	40 ± 5	29 ± 1	0.20
341	2013-11-03 05:16	M5.0	S10W17	4.2°	968 ± 22	14 ± 7	0.090	87 ± 8	42 ± 13	32 ± 2	0.17
344	2013-11-05 22:07	X3.3	S08E44	3.8°	2066 ± 65	72 ± 30	0.132	273 ± 66	141 ± 41	50 ± 5	0.13
345	2013-11-06 13:39	M3.8	S09E35	3.9°	2256 ± 60	71 ± 22	0.080	180 ± 5	67 ± 10	40 ± 3	0.23
347	2013-11-07 03:34	M2.3	S08E26	4.6°	2812 ± 36	119 ± 58	0.132	370 ± 63	167 ± 19	47 ± 4	0.15
348	2013-11-07 14:15	M2.4	S08E18	4.0°	2915 ± 49	98 ± 58	0.097	283 ± 23	117 ± 36	48 ± 3	0.27
349	2013-11-08 04:20	X1.1	S11E11	4.5°	3290 ± 56	187 ± 58	0.077	252 ± 29	186 ± 31	41 ± 2	0.15
350	2013-11-08 09:22	M2.3	S17W29	4.2°	236 ± 9	8 ± 2	0.102	24 ± 2	8 ± 1	23 ± 3	0.15
351	2013-11-10 05:08	X1.1	S13W13	4.2°	2010 ± 22	109 ± 49	0.127	254 ± 51	154 ± 31	46 ± 4	0.17
355	2013-11-16 04:47	M1.2	S14W29	3.7°	767 ± 36	65 ± 61	0.054	41 ± 12	26 ± 14	26 ± 2	0.17
356	2013-11-16 07:45	M1.6	S17W30	3.7°	806 ± 36	54 ± 30	0.062	49 ± 8	55 ± 18	29 ± 1	0.13
357	2013-11-17 05:06	M1.0	S19W41	3.6°	680 ± 34	135 ± 28	0.180	122 ± 16	70 ± 20	44 ± 1	0.12
367	2013-12-22 14:24	M1.6	S16E44	4.5°	553 ± 10	49 ± 19	0.118	65 ± 6	35 ± 9	23 ± 4	0.40
372	2013-12-29 07:49	M3.1	S16E03	3.3°	936 ± 12	18 ± 8	0.042	39 ± 5	22 ± 6	24 ± 2	0.18
373	2013-12-31 21:45	M6.4	S19W36	4.2°	848 ± 29	29 ± 25	0.194	164 ± 18	105 ± 14	36 ± 0	0.58
374	2014-01-01 18:40	M9.9	S19W45	5.1°	624 ± 11	41 ± 16	0.191	119 ± 25	59 ± 16	31 ± 2	0.38
380	2014-01-04 18:47	M4.0	S15E30	4.5°	3436 ± 109	737 ± 170	0.328	1125 ± 224	465 ± 126	101 ± 7	1.60
382	2014-01-07 03:49	M1.0	N07E07	2.5°	835 ± 18	61 ± 16	0.089	74 ± 7	23 ± 4	21 ± 1	0.12
383	2014-01-07 10:07	M7.2	S13E13	4.4°	3872 ± 48	443 ± 137	0.137	529 ± 61	263 ± 70	73 ± 3	0.50
384	2014-01-07 18:04	X1.2	S12E08	4.3°	3949 ± 67	478 ± 148	0.074	292 ± 74	184 ± 59	60 ± 3	0.90
399	2014-01-31 15:32	M1.1	N07E34	3.4°	717 ± 20	27 ± 11	0.128	91 ± 9	32 ± 6	31 ± 4	0.35

Table 4. Comparison of magnetic energies calculated with the COR-NLFFF and PHOT-NLFFF code for 11 M and X-class flares with a longitude difference of $< 45^\circ$ to the central meridian.

#	GOES class	Potential energy E_p^{COR}	Potential energy ratio E_p^{PHOT}/E_p^{COR}	Free energy E_{free}^{COR}	Free energy ratio $E_{free}^{PHOT}/E_{free}^{COR}$	Dissipated energy E_{diss}^{COR}	Dissipated energy ratio $E_{diss}^{PHOT}/E_{diss}^{COR}$
12	X2.2	1065 ± 15	0.94	52 ± 21	5.16	120 ± 11	0.88
37	X1.5	1791 ± 24	0.91	150 ± 38	1.21	269 ± 27	0.28
66	X2.1	922 ± 24	0.64	50 ± 35	3.22	188 ± 10	0.37
67	X1.8	582 ± 17	1.04	89 ± 17	0.85	94 ± 8	1.10
147	X5.4	1741 ± 32	1.22	198 ± 66	5.61	275 ± 47	1.27
148	X5.4	1781 ± 35	1.19	168 ± 56	6.64	200 ± 10
220	X1.4	3916 ± 766	1.01	951 ± 324	1.12	1399 ± 89	0.09
344	X3.3	2067 ± 65	1.61	72 ± 31	6.64	273 ± 67	0.32
349	X1.1	3290 ± 57	0.62	188 ± 58	1.37	253 ± 29	0.29
351	X1.1	2011 ± 23	0.85	109 ± 49	2.25	255 ± 52	0.22
384	X1.2	3950 ± 68	1.57	479 ± 149	1.83	293 ± 75	0.56
Average			1.05 ± 0.33		3.3 ± 2.3		0.5 ± 0.4

20110215_011400, EVENT=12, FRAME= 0 / 13, RUN=run2

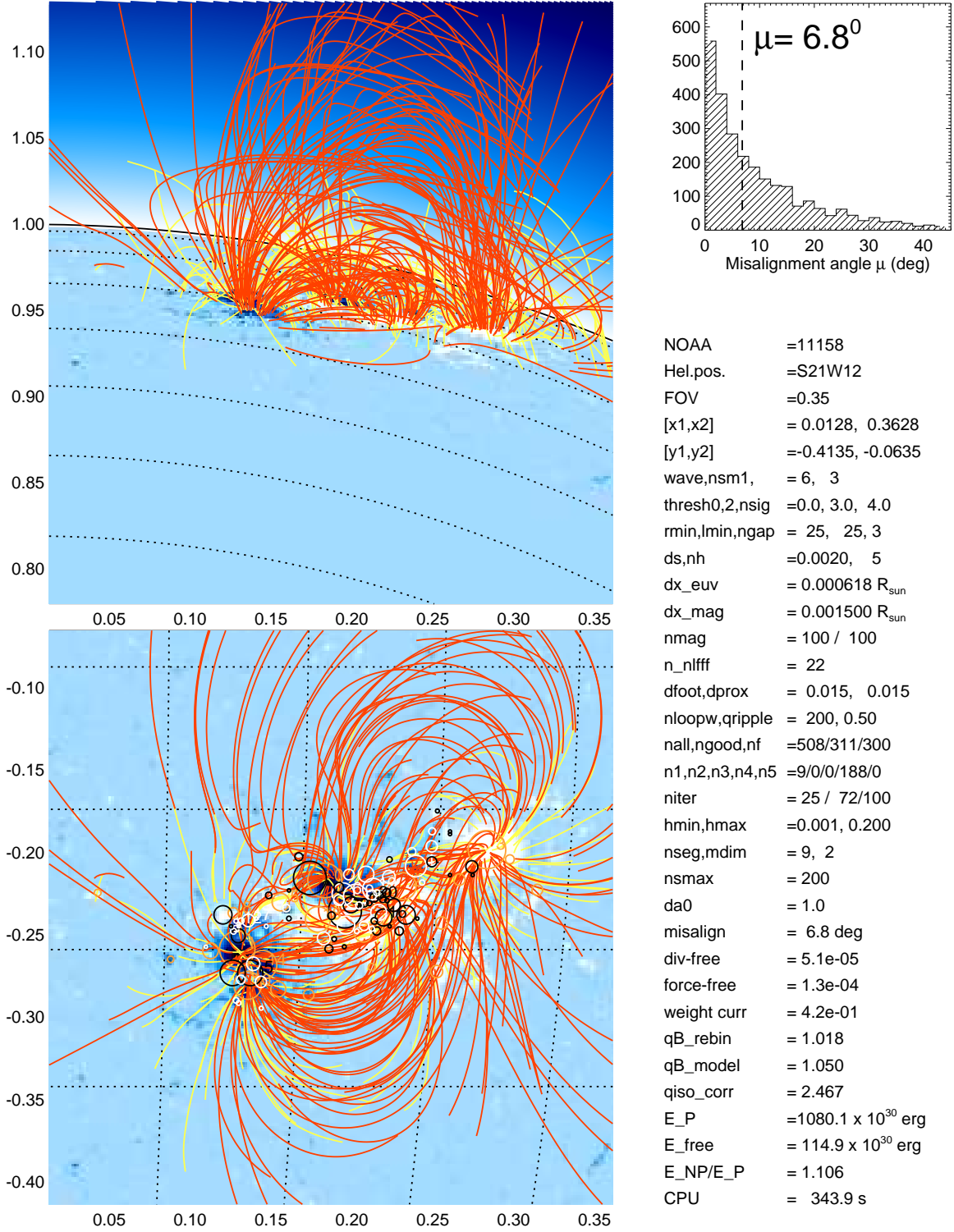


Fig. 1.— Example of a forward-fitting run (RUN2) for flare event #12 (2011 February 15, 01:14 UT), for time frame $i_t = 0$ (out of $n_t = 13$ flare time intervals). RUN2 selects loop structures with a ripple ratio of $q_{ripple} \leq 0.5$ in a field-of-view of $FOV = 0.35$ solar radii. The magnetogram (blue) and observed loops (yellow curves) and best-fit magnetic field lines (red) are shown in the image plane (x, y) (bottom panel) and rotated by 90° to the north (top panel), which corresponds to a projection into the (x, z) plane. The magnetic charges are indicated with (white/black) circles according to their (positive/negative) magnetic polarity and depth (radius or circles). The distribution of 2D misalignment angles is shown in a histogram

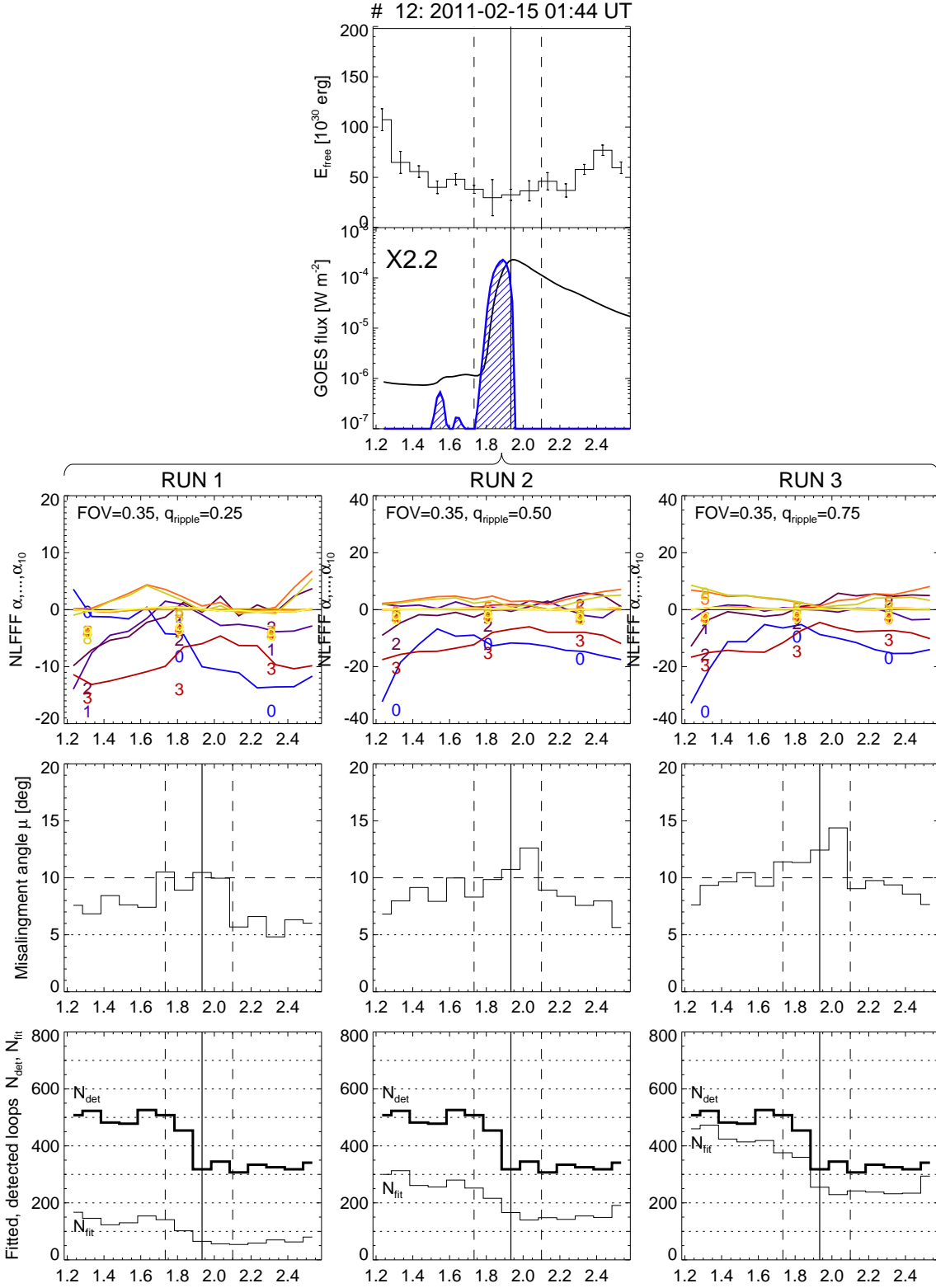


Fig. 2.— The time evolution of the free energy $E_{free}(t)$ (top middle), the GOES flux $F_{GOES}(t)$ (second row from top, black curve) and its time derivative (second row; blue hatched curve), averaged from three runs with different loop selection parameters (3 columns: $q_{ripple} = 0.25$ (RUN1, left), $q_{ripple} = 0.50$ (RUN2, middle), $q_{ripple} = 0.75$ (RUN3, right), yielding error bars for the free energy measurements. The time evolution of the force-free parameter $\alpha(t)$ for the 10 strongest magnetic sources (third row), the median misalignment angle $\mu_2(t)$ (fourth row), the number of detected $N_{det}(t)$ (bottom row; thick linestyle) and number of fitted loops $N_{fit}(t)$ (bottom row; thin linestyle), are shown for each of the 3 runs separately. The vertical lines indicate the flare peak time (solid linestyle), the flare start and end times (dashed linestyle).

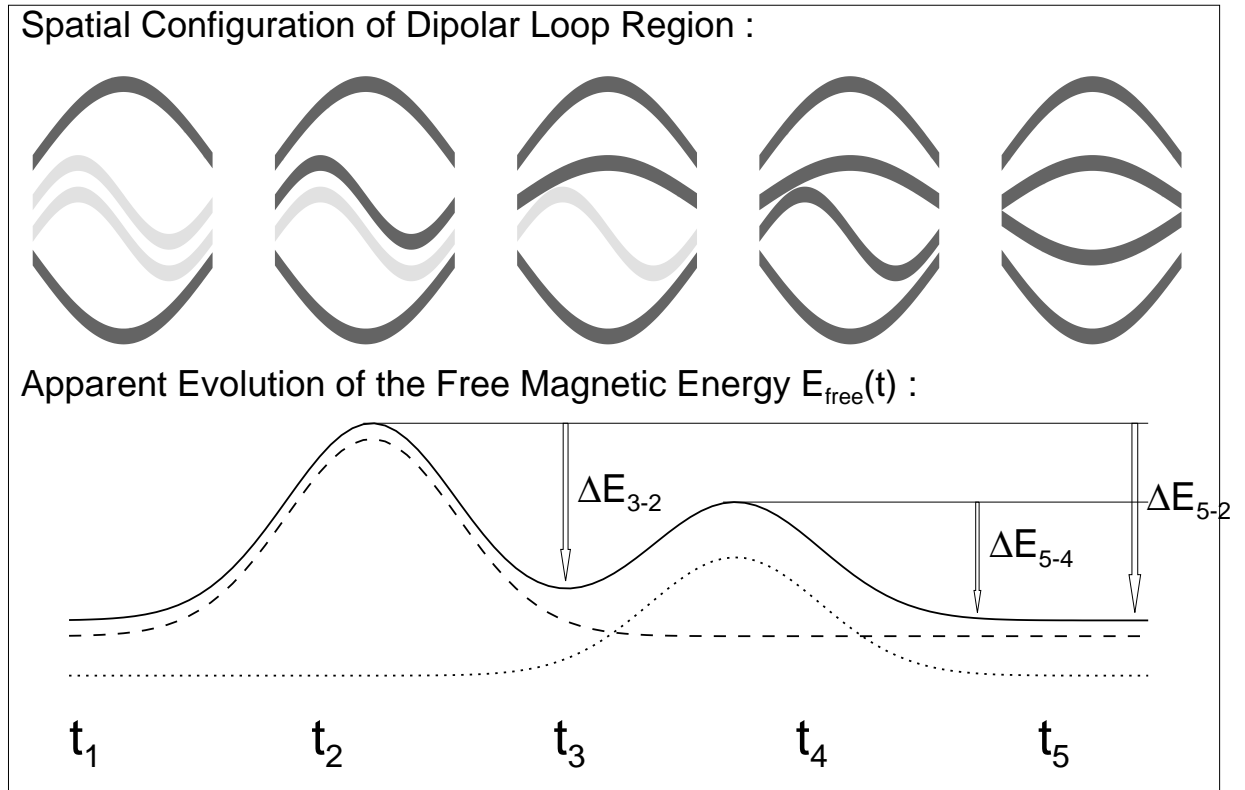


Fig. 3.— Schematic diagram of the spatial loop configuration (top panel) and evolution of free magnetic energy $E_{free}(t)$ during a flare. Mostly potential loops are visible at the beginning of a flare (t_1), while a first sigmoid is illuminated at t_2 , which relaxes to a potential loop at time t_3 . A second sigmoid is illuminated at time t_4 , which relaxes to a potential loop at time t_5 . The total energy difference before and after the flare, ΔE_{5-2} , is a lower limit to the sum of all sequential energy releases ΔE_{3-2} and ΔE_{5-4} , and thus underestimates the total dissipated magnetic energy (Aschwanden, Sun, & Liu 2014).

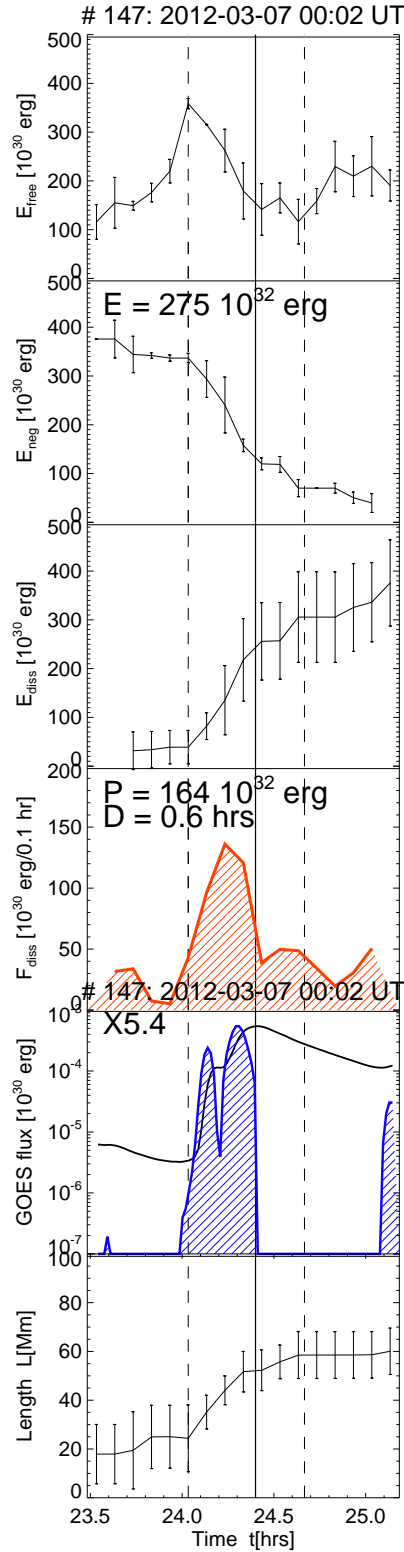


Fig. 4.— An example of the evolutionary parameters as defined in text is given here for the event # 147, 2012-Mar-07 00:02 UT, an X5.4 GOES class flare: the free energy $E_{free}(t) = E_n(t) - E_p(t)$ (top panel), the cumulative negative energy $E_{neg}(t)$ (second panel), the dissipated energy $E_{diss}(t)$ (third panel), the energy dissipation rate $F_{diss} = dE_{diss}(t)/dt$ (fourth panel; red), the GOES flux F_{GOES} and its time derivative $dF_{GOES}(t)/dt$ (fifth panel; blue), and the length scale $L(t)$ of the cumulative flare area (bottom panel). The

Preflare Energy Dissipation

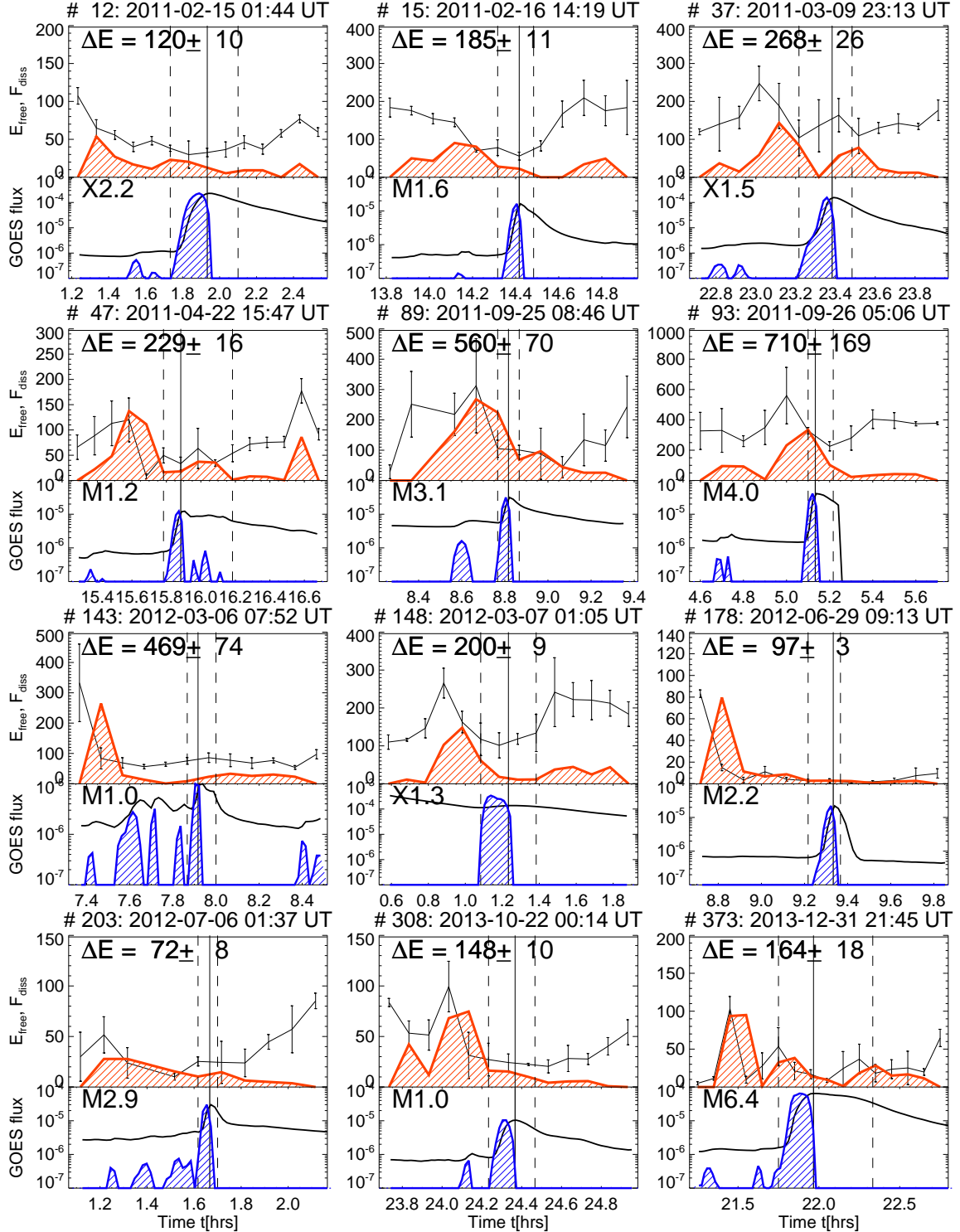


Fig. 5.— Examples of 12 flares with magnetic energy dissipation starting in the preflare phase. Each of the 12 panels shows the time evolution of the free (magnetic) energy $E_{free}(t)$ in units of 10^{30} erg (black curve with error bars), the energy dissipation rate $F_{diss}(t)$ in units of $[10^{30} \text{ erg} / 0.2 \text{ hr}]$ (red curve with hatched area), the GOES 1-8 Å light curve in units of W cm^{-2} (solid black curves), and its time derivative (blue curve with hatched area).

Flare Rise Time Energy Dissipation

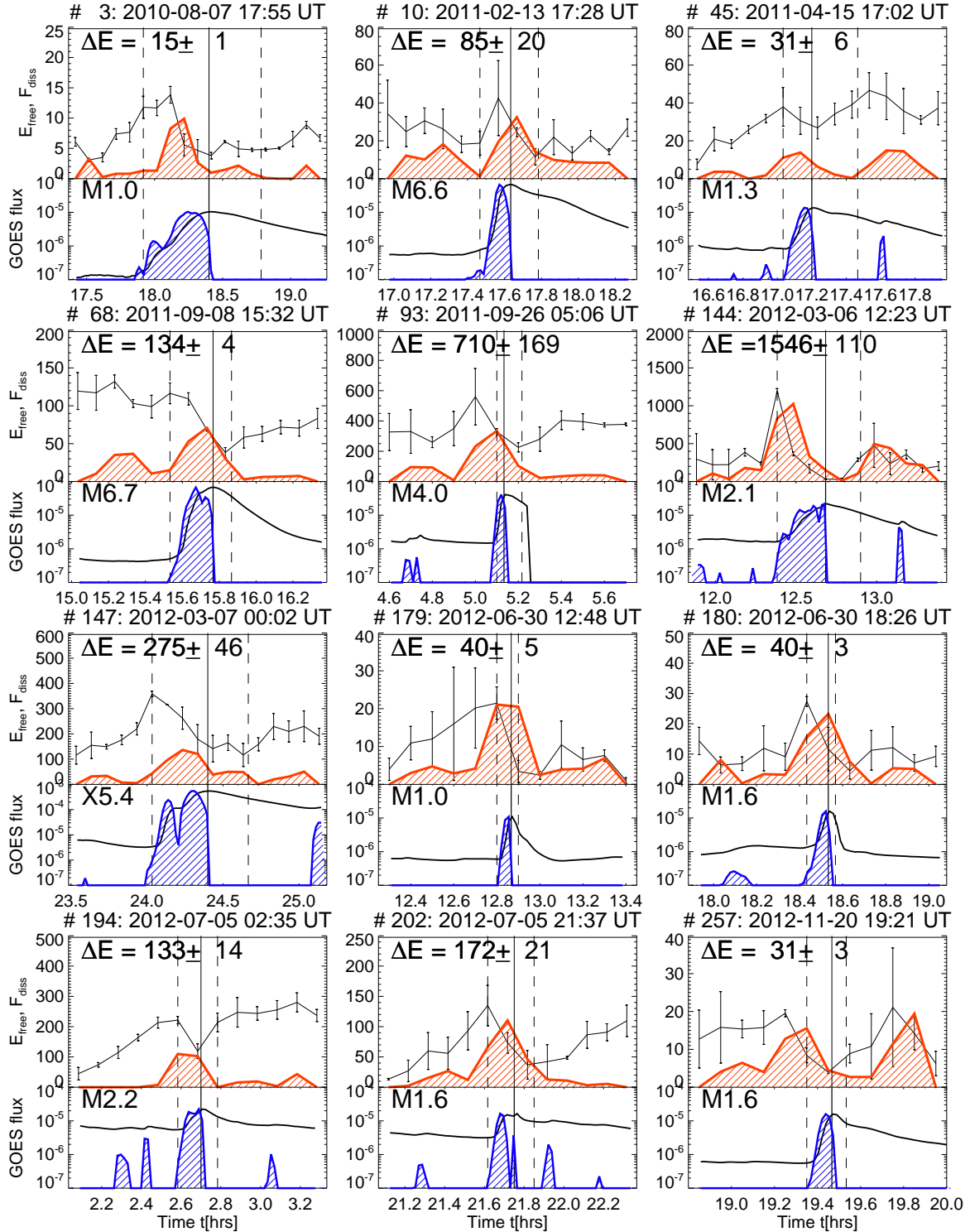


Fig. 6.— Examples of magnetic energy dissipation coinciding with the flare rise time. Representation otherwise similar to Fig. 5.

Flare Decay Time Energy Dissipation

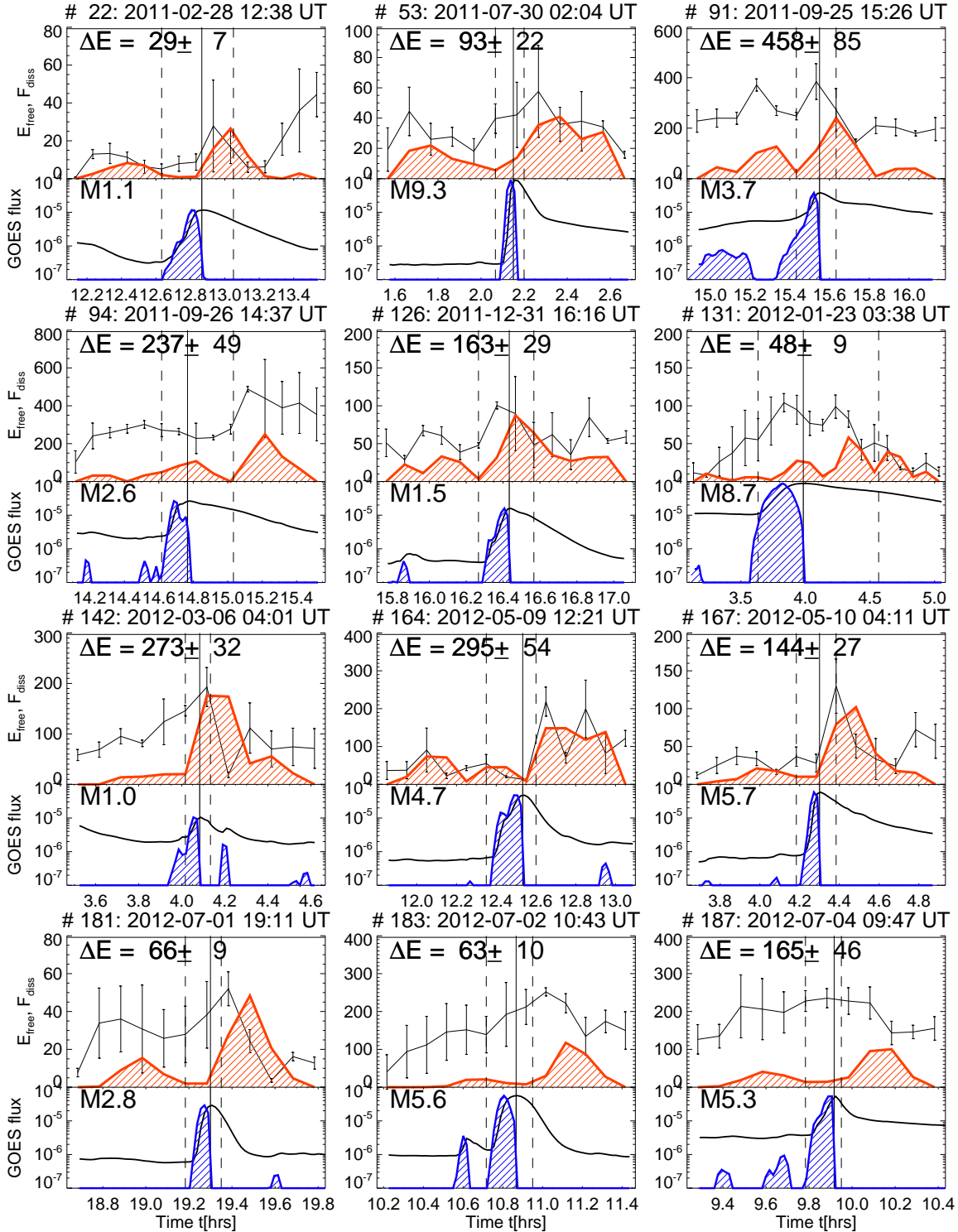


Fig. 7.— Examples of events with magnetic energy dissipation occurring mostly during the flare decay phase. Representation otherwise similar to Fig. 5.

Double Flare Two-Step Energy Dissipation

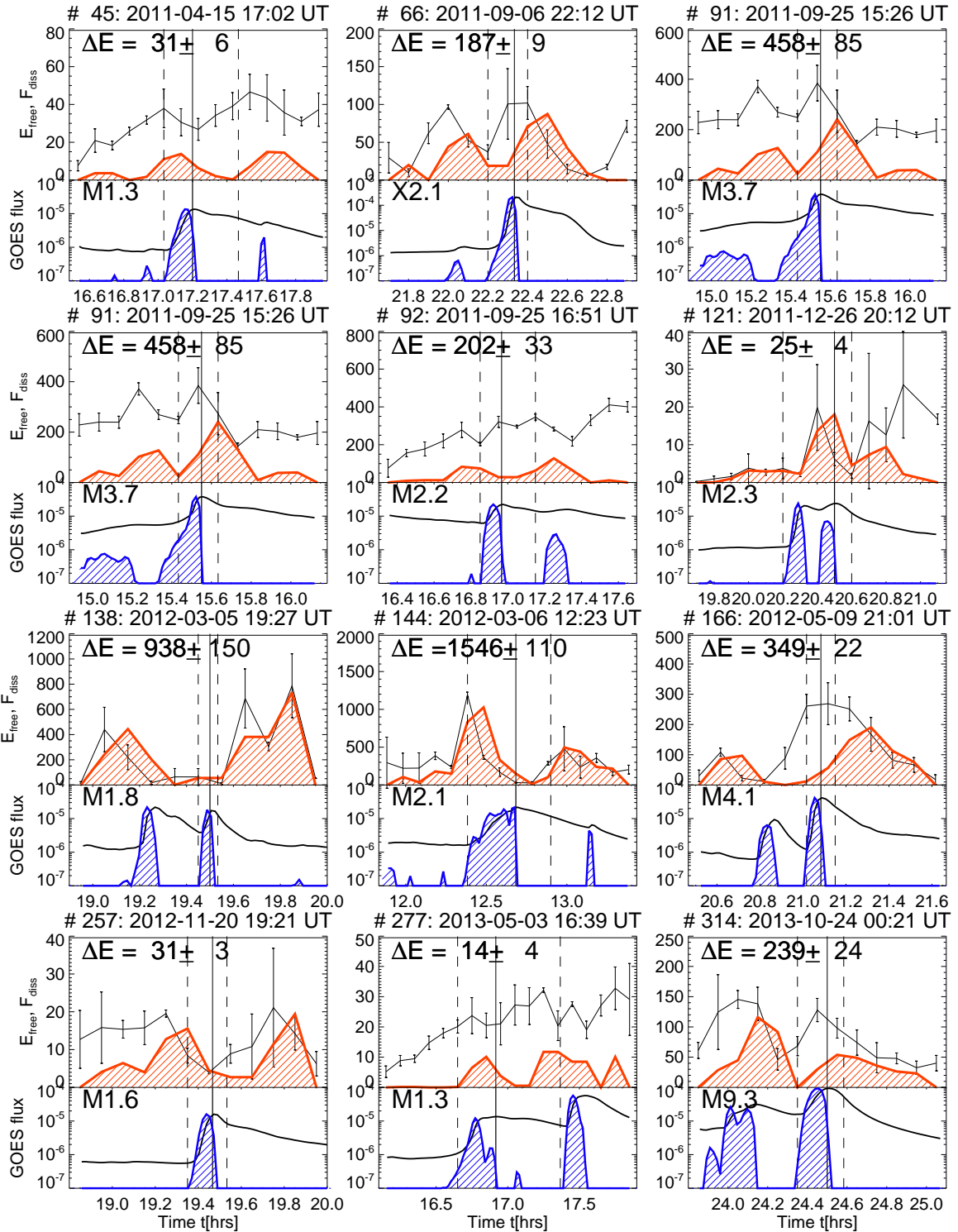


Fig. 8.— Examples of dual flare events with magnetic energy dissipation associated with the two flare peaks. Representation otherwise similar to Fig. 5.

Complex Flare Multi-Step Energy Dissipation

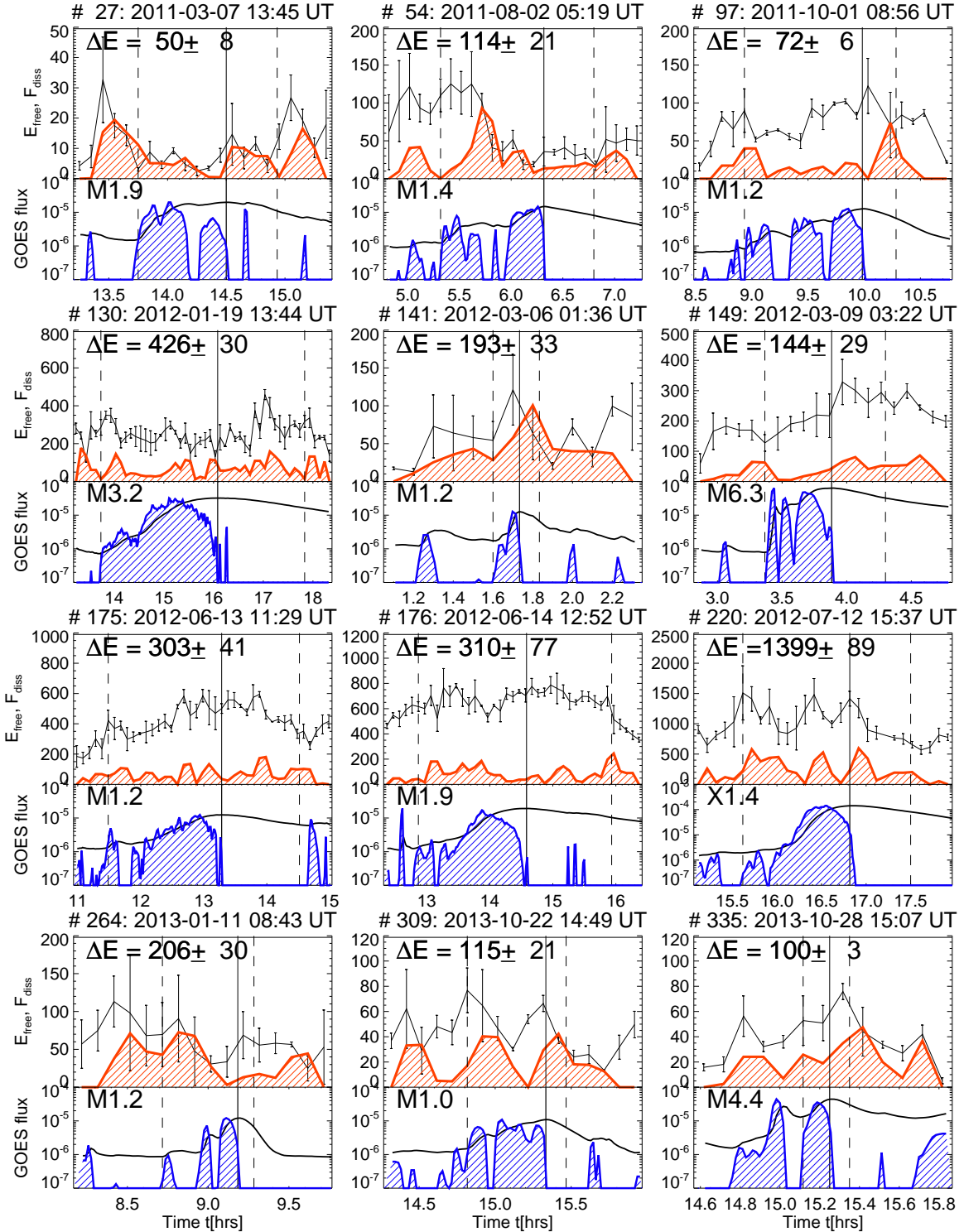


Fig. 9.— Examples of complex flare events with multi-step magnetic energy dissipation associated with individual flare subpeaks. Representation otherwise similar to Fig. 5.

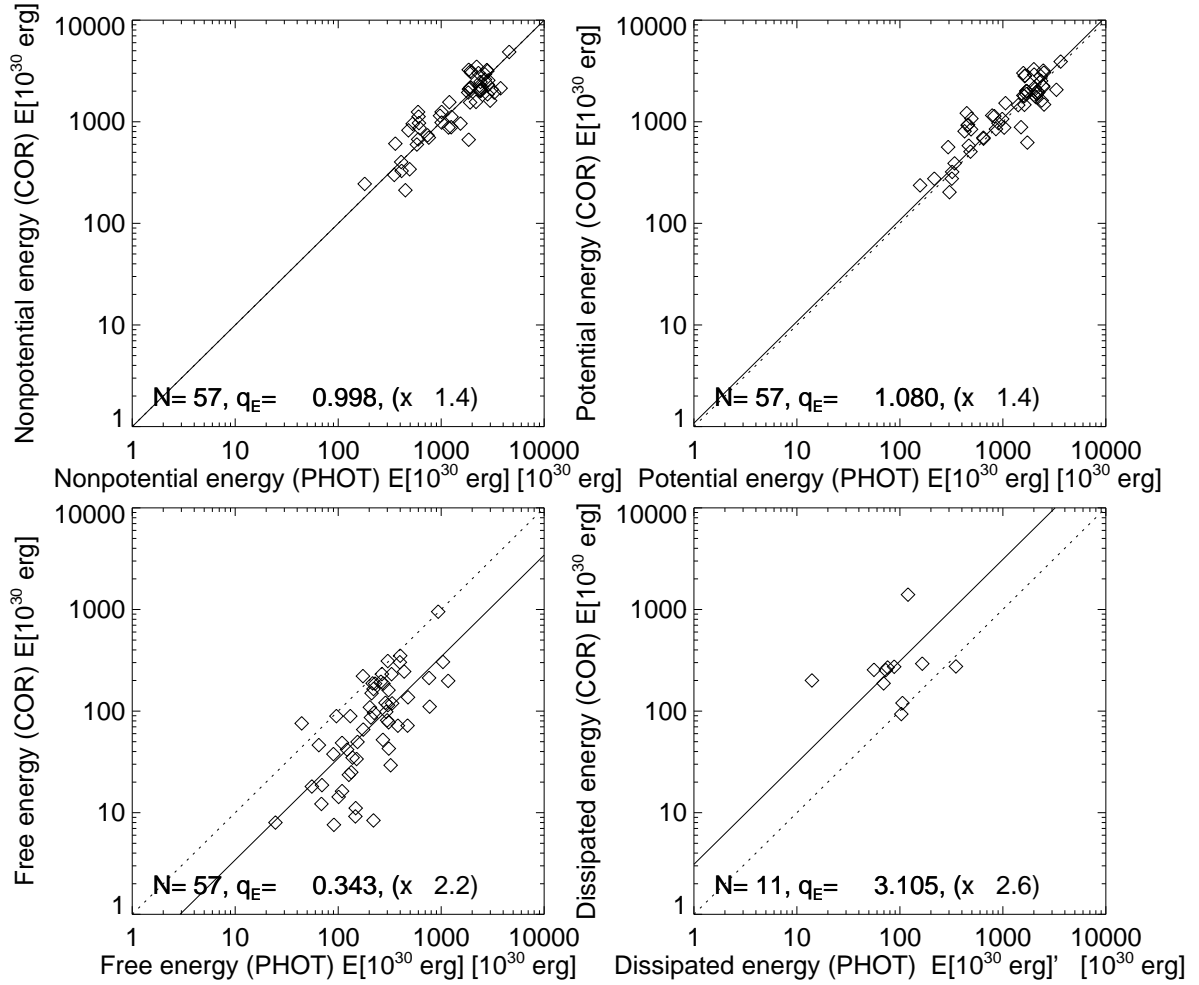


Fig. 10.— Scatterplot of mean nonpotential energies (top left), potential energies (top right), free energies (bottom left), and dissipated energies (bottom right) between the PHOT-NLFFF (x-axis) and COR-NLFFF codes (y-axis). The solid line indicates the mean proportionality ratio, and the dotted line the unity ratio.

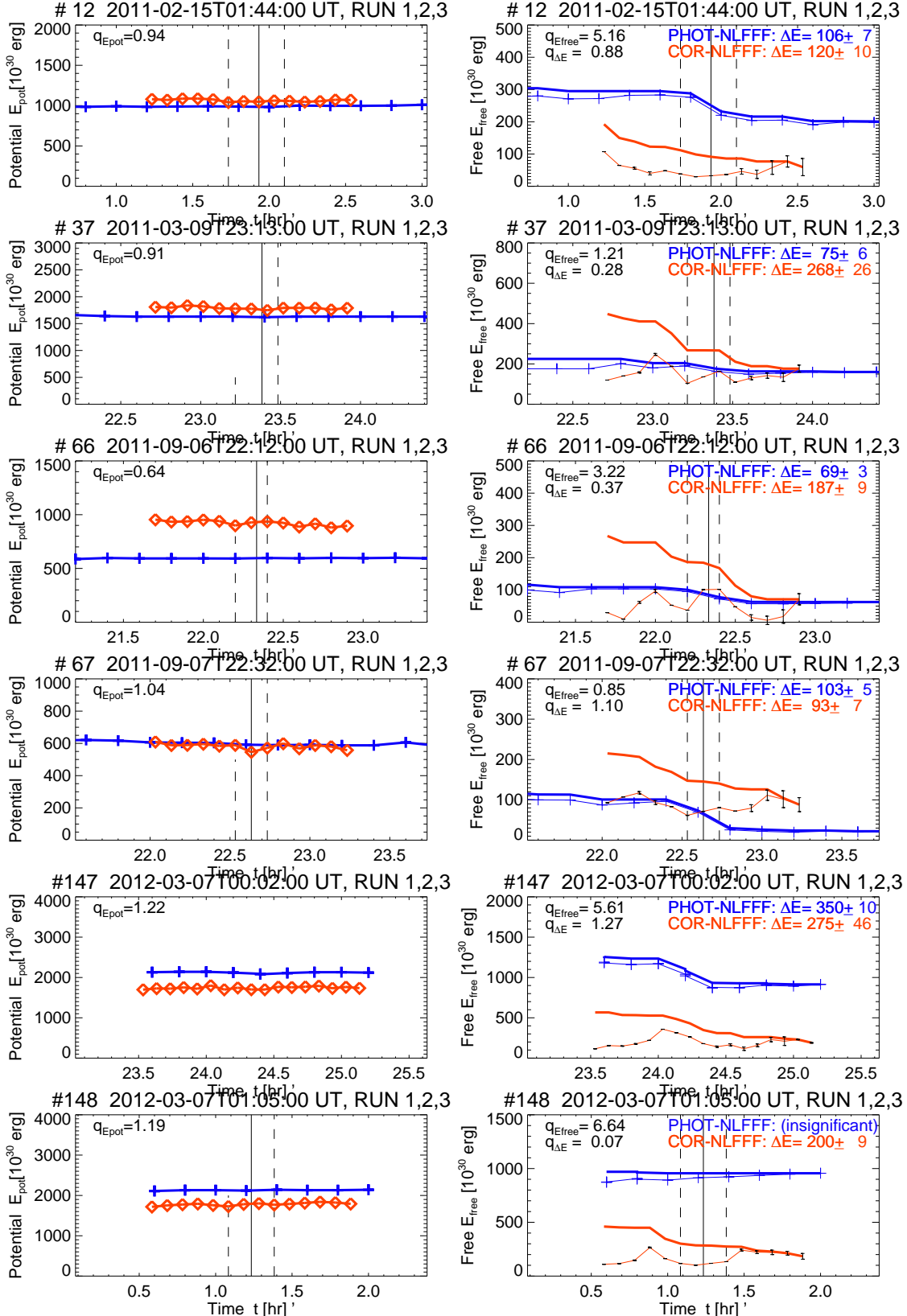


Fig. 11.— Comparison of the evolution of the potential energy $E_p(t)$ (left panels), the free energy $E_{free}(t) = E_{np}(t) - E_p(t)$ (right panels, thin curves), and the cumulative negative energy decreases $F_{neg}(t)$ (right panels, thick curves), for both the coronal COR-NLFFF code (red curves) and the photospheric PHOT-NLFFF code (blue curves), for six X-class flares.

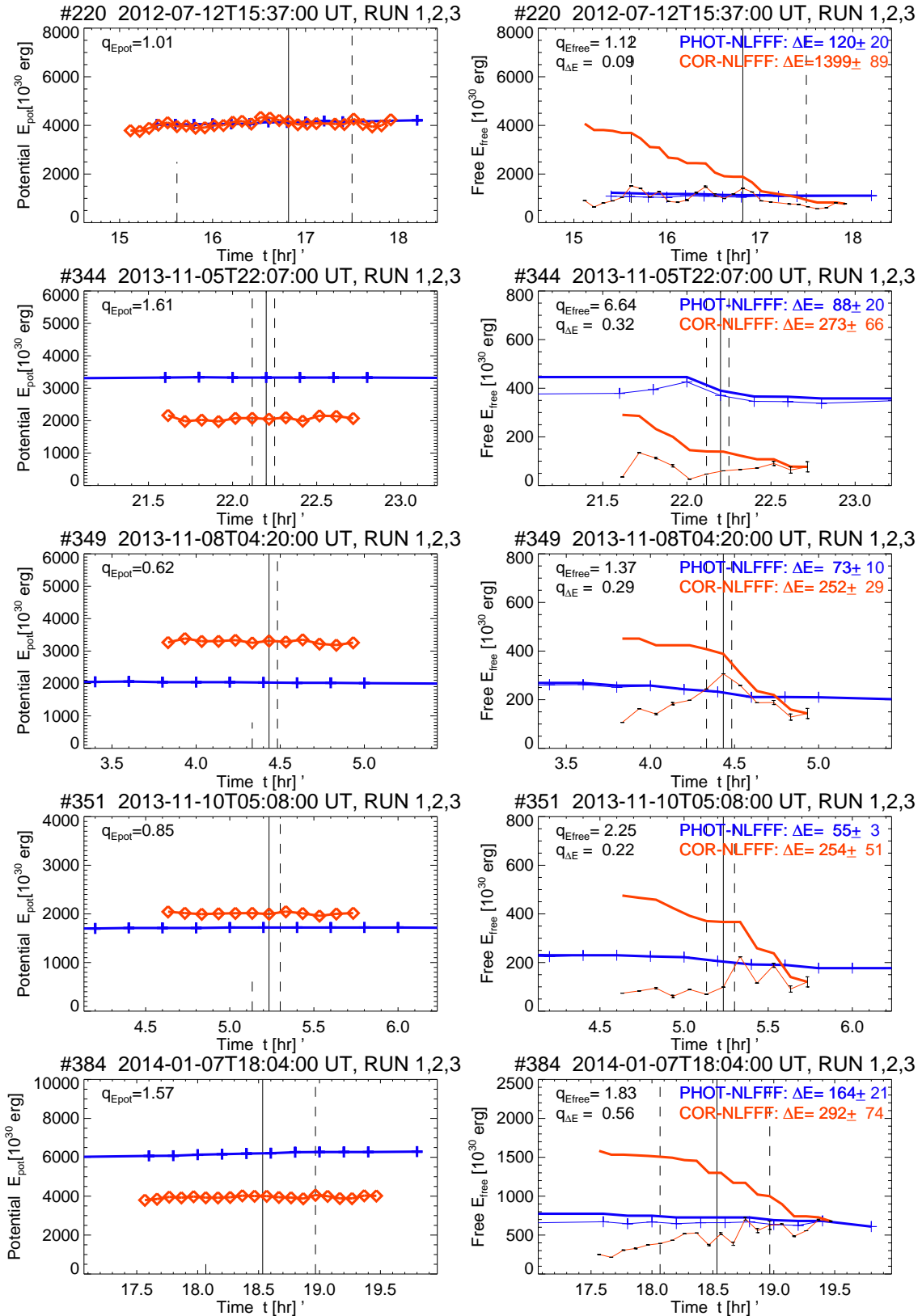


Fig. 12.— Comparison of energy evolution for another five X-class flares, with similar representation as in Fig. 11.

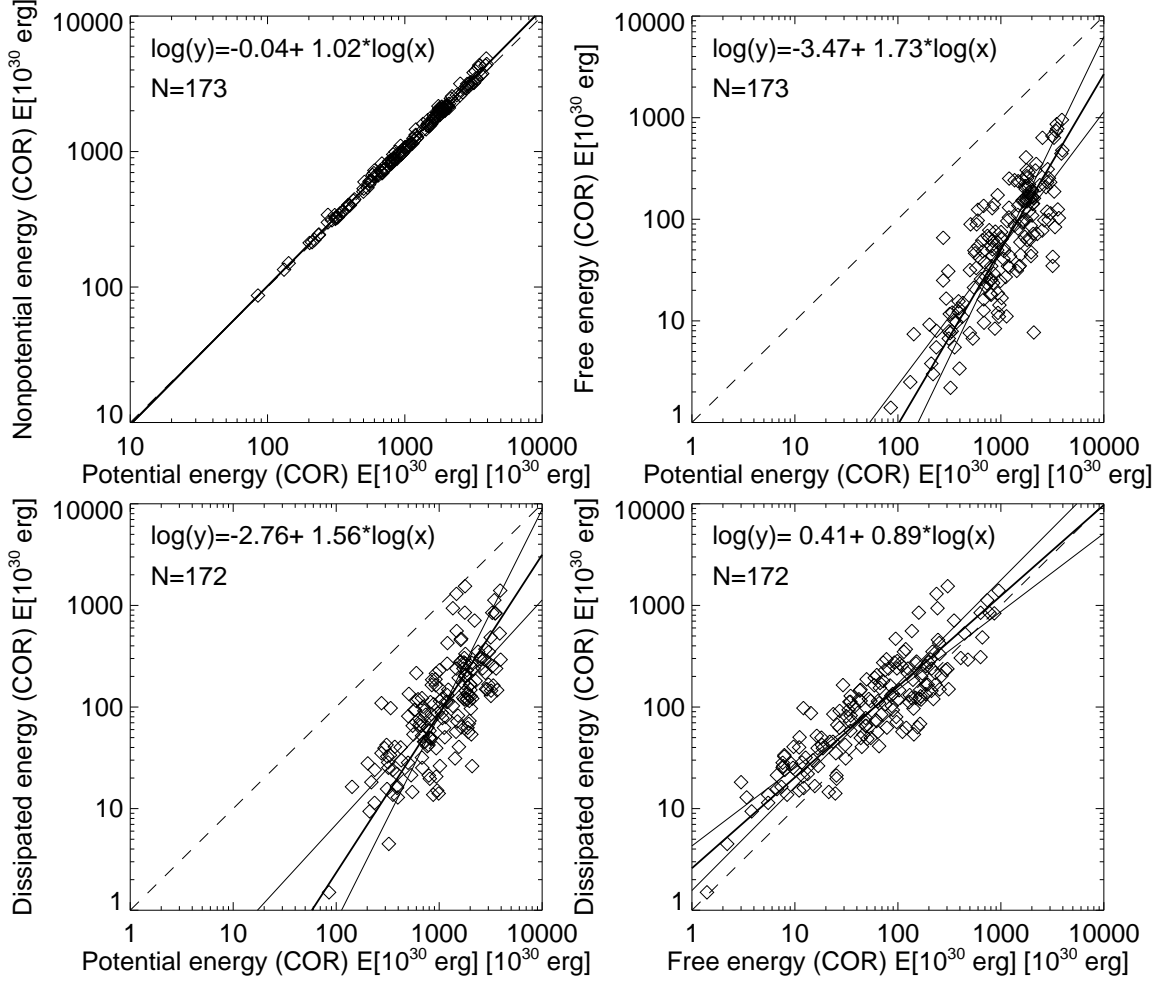


Fig. 13.— Scaling laws between the nonpotential energy E_{np} , the potential energy E_p , the free energy E_{free} , and the dissipated energy E_{diss} , for energy values computed with the COR-NLFFF code. Linear regression fits (thick solid lines) and uncertainties (thin lines) are shown, while proportionality is indicated with a dashed line.

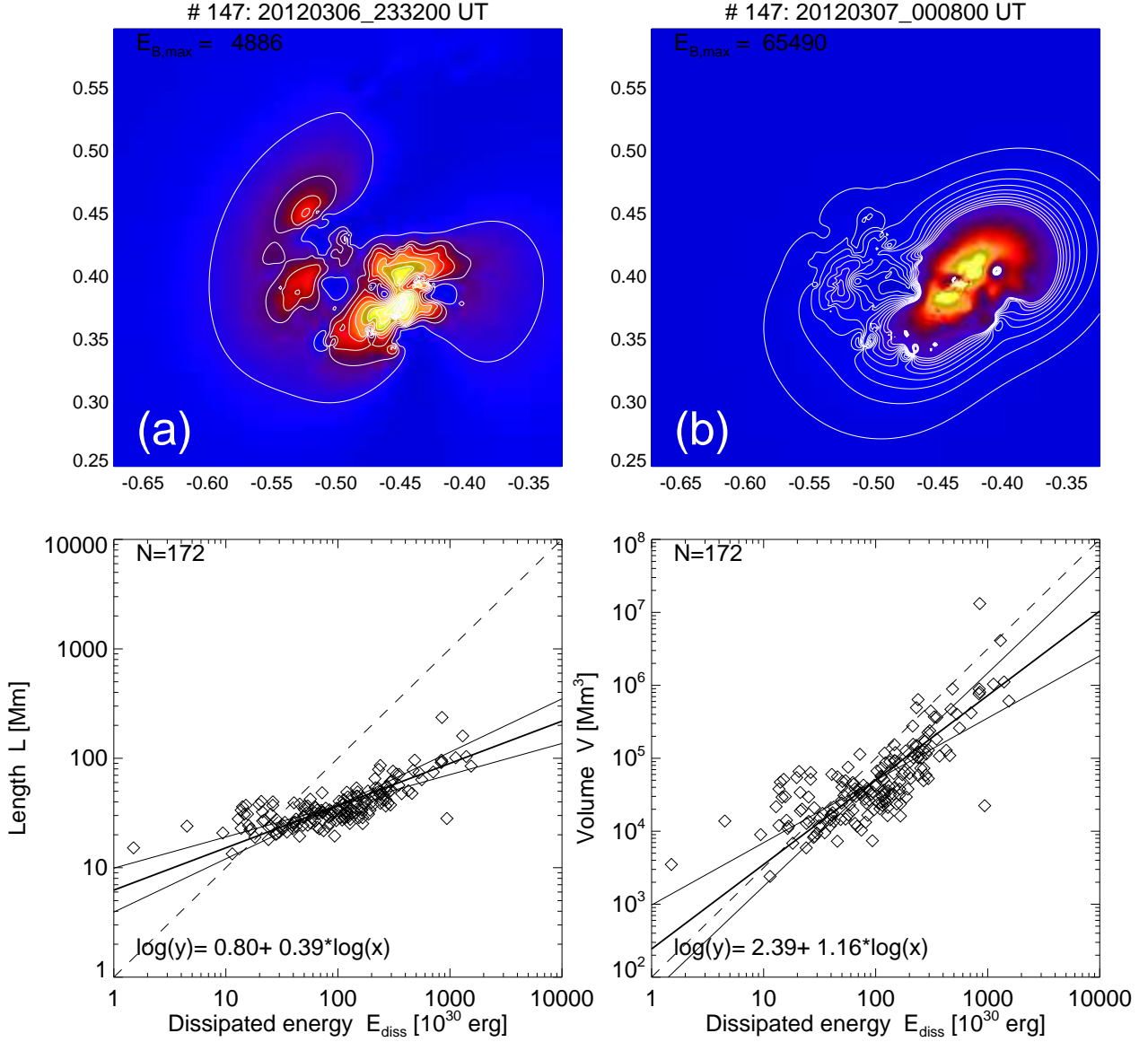


Fig. 14.— (a) Contour plot of the free energy distribution $E_{free}(x, y) = E_{np}(x, y) - E_p(x, y) = B_\varphi(x, y)^2 / (8\pi)$, in contours of $B_i = 5, 10, \dots, 100$ G, before the flare (2011-Mar-06 23:32 UT), and (b) at the peak of the flare. Note the maximum of the dissipated energy distribution is a factor of 13 higher at the flare peak. The flare area A is measured from the number of pixels above some energy threshold, defining a length scale $L = A^{1/2}$ and a flare volume $V = A^{3/2}$. *Bottom row*: Correlation plots of the dissipated flare energy E_{diss} and the flare length scale L (bottom left panel) or the flare volume $V = L^3$ (bottom right panel) for all analyzed 172 flare events. Linear regression fits (thick solid lines), uncertainties (thin solid lines), and proportionality (dashed line) are indicated, Note that the flare volume V is almost proportional to the dissipated energies E_{diss} .

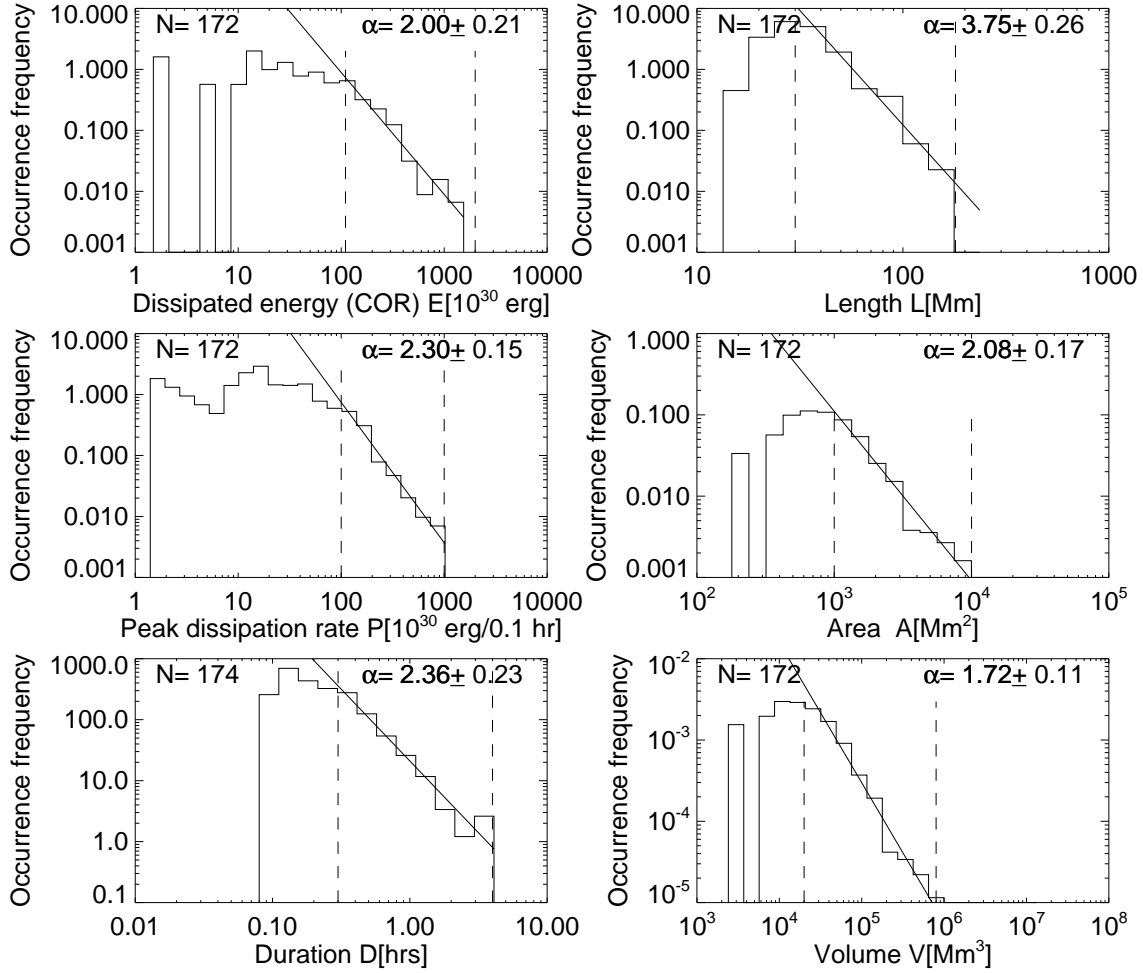


Fig. 15.— Occurrence frequency distributions on a log-log scale for the dissipated energy E_{diss} (top left panel), the peak dissipation rate F_{diss} (second left panel), flare durations T (bottom left panel), the flare length scale L , the flare area A , and the flaring volume V for 172 analyzed M- and X-class flares.

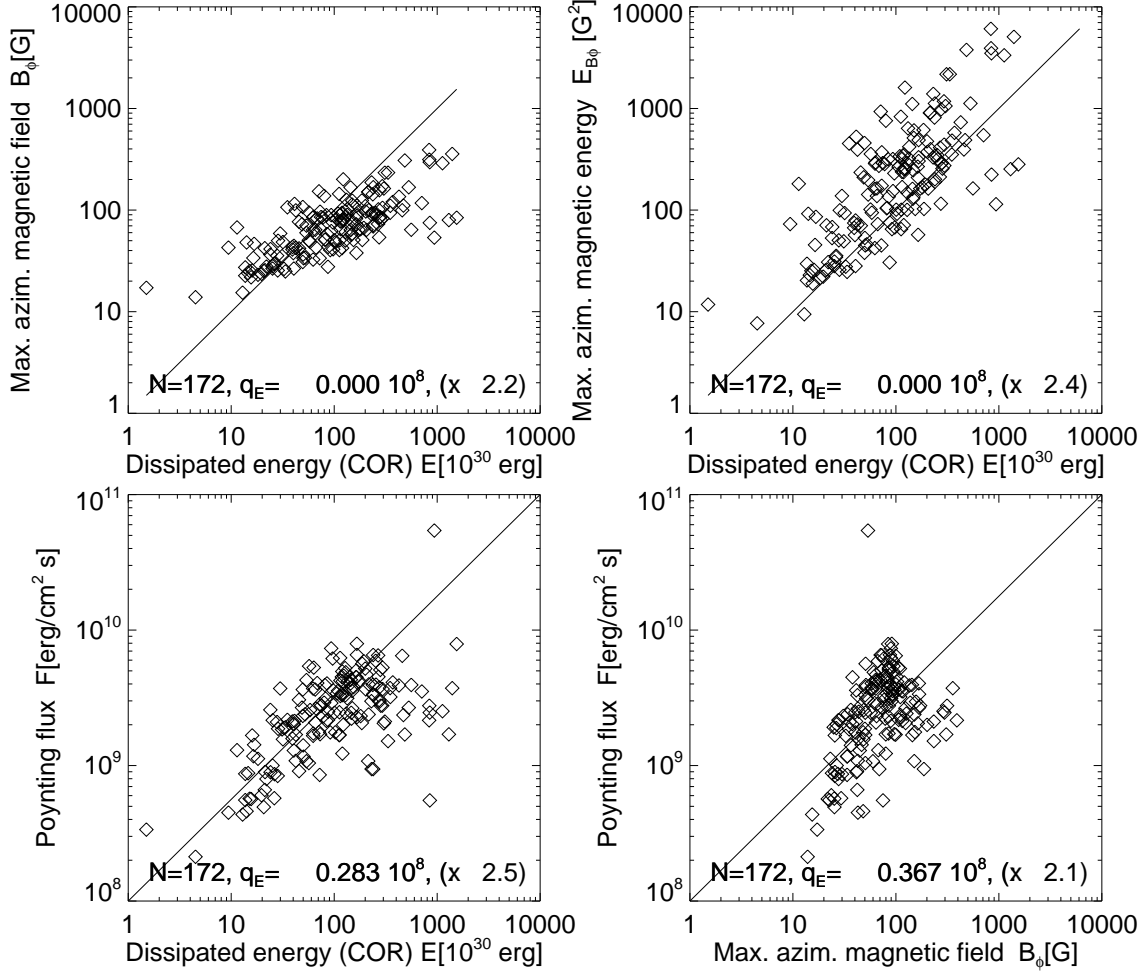


Fig. 16.— Scatterplots between the dissipated flare energies E , the maximum azimuthal magnetic field component B_ϕ (top left panel), the maximum azimuthal magnetic energy per pixel E_{B_ϕ} (top right panel), and the Poynting flux F (bottom left and right panels). Note the proportionality between E and E_{B_ϕ} (top right panel).

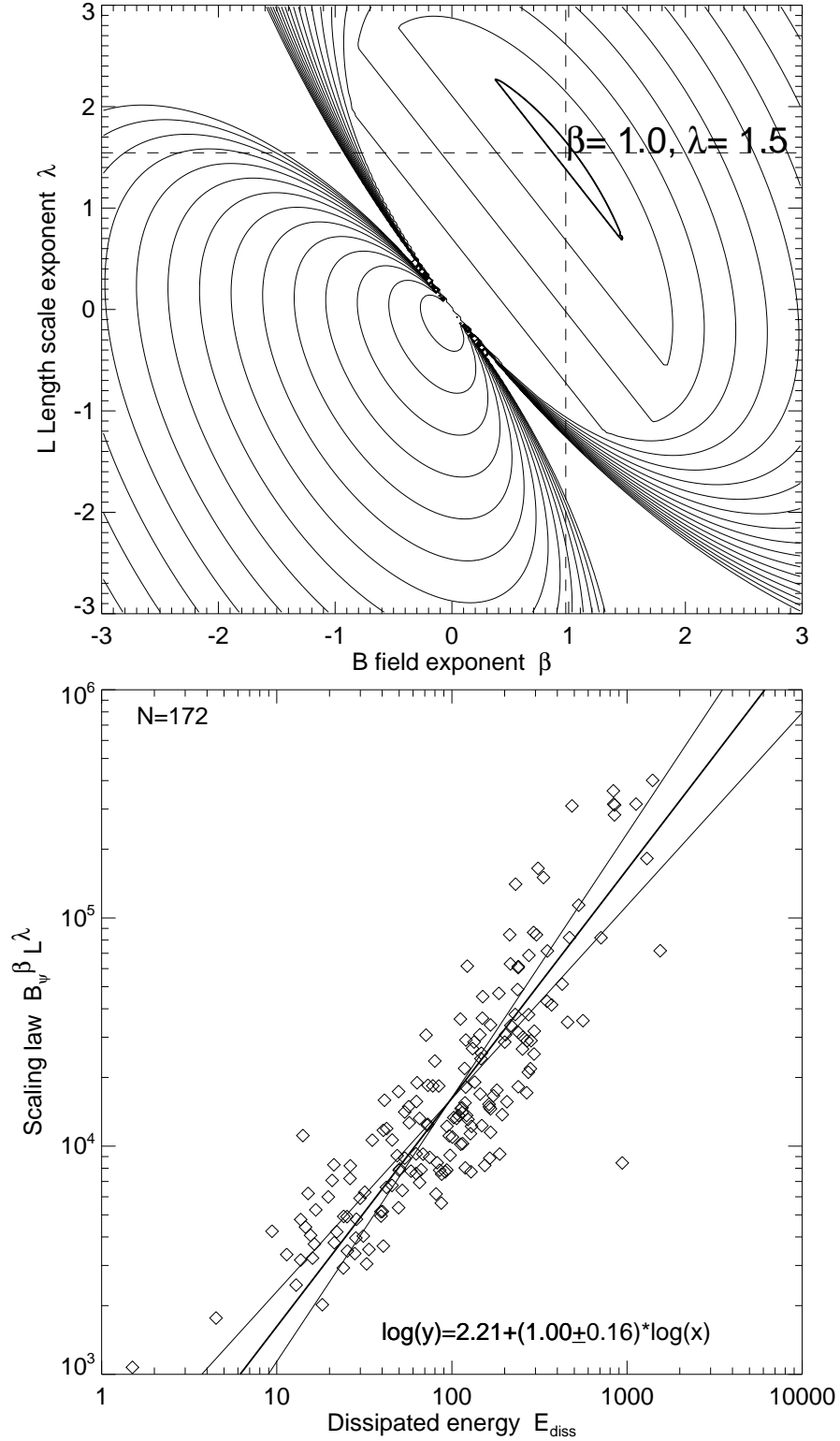


Fig. 17.— Goodness-of-fit map in parameter space $\chi(\beta, \lambda)$ (top panel) for a scaling law of the free energy $E_{free} \propto B^\beta L^\lambda$. A linear regression fit with the best-fit parameters $\beta = 1.0$ and $\lambda = 1.5$ is shown in the bottom panel.

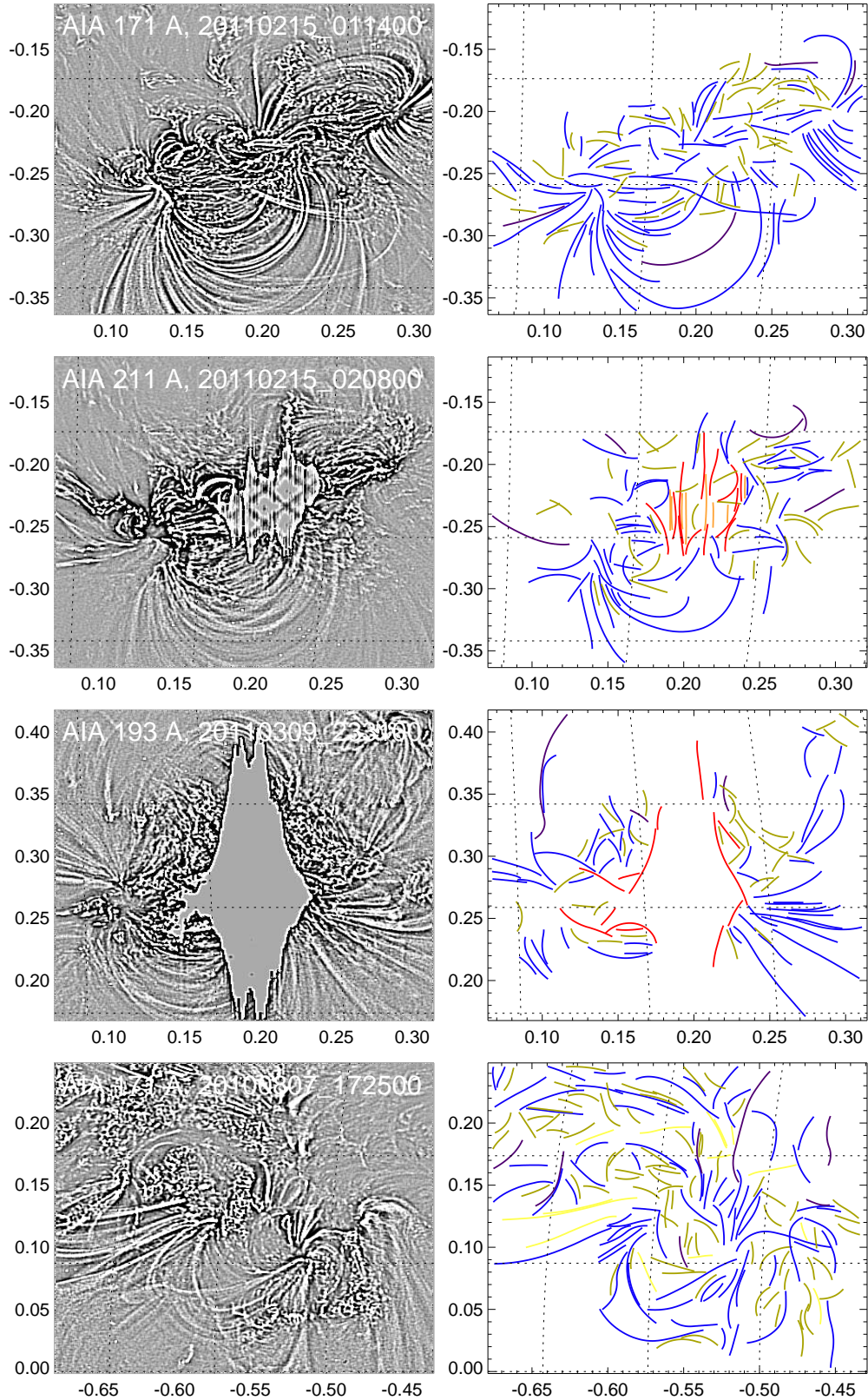


Fig. 18.— Examples of automated pattern recognition of the COR-NLFFF code: coronal loop structures (blue curves), boundaries of saturated image areas (red), vertical streaks from CCD pixel-bleeding (orange), and rippled (moss) structures (green). The greyscale images (left) are highpass-filtered EUV images.

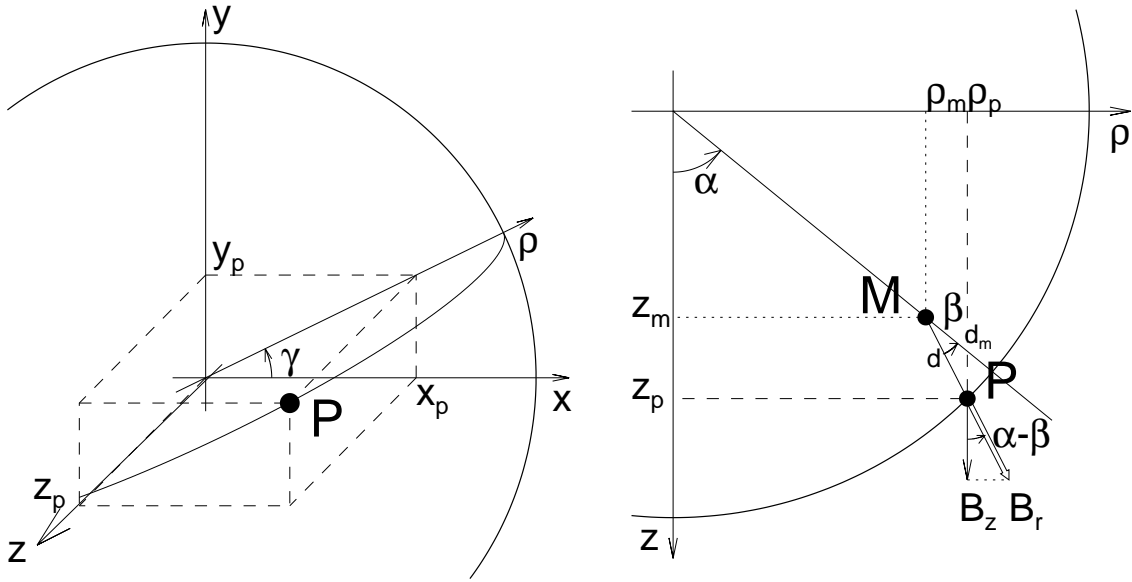


Fig. 19.— For the decomposition of magnetograms into buried magnetic charges, the 3D geometry of a point source $P = (x_p, y_p, z_p)$ in a cartesian coordinate system is shown (left), with the z -axis aligned to the line-of-sight from Earth to Sun center. The plane through the line-of-sight axis and the point source P has a position angle γ in the plane-of-sky with respect to the x -axis and defines the direction of the axis ρ . The geometry of a line-of-sight magnetic field component B_z is shown in the (z, ρ) -plane on the right hand side. A magnetic point charge M is buried at position (z_m, ρ_m) and has an aspect angle α to the line-of-sight. The radial component B_r is observed on the solar surface at location P and has an inclination angle of β to the local vertical above the magnetic point charge M . The line-of-sight component B_z of the magnetic field has an angle $(\alpha - \beta)$ to the radial magnetic field component B_r . (See details in Appendix A of Aschwanden 2012a).

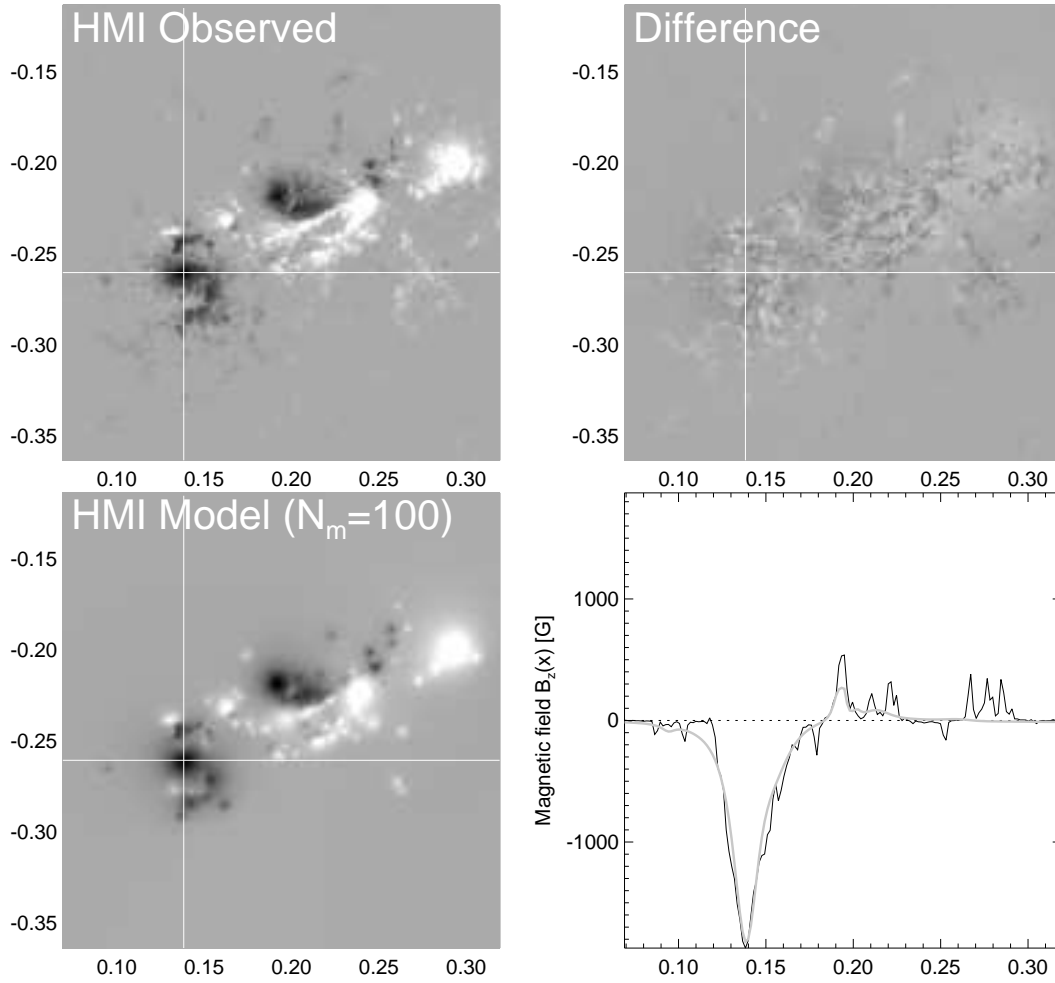


Fig. 20.— Example of a line-of-sight magnetogram from 2011 February 15, 01:56 UT, observed with HMI/SDO (top left), decomposed into $n_m = 100$ unipolar magnetic charges (bottom left), with the difference shown on the same grey scale (top right), along with a scan across the sunspot with maximum field strength (bottom right: black profile is observed, grey profile is the model).

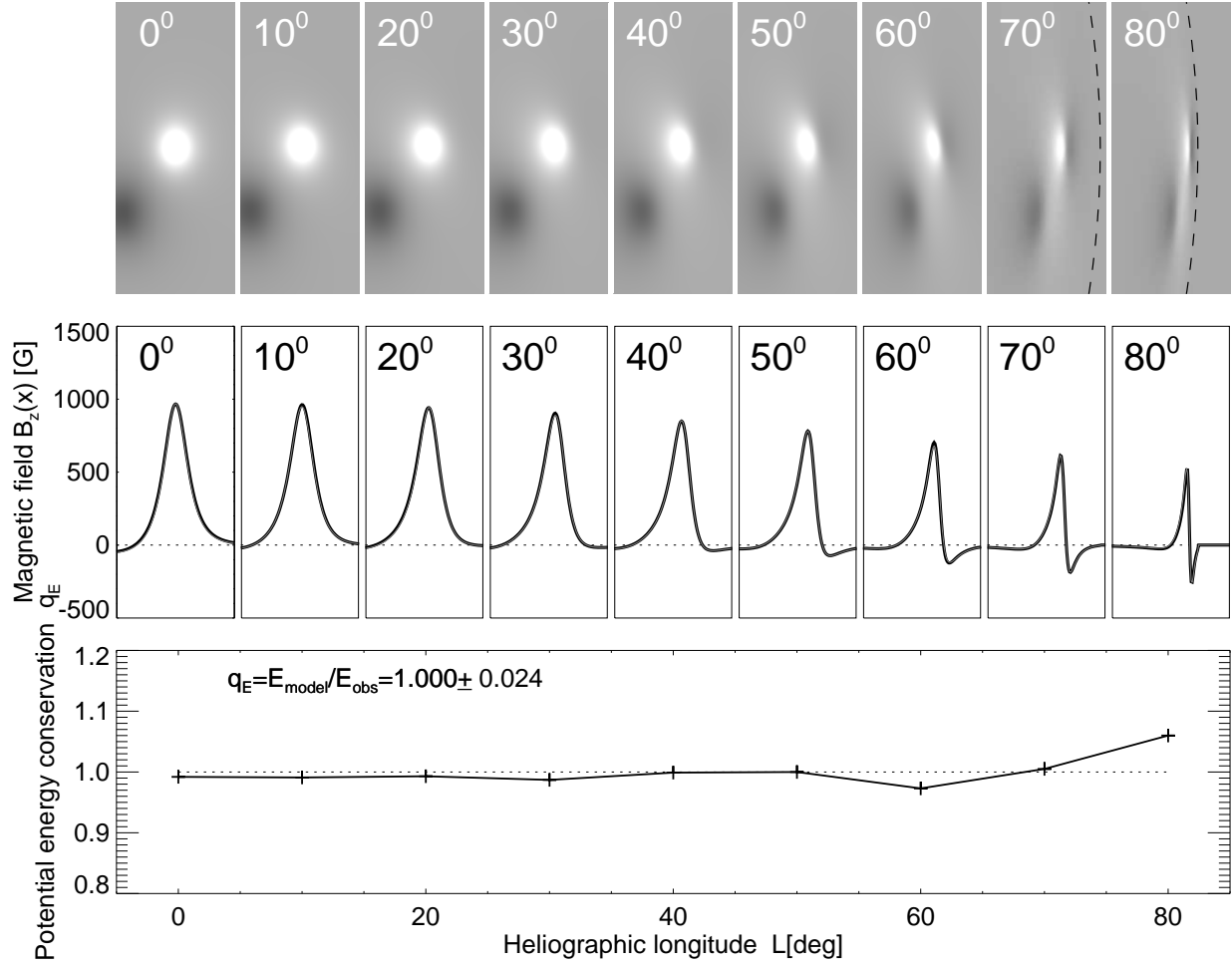


Fig. 21.— Simulation of a magnetogram with a buried dipole as a function of the longitude from Sun center in steps of 10° to the west limb at 80° (top panels). The magnetic field profile of the LOS component $B_z(x)$ is shown from the numerically inverted profile $B_z(x)$, which is indistinguishable from the simulated profile (black curves in middle panels). The conservation of the retrieved magnetic energy $E_B = \int B^2(x, y) dx dy$ is shown in the bottom panel, which demonstrates the invariance of the obtained magnetic energy with respect to the solar rotation or the heliographic position.

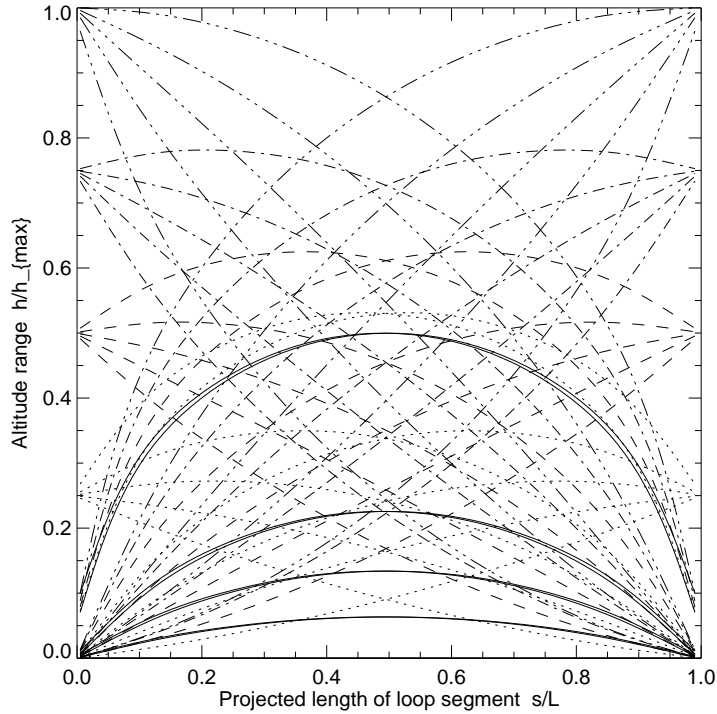


Fig. 22.— Modeling of the altitude coordinate $h(s)$ of loop segments observed in 2D, using a finite subset of $(2 \times n_h \times n_c)$ circular geometries for the 3D reconstruction. The model loops have one footpoint at photospheric height and the other end of the loop segment at altitude $h = h_{max}(i/n_h), i = 1, \dots, n_h, n_h = 5$, and each case is fitted with $n_c = 5$ different curvature radii. The projected distance s is scaled with the loop segment length L .